Manipulation of Colloids by Osmotic Forces

Jérémie Palacci

Manipulation of Colloids by Osmotic Forces

Jérémie Palacci

Présentée pour l'obtention du titre de
Docteur de l'Université Claude Bernard Lyon 1

Soutenue publiquement
Le 15 Octobre 2010

Laboratoire de Physique de la Matière Condensée et des Nanostructures
Université Claude Bernard Lyon I

Jury:
Annie Colin, LOF, Bordeaux (Rapporteur)
Jean François Joanny, Institut Curie, Paris (Rapporteur)
Olivier Dauchot, CEA, Saclay (Examinateur)
Armand Ajdari, Saint Gobain, Aubervilliers (Président du Jury)
Cecile Cottin-Bizonne, LPMCN, Lyon (Directrice de thèse)
Lyderic Bocquet, LPMCN, Lyon (Directeur de thèse)

Contents

Remerciements

Je tiens en premier lieu à remercier l'ensemble des membres de mon jury de thèse qui m'ont fait l'honneur d'accepter de juger ce travail. Conformément aux règles d'usage –puis de galanterie pour départager– je commencerai par remercier Annie Colin puis Jean-Francois Joanny pour avoir rapporté cette thèse. Je tiens également à remercier sincèrement mes deux examinateurs –pour lesquels l'ordre alphabétique prévaudra– Armand Ajdari et Olivier Dauchot. Enfin un immense merci, et j'y reviendrai par la suite, à mes encadrants officiels : Cécile, Lydéric ou officieux "Cyb" qui m'ont entouré de leur attention et de leur amitié au quotidien et ont partagé leur amour et leur connaissance de la Physique.

J'ai eu un mal incroyable à écrire ces remerciements. Non pas qu'il m'était difficile de trouver des arguments allant dans ce sens mais exactement le contraire. J'ai tant de choses à dire à tous ceux que j'ai cotoyés lors de ces trois années qu'il me semble impudique de les coucher sur le papier. Alors pêle-mêle quelques anecdotes et remerciements qui ne sont que de menus indices de tout ce que je dois aux gens sous-cités.

Merci Cécile pour ta gentillesse et ta patience au quotidien. Et il en fallait pour faire faire à un "cross-over" de Benoit Brisefer et Pierre Richard de la microfluidique et autres manipulations de précision ! Tu as été une chef géniale ! :)

Merci Christophe pour ton aide, et ta "froideur de tête" quand je m'emballais et racontais des conneries, ce qui arrivait souvent ! Et bien sûr pour toutes les discussions annexes :)

Merci Lydéric pour avoir accepté de me prendre en thèse puis m'avoir promis que tu stresserais à ma place ! C'était très agréable :) Et aussi pour m'avoir enseigné que les "cons osent tout", et pour tout le reste!

Merci Catherine pour ta bonne humeur et tes ragots, qui à défaut d'être fiables étaient toujours enthousiasmants ! "you rock" !
Merci Anne-Laure (permanente C.R.2 à la date d'écriture des remerciements) d'avoir donné un peu de son temps, de sa gentillesse et de sa bonne humeur à un NON-permanent ! :)
Merci Agnès pour les kms parcourus et les couleurs et la bonne humeur au quotidien, tellement agréables !
Merci bien sûr Elisabeth pour les 1000 discussions toujours engagées et parfois âpres que l'on a pu avoir ensemble sur des sujets aussi variés que la burqa, césarienne vs accouchement par voie basse, le féminisme face au racisme, l'ostheopathie et les blocages lombaires (si tu veux je te passe le numéro de Flore, elle est vraiment bien ;)) et tant d'autres sujets ! Merci également pour ta disponibilité –pour moi en tout cas hihi– et ta gentillesse ...
Merci Jean pour des blinds tests endiablés et autres...
Merci à tous les autres permanents du labo (Luc, Jean-Louis ...) avec qui j'ai eu tant plaisir à échanger !
NB : pour Anne-Laure, j'ai terminé la section permanent, je passe donc aux non-permanents, tu apprécieras la séparation de genre ! :p
Merci aux étoiles filantes et à ceux qui nous ont quittés, Hervé –dont les pieds de plomb n'ont d'égale que des doigts de fée–, Pierre Yop, Benjamin Abecassis -dit le méga steack ! ...
Merci aux autres thésards/postdocs et amis avec qui les pétages de plomb ont toujours été agréables : Laurent –petit Steack deviendra grand–, Lulu –qui devra malgré tout prendre garde à maîtriser ses pulsions meurtrières– Alessandro, mac forever !, et tous les autres !
Merci Laure-Petit (en un mot) pour 2 annés de thèse trop cool passées à s'insulter et à se gaver de gâteaux (tout en s'affutant). Puis pour les années qui suivirent ! Milles excuses pour la procrastination dont

j'ai été coupable pendant ces années ... Je dédie un peu de cette thèse à petit torchon qui sinon ne servirait vraiment à rien!
Éternels Remerciements aux merveilleux amis que sont –par ordre alphabétique :p– Binjjjjjj, Claire, Laetitia, Mantxos et Samuel ! Un rapide coup d'oeil nous permet de voir que Cédric n'est pas dernier ;) Merci pour les tennis, les soirées copines, les soirées rue Dedieu, les nuits sur les coussins pourraves de canapé –parce que quand même on va pas dormir à 2 dans un lit queen-size !–, les samedis 304/Tonk's/crèpes, les repas Domus (au fait c'est combien pour les profs en classe prépa qui ont une carte étudiant ??)... Merci de m'avoir ouvert les yeux sur des réalités qui parfois m'échappaient...;) Je tiens à associer pour cette dernière partie Mr. Tiss ! Et merci à ce dernier d'avoir été un rayon de soleil que dis-je un arc-en-ciel au quotidien pendant toutes ces années :D. Je tiens également à remercier le petit bestiaud. D'abord parce qu'elle a des petites mains et que c'est du coup pas toujours facile de manger un burger. Ensuite parce que sans elle j'aurais passé mes soirées aux restos et aux cinés avec ses parents en me couchant tard et n'aurais du coup sans doute pas pu mener ma thèse à son terme :D Plein de bisous petit bestiaud ! Et bienvenue aux nouveaux –paris en cours!!
Gros merci au vieux keggy et l'aimante Catherine ! Et encore désolé pour la photo ;D
Un immense merci à Mathilde "Pic Pic". Merci pour les milliards de discussions et pour avoir éclairé ces années, les précédentes –et celles à venir– de tes petits sourires ! N'oublie jamais que tu peux déplacer des montagnes si tu en as l'envie (et la volonté hihi) ! You are strong and independent ;) !!
Merci aux potes d'infoENS (Joubs qui n'a plus de genoux, GG-payday, Dan le coolos, Thieu avec qui j'adore m'engueuler , petit

Pané ...)
Merci Thibaut Divoux ! Pour la seule nuit blanche de ma vie –sauf omission involontaire ! Merci d'avoir sacrifié un we de ta vie à corriger les milliards de coquilles et dramatiques typos qui émaillaient (pullulaient??) dans le manuscrit ! Et pour les nombreuses soirées passées à refaire la recherche et le Monde ! Merci pour les persécutions d'étudiants d'agreg. Comme pour tout, bourreau c'est plus amusant à 2 !
Merci mes petits parents de m'avoir toujours accompagnés dans mes choix et pour avoir toujours été là pour moi quand j'en avais besoin ! Même si chez moi la répartition des tâches se fera peut-être un peu différemment (et toc mon papa, tu vas encore passer un certain temps à étendre le linge pendant les vacances :p), vous êtes pour moi un modèle ! Notamment pour avoir eu l'ouverture de nous aider à faire ce dont on avait envie même si cela pouvait sembler farfelu ! Vous assurez grave ! Bisous ! Et puis gros bisous à mes soeurs dont le mauvais caractère n'a d'égal que le bon coeur :D Et puis je suis trop fier d'avoir des soeurs aussi supers :D
Voilà, je vais devoir refermer ces remerciements : compte tenu du coût de l'impression, JLB va me tuer s'il y a trop de pages de remerciements ! :D
Donc rapidos, merci Fanny, Guizz, Kzoo, Gaby, Petit Lo, Elise Hamard–Perron, Nono, Lionel, Amandine, Marion, Prosper, Chris Bellier, Eric... Thanks Andy for the last proofreading! Je suis sûr d'oublier des gens et cela m'attriste !

Je tiens donc à dédicacer ce manuscrit à tous ceux que j'ai eus le bonheur de croiser pendant ces 7 années lyonnaises. Merci pour tout et à bientôt, ici ou ailleurs ! :)

Foreword

This thesis work deals with the manipulation of colloids by *diffusio-phoresis*: the motion induced by a solute gradient. This physical mechanism belongs to the more general class of surface-driven "phoretic" phenomena as the much more famous electro or thermo-phoresis. Thanks to its interfacial origin the phenomenon is robust to downsizing and appears as a relevant tool for flow generation or colloid manipulation in a context of booming micro and nano-fluidics. As diffusio-phoresis transformes the chemical free energy associated with the concentration gradient into mechanical power, I interrogate its role of energy transducer in many situations in soft matter systems where concentrations gradients are naturally present *e.g.* evaporation, biological systems... The recent development of microfluidics gives a proper avenue to study diffusio-phoresis with controlled solute gradients and make it possible to go steps further the pioneering work of Deruyaguin and Prieve.
Dealing with diffusiophoresis, one can consider two different experimental *scenarii*: *(i) Microfluidics:* an external operator imposes a solute gradient and studies the diffusio-phoretic behavior of particles in the gradient or *more subtle (ii) Swimmers:* colloids generate spontaneously the solute gradient and thus self-propel. These two *scenarii* are the two main axes of my PhD work and represent each a chapter of this manuscript.

I first give a presentation of the physical mechanisms at work in interfacial transport in the first chapter and begin with the well-known electro-osmosis to underline the role of the diffuse layer in the vicinity of the solid wall. Then I turn to diffusio-

phoresis and give few comments on the phenomenon. The first chapter aims at presenting a simple and pedagogical review of the literature to help the reader build an intuition of the phenomenon. The presentation is also enriched with two original contributions: *(i)* I demonstrate that diffusio-phoresis can be *generically* written as a *diffusio-phoretic* mobility times the gradient of the osmotic pressure which hence constitutes the natural thermodynamic field of the diffusio-phoretic thermodynamic force and *(ii)* I compare thermo-phoresis and diffusio-phoresis phenomena and underline the deep origin of their different field of applications.

The second chapter is devoted to a *microfluidic study* of diffusio-phoresis. It has required the development of a specific hydrogel microfluidic device in order to control *spatially* and *temporally* the concentration gradient. I first briefly present the principle of the hydrogel microfluidic and demonstrate the control of the solute gradient. Then, I study the directed migration of colloids in a controlled gradient and show a quantitative agreement between the experimental observations and the theoretical expectations. Imposing time-dependent concentration profiles, I observe intriguing phenomena of particles localization which originate in the logarithmic form of the diffusio-phoretic velocity with electrolytes concentrations: $V_{DP} \propto \nabla \log(c)$. The non-linearity of the expression leads to *(i)* the trapping of particles by rectification of oscillations while the high sensibility of the log-sensing to vanishing concentrations is harnessed to obtain *(ii)* particles segregation by osmotic shock. This chapter ends with a few physical perspectives on diffusio-phoresis and an iconoclast questioning on the role of diffusio-phoresis in

biological systems.

The third chapter is dedicated to microswimmers Janus particles. I first describe the basics of the "life at low reynolds" taking place in micro-systems and underline the differences with the large Reynolds number world we usually inhabit. It accounts specific constraints, *e.g.* the time-reversibility of the motion equation. I briefly review various strategies to swim at low Reynolds developed by biological or artificial microswimmers. Then I will discuss the synthesis of Janus colloids as experimental colloidal micro-swimmers. Thanks to the catalytic dismutation of hydrogen peroxide on platinum, they generate autonomously a solute gradient and propel by *self-diffusio-phoresis*. These swimmers are coupled by both hydrodynamic and chemical interactions which make them a natural system to study collective behaviors and related out of equilibrium effects. As a first step, l study the dynamics of individuals and connect it to the statistical properties of an assembly of swimmers under gravity in a tribute to Jean Perrin's historical experiment. This yields to a direct measurement of the effective temperature of the active system as a function of the particle activity, on the basis of the fluctuation-dissipation relationship and tests the validity of thermodynamic concepts in active systems in the case of a semi-dilute solution of Janus particles. This measurement is the first direct measurement of an active temperature in an active system. In this context, it does not demonstrate important breakdown of equilibrium physics –certainly related to the dilute concentration of swimmers– but is a key first step to address more complex behaviors of active matter.

In the fourth and last chapter I present a brief review of

the abundant literature on collective effects, *designed for experimentalists*. The aim is to point relevant and *experimentally accessible* observables and signatures related to the "out-of-equilibriumness" of active systems. I will report theoretical predictions as well as experimental demonstrations of these effects. The purpose of this chapter is to build a basic toolbox for the experimental study of active suspension and notably of Janus microswimmers suspensions. In this context, further perspectives and preliminary experimental results on dense suspensions of Janus microswimmers are discussed.

Each chapter of this thesis manuscript was written as much as possible as standalone and can be read independently.

Je vous remercie d'être venus, il y a de la lumière, c'est chauffé ...[1]

N. Sarkozy, 22 Janvier 2009.

1

Interfacial transport

Historically, surfaces are considered to play a negligible role in fluids dynamics and are often reduced to boundary conditions. For solid-liquid interfaces, it is usually assumed a non-slip condition along the wall and derived flows in agreement with most usual hydrodynamic situations (Poiseuille flow ...). This assumption ignores the microscopic and complex structure of the thin layer at the transition between the solid and the liquid phase considering its effect negligible at larger scales. However many transport phenomena take their origin within the first nanometers at the solid surface. In this chapter we recall how an interfacial gradient of a field O (O being an electrical potential V, a temperature T, or a solute concentration c) leads to a *thermodynamic force* that drives the fluid under motion with respect to (w.r.t.) a wall (by *osmosis*) or reciprocally move par-

[1] First and so far only, report of macroscopic migration in an intensity and thermal gradient, literally *photo* and *thermo* - *taxis*.

ticles (by *phoresis*).
We will present the physics at work in the example of *electro-osmosis* to underline the crucial role of the nanometric diffuse layer to generate flows at much larger scale. Moreover as we will see the consequences of hydrodynamic flows induced by slip velocity are quite different from flows induced by net body forces. Notably, the "slip velocity" is size-independent which confer to the mechanism a strong robustness to miniaturization and downsizing. Given the increased surface to volume ratio at micro-scales and the huge corresponding increase in hydrodynamic resistance, interfacial transport appears as a proper avenue to generate motion and flows in the advent of micro and nanofluidics.

1.1 Electro-osmosis

We first present the physical mechanism for "electro-osmosis", *i.e.* the flow induced by a gradient of electric potential *i.e.* an electric field. This is a "back of the envelop" presentation to catch the physics at work and avoid cumbersome formalism. Furthermore, this example underlines the role of the nanometer diffuse layer in a field gradient to generate a flow. Before osmosis, we make a brief reminder on a few basics of interfacial physics that will be needed in the following.

1.1.1 Debye-Huckel double layer

Let us consider a solid surface in an aqueous solution containing ions. For the sake of simplicity, we consider only ions and cations with the same but opposite charge q. Once immersed in water, the solid surface gets charged. We consider a negative charge for the demonstration, as spontaneously acquired by glass and silicon substrates. Cations in solution are attracted by the charged surface whereas anions are repelled leading to the formation of a double layer in the vicinity of the wall. The steady distribution results from the balance between the electrostatic attraction by the charged surface and the thermal brownian motion of the ions. Finally if forms a a *diffuse layer*: the "Debye-Huckel" layer.
At equilibrium with a thermal bath at temperature T, the distribution of the ions, of charge $\pm$q follows a Boltzmann distribution

$$\rho_{\pm}(z) = \rho_0 e^{\mp qV(z)/k_B T} \tag{1.1}$$

where k_B is the Boltzmann constant and $V(z)$ denotes the electric potential in the solution induced by the solid charged surface (see figure 1.1)[1].
Moreover the electric potential obeys the Poisson equation:

$$\Delta V = \frac{-q\rho_+ + q\rho_-}{\epsilon} \tag{1.2}$$

[1]In order to derive the Boltzmann distribution of the ions, we implicitly assumed a mean field theory following Gouy-Chapman model: we neglected the fluctuations of V and consider only the mean value of the charge distribution. And we also neglect the interactions ions-ions and ions-solvent.

with $\epsilon = \epsilon_0 \epsilon_r$ the permittivity of the considered medium, $\epsilon_r = 80$ for water and ϵ_0 the vacuum permittivity.
Taking into account 1.1, the electric potential is given by the Poisson-Boltzmann equation

$$\frac{\mathrm{d}^2 V}{\mathrm{d}z^2} = \frac{2q\rho_0}{\epsilon} \sinh(qV/k_B T) \qquad (1.3)$$

with the following boundary conditions $V = \zeta$, the "zeta" potential[2] on the solid surface $z = 0$ and $V(\infty) = 0$ (solution of finite energy). In the so-called Debye-Huckel approximation of weak potentials: $qV \ll k_B T$ Eq-1.3 can be linearized and the potential exponentially decays from the solid surface on a Debye length λ_D

$$V(z) = \zeta e^{-z/\lambda_D} \qquad (1.4)$$

with $\lambda_D^{-2} = 2q^2\rho_0/\epsilon k_B T$, the screening length of the charged surface. For a monovalent centimolar salt in water $\lambda_D \sim 3\,\mathrm{nm}$. The diffuse nature of the distribution of the ions close to a charged surface is generally denoted as the "Debye-Huckel double layer".

1.1.2 Electro-osmosis for dummies

In the following we will try to capture the crucial ingredients and the basic physics of interfacial transport. We now apply an electric field in the x direction, *i.e.* an electric potential gradient along the surface (see Fig. 1.1). Of course, as the system

[2]The zeta potential of a surface is typically in the range $\mid \zeta \mid \sim 10 - 100\,\mathrm{mV}$.

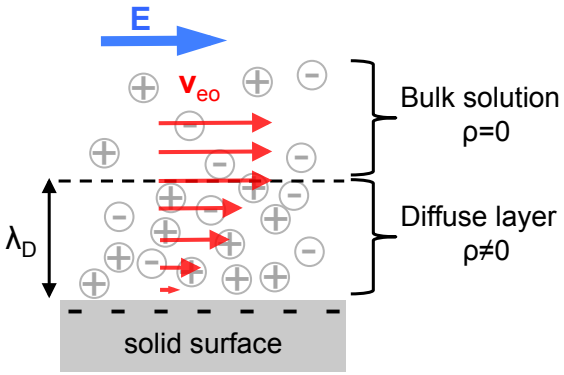

Figure 1.1: **Debye layer and electro-osmotic flow**. Most solid surfaces in water gets charged. It induces the formation of a diffuse Debye-huckel layer which screens the charge of the surface over the length λ_D (λ_D depends on the ions concentration but is typically 3 nm in 10^{-2} M solutions). In the double layer, the net charge is non zero while the bulk solution (beyond λ_D) is neutral. If we now apply a macroscopic electric field in the solution (blue arrow), it therefore exerts no force on the bulk and drives the diffuse layer under motion by a volume force $\mathbf{f}_E = \rho\mathbf{E}$. As λ_D is thin it can be assimilated from a macroscopic view to a stress $\sigma_E \sim \lambda_D \rho \mathbf{E}$. This is the *interfacial driving power* of electro-osmosis which leads to a flow velocity $\mathbf{V}_{eo}$ far from the surface. At mechanical equilibrium, $\mathbf{V}_{eo}$ is given by the balance between the motor and the viscous dissipation by shear (velocity appears as light red arrows) in the Debye layer. Finally, *i.e.* $\sigma_v = \eta \mathbf{V}_{eo}/\lambda_D = \sigma_E$ (with no-slip boundary condition on the surface plane). The static distribution of ions is sketched in grey and the consequences of the electric field appear in red on the figure. An electric potential gradient leads to a flow in the bulk while the total net force is zero. This interfacial transport relies on the existence of a non neutral diffuse layer in the close ($\sim$ nm) vicinity of solid surface by electrostatic interactions. The electro-osmotic flow can be formally reduced to an apparent slip-velocity $\mathbf{V}_{eo}$ for macroscale hydrodynamics.

S =[surface+Debye-Huckel layer+bulk solution] is neutral, the total net force on the system $\mathbf{F}_e = \int_S \rho \mathbf{E} \mathrm{d}V$ is zero. One could therefore be tempted to say that there is "no force, no flow" but this would be incorrect ! The system S is globally neutral but *(i)* the cloud of ions and counterions of the double layer is non neutral and *(ii)* deformable on the sense ions may move. The total charge density follows:

$$\rho = \begin{cases} = 0 & \text{si } y \geq \lambda_d \\ \neq 0 & \text{si } y < \lambda_d \end{cases}$$

The total charge density can be related to the surface potential ζ by the Poisson-Boltzmann equation. We can reduce Eq-1.3 to:

$$\frac{\zeta}{\lambda_D^2} \sim -\frac{\rho}{\epsilon} \tag{1.5}$$

using that the electrical potential gradient takes place in the diffuse layer. Under a macroscopic electric field $\mathbf{E}$, only the ions in the double layer undergo a net volume force $\mathbf{f} = \rho \mathbf{E}$ and move. The velocity within this thin layer determines the velocity field outside the layer $\mathbf{V}_{eo} = V_{eo}\mathbf{e}_x$. As $\lambda_D \sim$ nm, we rewrite the volume force in term of a macroscopic surface stress using Eq-1.5:

$$\sigma_E \sim \rho \lambda_D \mathbf{E} \sim -\frac{\epsilon \zeta}{\lambda_D} \mathbf{E} \tag{1.6}$$

This is the driving power of motion.
This stress is balanced by a viscous stress σ_η taking its origin in the velocity gradient within the diffuse Debye-Huckel layer. Given the non-slip boundary condition on the wall, we get:

$$\sigma_\eta \sim \frac{\eta}{\lambda_D}\mathbf{V}_{eo} \tag{1.7}$$

At mechanical equilibrium, the stress induced by the electric field is dissipated by the the viscous stress $\sigma_E = \sigma_\eta$, and Eq-1.6 and Eq-1.7 leads to the electro-osmotic velocity:

$$\mathbf{V}_{eo} \sim -\frac{\epsilon\zeta}{\eta}\mathbf{E} \tag{1.8}$$

The result here derived with only physical and dimensional arguments can be shown exactly and is known as the *Schmoluchovsky formula* for the electro-osmotic velocity[3].

1.1.3 Electro-osmotic flow in microchannel

We now apply an electric field in a microfluidic channel. If we consider identical materials for each walls, the field drives the ions in the Debye layer and the liquid in the channel is carried at null force with velocity $\mathbf{V}_{eo}$ (see Fig-1.2-a). A plug velocity profile develops in the channel and all the dissipation takes place

[3]We want to underline that in this formula the zeta potential is the electrostatic potential at the "shear plane", *i.e* at $z = 0$ where the velocity vanishes. It is not very clear in our description if it is for example on the solid surface, or after the Stern layer which is "rigidly" attached. In first approximation, one can consider that the Stern layer is small and identify both description to focus on the physics at work (while the condition of velocity continuity leads to define ζ outside the Stern layer in our case). Nevertheless, it can lead to subtleties in the specific defitions of the ζ potential versus the surface potential Ψ_0, which we will not consider in this manuscript but that are of importance in slippage theory [1].

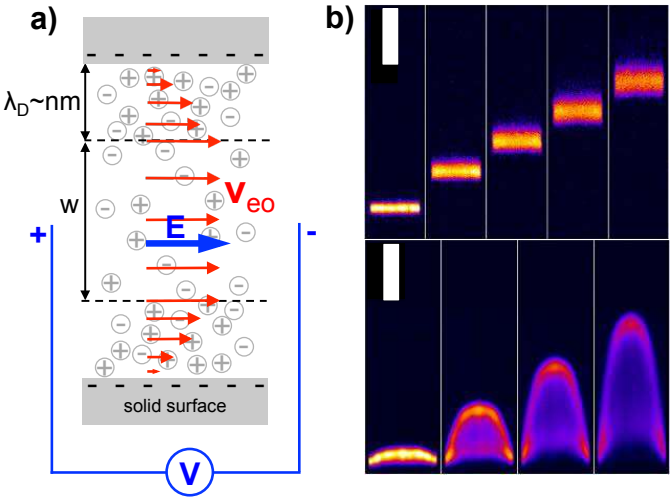

Figure 1.2: *(a)* **Electro-osmotic plug flow in a micro-channel**. We consider an macroscopic electric field imposed in a micro-channel. The electro-osmosis flow originates in the Debye layer (of thickness $\lambda_D \sim$ nm) and leads to a plug flow of constant velocity $\mathbf{V}_{eo}$. The plug profile strongly limits the dispersion of species which can be crucial in analytical applications. Grey stands for the static electrostatic Debye layer, blue is the external electric source and red is for the electro-osmotic flow. *(b)* **Difference of dispersion between electro-osmotic (*Top*) and pressure-driven flows (*Bottom*)**. In the electro-osmotic plug flow, diffusion of the fluorescence is limited to thermal diffusion. The Poiseuille profile is clearly noticeable with pressure-driven flows, and strongly enhances the dispersion of the fluorescent species (notably by Taylor-Aris dispersion). Visualization is performed with caged fluorescence in microchannels (width 200 μm). Scale bar is 200 μm. Reprint from J. Santiago's lab @ Stanford.

in the nanometer-scale interfacial layer. Moreover, according to Eq-1.8 the velocity is robust to downsizing and is insensitive to the huge increase of hydrodynamic resistance experienced in pressure-driven flow [1].The plug profile of the flow strongly limits the Taylor dispersion [2] in the channel which is critical with Poiseuille flow. This makes electro-osmosis a very useful driving method in microfluidics [3]. In particular for chemical analysis purposes which need to displace product without dispersion (see Fig-1.2b.). Conversely electro-osmosis is a common technique for pumping fluids [4, 5]. However pumping with DC voltage is limited by slow velocity (typically $100\,\mu$m/s) and Faradaic reactions at the electrodes. AC applied voltages [6, 7] is therefore used to increase pumping efficiency as well as more fancy electrokinetics effects (ACEO, ICEO ..) thanks to non linear effects [8–10]. The world of electrokinetics is broad and passionating but goes far beyond the basic intuition of interfacial transport we want to offer.

1.1.4 Electro-phoretic motion of a colloidal particle

Let us consider the effect of an electric field on a colloidal particle with radius $R \gg \lambda_D$. Zooming at the scale of the Debye layer, the surface of the colloid appears flat and the considered situation is equivalent to the case of electro-osmosis but with the fluid at rest. We therefore observe a motion of the charged colloid in an electric field, namely the *electro-phoresis*. The derivation of the electro-phoretic velocity $\mathbf{V}_{EP}$ requires the complete resolution of the Stokes flow around the colloid given

the electro-osmotic slip boundary condition, *i.e.* $\mathbf{V} = \mathbf{V}_{EO}$ on the surface. Assuming that the Debye layer is much smaller that the particle radius, it leads *exactly* to the result for an homogeneous particle:

$$\mathbf{V}_{EP} = \frac{\epsilon\zeta}{\eta}\mathbf{E} = -\mathbf{V}_{EO} \tag{1.9}$$

1.1.5 Electro-osmosis: an interfacial transport

We now point some aspects of the results that are in fact shared by all phoretic phenomena and deeply related to the interfacial origin of the mechanism.

- The Debye length is only a few nanometers, and the electro-osmotic velocity $\mathbf{V}_{eo}$ appears as an apparent slip velocity on a macroscopic length scale. Dynamical processes in the region of finite thickness in interaction with a solid surface leads formally to a violation of the non-slip boundary condition (BC) with consequences on the flow at much higher scale.

- The osmotic velocity does not depend on the geometry of the particle, *i.e.* the radius of the colloid. Phoretic transport is hence very robust to downsizing and is thus a golden avenue in the advent of micro and nano-fluidics.

- The flow relies on the modifications of a solute –here ions– in the close vicinity of a solid surface through interactions –here electrostatic through the *zeta* potential of the surface–.

- The total net force exerted on the colloid is zero which is totally different from situations in which the particle motion is induced by a net body force. In that respect the hydrodynamics flow field differs drastically from the flow field associated with external fields as gravity. In particular this implies that the $1/r$ term in the hydrodynamic field vanishes.

1.2 Diffusio-osmosis: motion induced by a solute gradient

The electro-osmosis description demonstrates the huge impact on the flow of a nanometer scale layer. We now quit electrostatics to turn to to an other kind of interfacial transport: *diffusio-osmosis*, flow induced by a solute gradient. It is much less famous than electro-osmosis, and to some regards subtle and less intuitive. We will describe the generation of flow within the interfacial structure by application of a macroscopic concentration gradient and will show how a solute gradient and the subsequent osmotic pressure gradient can 'carry" colloidal particles.

Let us consider a fluid (with constant viscosity η) containing a solute with concentration c. The solute interacts with a solid surface placed in $z = 0$ (see Fig-1.3). The interaction between the solute and the solid surface can be of various origins. If the solute is charged[4], it will interact with the solid surface *via* elec-

[4] And also the surface which is experimentally the case of all solid surfaces immersed in water.

trostatic forces leading to a Debye double-layer at the interface between the solid and the liquid phase. It may also result from Van der Waals interactions between the neutral solutes and the solid surface.
We consider here a potential of interaction $U(z)$ between the solute and the surface and we define a typical length λ for the range of interaction, *e.g.* λ is the Debye length λ_D for electrostatics interactions (see section 1.1.1).
At thermal equilibrium, in the dilute limit of non interacting ions, it leads to a Boltzmann distribution of the solute species:

$$c(z) = c_0 e^{-\frac{U(z)}{k_B T}} \tag{1.10}$$

U can be positive (respectively negative) in the case of repulsive (respectively attractive) interactions between the solute and the surface leading to a depletion (respectively accumulation) of the solute near the surface[5]. We point out that the thermal equilibrium may depend on x along the surface (see Fig. 1.3), if the interaction depends on this coordinate *e.g.* non uniform zeta potential $\zeta(x)$, supposed to vary a length scale a. The result prescribed in equation Eq-1.10 remains locally valid as long as $a \gg \lambda$.

1.2.1 Solute gradient in the bulk: Fick's law

We now consider a situation where a concentration gradient of solute $\nabla c_0(x)$ is imposed far away from the surface. In the bulk,

[5]For electrostatic interactions, a full derivation for the concentration c must also take into account both anions and the cations of the electrolyte as well as electroneutrality.

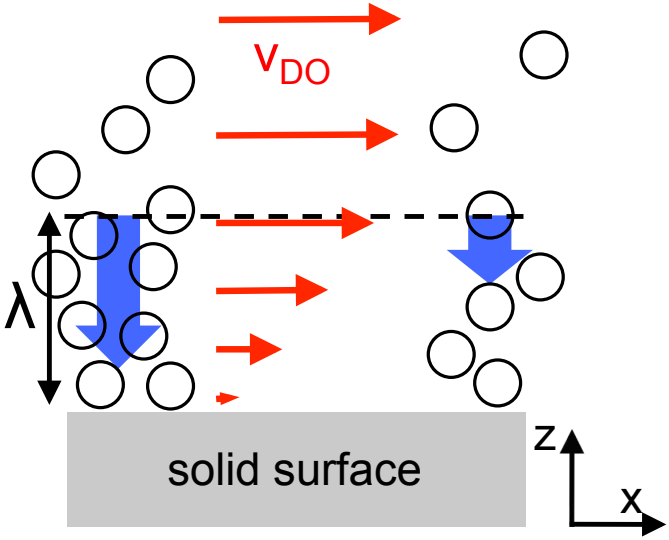

Figure 1.3: **Diffusio-osmosis of a neutral solute.** A solute gradient is additionally imposed along the x direction. The solute interacts with the solid surface (grey) over the range λ. On the picture, we suppose an attractive interaction between the solute and the surface which leads to an accumulation of solute at the interface. The solute gradient along the z results in an osmotic pressure (blue arrow, the size of the arrow magnifies the amplitude of the osmotic pressure) which "squeezes" the liquid to the wall. The large scale solute gradient along the x direction gives an unbalanced osmotic pressure in the diffuse layer. That drives the liquid towards the regions of low concentration of solute (supposing attraction between salt and solute). Consequently there is an apparent slip velocity $\mathbf{V}_{DO}$ outside of the interfacial layer which magnitude is given by the balance between the gradient of osmotic pressure in the layer –the motor– and the viscous stress due to the non-slip condition at the solid surface–the dissipation– (see Eq-1.16 and Eq-1.17)

the concentration gradient induces a flux of solute – due to the random motion of the particles – following the Fick's law:

$$\mathbf{J}_F = -D_s \nabla c_0(x)$$

with D_s the thermal diffusion of the solute. **There is of course no flux of solvent and thus no flow in a fluid in the bulk induced by a solute gradient.**[6]
Let us now reconsider this situation from an alternative perspective. The solute concentration gradient may naively be associated to a bulk osmotic pressure given for an ideal solution [11,12] by:

$$\nabla \Pi = -k_b T \, \nabla c(x) \tag{1.11}$$

It would thus be tantalizing to think *prima facie* that the solvent flows under the osmotic pressure gradient which is in clear contradiction with the previous result. In fact, such an argument is completely wrong! Indeed, at local equilibrium the mechanical –hydrostatic– pressure adapts in order to keep the "total" pressure[7] constant *everywhere in the bulk* according to [13]:

$$p_{solvent} + k_B T c_0(x) = p_0 \tag{1.12}$$

where p_0 denotes the pressure in the bulk far from any surface. In bulk the osmotic pressure gradient is counterbalanced by the

[6] This is exactly true only considering point particles, solvent and solute. Taking into account the size difference between solute and solvent molecules leads to a solvent flux given the fluid incompressibility. This small effect is not considered in the following.

[7] Sum of the solvent and osmotic pressure.

hydrostatic pressure maintaining the system at rest. In particular, this effect can be used in *osmometry*. The osmotic pressure Π exerted by the solute is measured by monitoring the rise of a solution in vertical tube separated with the pure solvent by a semi-permeable membrane [13].
We thus stress that the "bulk" osmotic pressure *does not* drive any flow in the fluid. We can figure out this effect remembering that *in the bulk* the system does not present any membrane against which the force exerted by the solute may act.

1.2.2 Diffusio-osmosis: interfacial transport under solute gradient

We now add a solid surface which interacts with the solute through an interaction potential $U(z)$. Several orders of magnitude separate the macroscopic scale of the solute gradient imposed by an external operator, and the *nanometer* range λ of the interaction. This gives an equilibration time for the concentration and the pressure field in the z direction much smaller than the relaxation for the gradient. Under this assumption, Eq-1.10 rewrites:

$$c(x,z) \approx c_0(x) e^{-\frac{U(z)}{k_B T}} \tag{1.13}$$

The presence of the wall alters the balance between osmotic and hydrostatic pressure. And the mechanical equilibrium of the normal forces along z gives:

$$-\partial_z p(x,z) + -\partial_z U(z)\, c(x,z) = 0 \tag{1.14}$$

Using Eq-1.13, Eq-1.14 can be easily integrated and gives the "osmotic equilibrium":

$$p(x,z) - k_B T c(x,z) = constant = p_0 - k_B T c_0(x) \qquad (1.15)$$

where the constant has been determined in the bulk far from the surface (Eq-1.12). The differentiation of Eq-1.15 with respect to x leads to:

$$\partial_x p(x,z) = k_B T \partial_x [c(x,z) - c_0(x)] \qquad (1.16)$$

A pressure gradient $\nabla_x p$ rewritten in term of unbalanced osmotic pressure $k_B T \nabla_x [c(x,z) - c_0(x)]$ acts on the fluid and forces a flow parallel to the surface. As a driving force within the diffuse layer it is the motor of the *diffusio-osmotic* flow. *At mechanical equilibrium* this force is balanced by the the viscous shear stress according to Stokes equation.

$$\partial_x p(x,z) = \eta \Delta v_x \sim \eta \partial_x^2 v_x \qquad (1.17)$$

where v is the fluid velocity in the layer and the Laplacian operator is replaced by $\Delta \sim \partial_x^2$ as the velocity is along x. Finally, the fluid velocity $v_x(z)$ increases through the interfacial layer to a finite and constant value $\mathbf{V}_{DO}$ in bulk[8]. Given the non-slip condition at the wall (Navier boundary condition), double integrating the Eq- 1.17, one can determine the velocity profile in

[8] Once again, we remind that no net force is exerted by a solute gradient on a fluid in bulk.

the diffuse layer [14, 15]:

$$\mathbf{V}(z) = \int_0^z dz'[e^{-U(z')/k_BT} - 1]\frac{dc_0}{dx}\mathbf{e}_x \qquad (1.18)$$

and thus obtain the "effective slip velocity" outside the layer given by Eq-1.18 for $z = \infty$:

$$V_{DO} = -(k_BT/\eta)\Gamma L\frac{dc_0}{dx}\mathbf{e_x} \qquad (1.19)$$

where $\Gamma = \int_0^\infty dz[e^{-U(z)/k_BT} - 1]$ measures the excess of solute induced by the presence of a solid wall ($\Gamma < 0$ for depletion of solute and $\Gamma > 0$ for solid-solute attraction) and $L = \Gamma^{-1}\int_0^\infty dzz[e^{-U(z)/k_BT} - 1]$ is related to the range of interaction of the potential and is thus of the order of λ.

Case of an electrolyte

We consider the particular case of an electrolyte as the solute and a charged wall characterized by its surface potential ζ interacting electrostatically. For the sake of simplicity we suppose anions and cations of the same but opposite charge $\mid q \mid$. The problem has been studied previously in section-1.1.1 and we only remind that the ions organize in a double layer of typical thickness λ_D screening the surface charge. We can thus conclude that the length scale Γ and L are of order λ_D and Eq-1.19 simply rewrites:

$$\mathbf{V}_{DO} \sim -\frac{\lambda_D^2 k_BT}{\eta}\nabla\mathbf{c_0} \qquad (1.20)$$

Using the expression for the Debye length, $\lambda_D^2 = \epsilon k_B T/2q^2 c_0$ prescribed by the Gouy-Chapman model (see section-1.1.1), one obtains:

$$\mathbf{V}_{DO} \sim -D_{DO} \nabla \log c_0 \qquad (1.21)$$

where $D_{DO} = \epsilon k_B^2 T^2/2q^2\eta$ is the *diffusio-phoretic mobility* of the considered electrolyte (and surface). D_{DO} has the dimension of a diffusion coefficient and $D_{DO} \sim 10^{-10}\,\mathrm{m}^2/\mathrm{s}$ –at room temperature for a monovalent salt– which corresponds to the thermal diffusion coefficient of a $\sim 2\,\mathrm{nm}$ particle in water. Let us stress that D_{DO} only depends on the characteristics of the interfacial layer as for the electro-osmosis/phoresis phenomena.

Marangoni-like effect in the Debye layer
Physically the diffusio-osmotic velocity $\mathbf{V}_{DO}$ can be interpreted following the same reasoning as for electro-osmosis. The driving force of the flow is the excess of osmotic pressure $\nabla(-k_B T c_0)$ integrated over the Debye layer, of thickness λ_D. As $\lambda \sim$ nm, it can be expressed as a macroscopic surface stress:

$$\sigma_o \sim \lambda_D \times \nabla[-k_b T c_0] \qquad (1.22)$$

which is a Marangoni-like stress "$-\nabla\gamma$" with a non uniform surface tension γ, related to the solute concentration as follows:

$$\gamma(x) = \lambda_D k_B T c_0(x) \qquad (1.23)$$

The excess of osmotic pressure is balanced by a viscous stress taking its origin in the velocity gradient in the diffuse layer. Given the non-slip BC at the wall and the diffusio-osmotic velocity outside the diffuse layer, the viscous stress can be written

as:

$$\sigma_\eta \sim \frac{\eta}{\lambda_D}\mathbf{V}_{DO} \tag{1.24}$$

The mechanical equilibrium $\sigma_o = \sigma_\eta$ leads to the "apparent slip velocity" $\mathbf{V}_{DO}$:

$$\mathbf{V}_{DO} \sim -\frac{\lambda_D^2 k_B T}{\eta}\nabla c_0(x) \tag{1.25}$$

as obtained in Eq-1.19. Finally the diffusio-osmotic flow can thus be rephrased as a **Marangoni-like effect in the Debye layer**.

Ion specificity
The theory for diffusio-phoresis in electrolyte gradient relies on electrostatic interaction and does not depend on the type of ion considered(at given charge). Actually we have discussed up to now only the *chemio-osmotic* mechanism of the diffusio-phoretic flow. In order to take into account the salt ion-specificity measured experimentally [16, 17], one has to consider the local electroneutrality of the solution. A full treatment for charged species must involve a supplementary *electrophoretic* contribution originating in the difference of electrophoretic mobilities of the ions. Indeed, an electric field **E'** is spontaneously generated in the *absence* of electrical current when a concentration gradient of an electrolyte is established:

$$\mathbf{j}_e = -(-q)D_-\nabla c_0 - qD_+\nabla c_0 + (-q)c_0\mu_+^E\mathbf{E}' + qc_0\mu_-^E\mathbf{E}' \tag{1.26}$$

with $q > 0$ the electrical charge of the cation[9], D_+ (respectively D_-) the thermal diffusivity of the cations, (respectively anions) and μ_+^E, (espectively μ_-^E) the electrical mobility of the cations (respectively anions). The fluctuation-dissipation theorem relates the electrical mobility and diffusivity [13]:

$$\mu_\pm^E = \frac{\pm q D_\pm}{k_B T}$$

We can derive from Eq-1.26 the electric field **E'** at zero current:

$$\mathbf{E}' = \beta \frac{k_B T}{q} \nabla \log(c_0) \tag{1.27}$$

with $\beta = (D_+ - D_-)/(D_+ + D_-)$ quantifies the difference of ion diffusion coefficients and is ion-specific. The self-induced electric field **E'** drives the diffuse layer by electro-osmosis (see section-1.1) at a slip velocity given by the Schmoluchovski formula (Eq-1.8):

$$\mathbf{V}'_E = -\frac{\epsilon\zeta}{\eta}\mathbf{E}' = -\beta\frac{\epsilon\zeta k_B T}{\eta q}\nabla \log(c_0) \tag{1.28}$$

It contributes simultaneously to chemio-osmosis to the diffusio-osmotic flow. A complete derivation of the problem gives the *total* apparent slip velocity $\mathbf{V}_{DO}$ [18]:

$$\mathbf{V}_{DO} = -D_{DO}\nabla \log(c_0) \tag{1.29}$$

with

$$D_{DO} = -\beta\frac{\epsilon\zeta}{\eta}\frac{k_B T}{q} + \frac{\epsilon}{2\pi\eta}(\frac{k_B T}{q})^2 \log(1-\zeta^2) \tag{1.30}$$

[9] For the sake of simplicity we suppose anions and cations with the same absolute charge.

where the first term originates in the self-induced electrophoretic contribution, and the second term is the complete derivation of chemio-osmotic contribution. Finally, Eq-1.29 and Eq-1.30 give a complete and quantitative expression of the diffusio-osmotic flow induced by an electrolyte gradient. One can use salt gradients– usually obtained with LiCl, NaCl, KCl– to benchmark the validity of the theory of *diffusio* interfacial transport. This is done in [17] and in the experiments reported in the chapter 2 of this manuscript.

1.2.3 Diffusio-osmosis in a nutshell

Focusing on main ingredients and the physics at stake , we finally summarize the diffusio-osmotic mechanism:

1. *Role of the imposed solute gradient.* A solute gradient along x gives a gradient along x of the normal osmotic pressure.

2. *Role of the surface.* The interaction potential U of the solute with the surface provokes a normal osmotic pressure gradient which squeezes[10] the fluid against the wall. This normal stress is mediated in the surface plane by the isotropy of the pressure.

Taking into account this two effects, one can thus figure out that a solute gradient along x gives an interfacial pressure gradient

[10] In the case of an attractive potential

related to the unbalanced osmotic pressure along the same direction (see Fig-1.3). It pushes the fluid in the vicinity of the surface and is at the source of the *diffusio-osmotic* flow.

1.2.4 Diffusio-phoretic motion of a colloidal particle

As for electro-phoresis in section-1.1.4, we now consider the effect of a solute gradient on a colloidal particle in the limit of $R \gg \Gamma, L$ with R the radius of the colloid. The diffusio-osmotic flow in the interfacial layer leads to a net motion of the colloid in the solute gradient, namely *diffusio-phoresis*. Considering the same material and the same surface charge for both the colloid and the surface, the diffusio-phoretic velocity reads:

$$\mathbf{V}_{DP} = -\mathbf{V}_{DO} = D_{DO}\nabla \log[c_0(x)] \tag{1.31}$$

$$= D_{DP}\nabla \log[c_0(x)] \tag{1.32}$$

where $D_{DP} = D_{DO}$ defines for consistency the *diffusio-phoretic mobility*. As for electro-phoresis (see section-1.1.4), the driving force acts *only* in the diffuse layer and gives a "phoretic" velocity which depends on interfacial properties but non of the radius of colloid. This gives the phenomenon a high robustness to downsizing, provided $R \gg L, \Gamma$.
Diffusio-phoresis is a ballistic motion along a solute gradient and thus completely different from a diffusive dynamics. We can however assess on purely dimensionnal basis that the diffusio-phoretic mobility will compare with natural diffusion in the sys-

tem and thus with the diffusion constant D_c of the colloid[11]. The thermal diffusion is given according to the fluctuation-dissipation theorem by the Stokes-Einstein formula: $D_c = k_B T/6\pi\eta R$ [19–22]. If we consider a colloidal particle of radius $R = 0.5\,\mu$m in water at ambient temperature, $D_c \sim 0.4\,\mu\text{m}^2/\text{s}$ and is thus much smaller than $D_{DP} \sim 100 - 500\,\mu\text{m}^2/\text{s}$. We now consider the diffusivity of the solute used as a solute gradient *e.g.* LiCl salt. The thermal diffusion $D_s \sim 1300\,\mu\text{m}^2/\text{s}$[12] is of the same order of magnitude as the diffusio-phoretic mobility of the colloid. This is a hint on the role of *carriers* exerted by the solute molecules to drag the big species –the colloid– along the gradient as recently underlined in [17].

1.2.5 General case *–New!–*

In this section, *which may be skipped on a first reading*, we come back on the diffusio-osmosis phenomenon and emphasize the osmotic nature of the process. While most of the chapter is a review of the literature, we point that the following result is an original contribution.

We generalize the result of Eq- 1.19 to situations where the osmotic pressure discards the ideal solution which goes as $\Pi = k_B T c$ (see Eq-1.11). This is notably the case for polymer so-

[11] This intuition will be supported by numerous experimental and theoretical results in chapter 2.

[12] For an mulitvalent electrolyte solution for which anion and cation do not present the same diffusivity, the salt diffusivity is defined as detailed in [23] as $D_s = \frac{(|z_-|+z_+)D_-D_+}{z_+D_+ + |z_-|D_-}$ where D_+ and D_- the diffusivities of the consituent ions and z_+ and z_- their valence.

lutions which deviate significantly from ideality and present an osmotic pressure $\Pi_p \sim c^{9/4}$ for semi dilute solutions [13].
We consider the same situation and notation as in section-1.2.2 and Fig-1.3. In brief, a solute gradient $\nabla c_0(x)$ is imposed along a flat solid surface. The solute undergo an external potential $U(z)$ from the surface.

In bulk

In the regime of large concentration of the solute, the solution is no longer ideal. In bulk, the only difference with the ideal case is that the Fick's relation should be replaced by[13] the following:

$$\mathbf{J}_s = -\lambda(c)\,\nabla\mu[c]$$

with $\mu[c]$ the chemical potential of the solute and λ a mobility. One finds the usual Fick's law in the small concentration limit with $D = \lambda/c$.

In the diffuse layer

Solute profile
We first focus on the solute distribution. We assume as in section-1.2.2 a thin diffusive layer so that the equilibration along is always z reached, given a solute gradient. The local equilibrium is thus attained and rewrites, neglecting gradients along

[13] In fact, this is the natural way to write the flux as μ is the natural thermodynamic affinity. The usual Fick law is the limit case.

the surface w.r.t. z gradients[14] [13]:

$$\mu[c(x,z)] + U(z) = \mu[c_0(x)] \tag{1.33}$$

Osmotic pressure
A general formulation for Π can be expressed with f, the free energy density [13]:

$$\Pi(c) = c\frac{\partial f}{\partial c} - f(c) + f(c=0) \tag{1.34}$$

Pressure profile
We now turn to the pressure profile. It is derived from the projection of the Stokes equation along z:

$$0 = \eta\Delta v_z - \nabla_z p + c(x,z)(-\partial_z U) \tag{1.35}$$

with $v_z = 0$ as the flow is along x so that:

$$\nabla_z p = c(-\partial_z U) \tag{1.36}$$

Using, Eq-1.33, the right term of Eq-1.36 gives,

$$c(x,z)(-\partial_z U) = -c \times \nabla_z \left(\mu[c_0(x)] - \mu[c(x,z)]\right) = c\nabla_z \left(\frac{\partial f}{\partial c}\right)_T \tag{1.37}$$

[14] Note that this is the stationary solution of the Smoluchowski equation: $\partial_t c + \nabla J_s = 0$, with

$$J_s^z = -\lambda\nabla_z\mu + m\,c\,(-\partial_z U)$$

with m a mobility. Inserting the equilibrium solution $\mathbf{J}_s = 0$, we obtain the fluctuation-dissipation relationship for the mobilities λ, μ: $\lambda = m \times c$.

using the thermodynamics definition for the chemical potential $\mu = \left(\frac{\partial f}{\partial c}\right)_T$.
Now, using the expression 1.34 for the osmotic pressure, one has

$$\nabla_z \Pi[c] = c \times \nabla_z \left(\frac{\partial f}{\partial c}\right)$$

Altogether,

$$c(-\partial_z U) = \nabla_z \Pi[c]. \tag{1.38}$$

Coming back to Eq-1.36, one deduces $\nabla_z(p - \Pi) = 0$, and thus

$$p(x,z) - \Pi[c(x,z)] = p_0 - \Pi[c_0(x)] \tag{1.39}$$

Velocity profile
We now consider the velocity profile projecting the Stokes equation along x:

$$0 = \eta \Delta v_x - \nabla_x p + c(-\partial_x U) \tag{1.40}$$

The last term being zero, using Eq-1.39, it can be recast into the expression:

$$0 = \eta \Delta v_x - \nabla_x \left(\Pi[c_0(x)] - \Pi[c(x,z)]\right) \tag{1.41}$$

The solution of the equation is

$$v_x(x,z) = \frac{-1}{\eta} \int_0^z dz'\, z'\, \nabla_x(\Pi[c_0(x)] - \Pi[c(x,z)]) \tag{1.42}$$

Now using Gibbs-Duhem relation, $d\Pi = cd\mu$[15], one may rewrite this expression as

$$v_x(x,z) = \frac{1}{\eta}\int_0^z dz'\, z'\, \left(c_0(x) - c(x,z)\right) \nabla_x \mu[c_0(x)] \qquad (1.43)$$

For this result we also used, accordingly to Eq-1.33, that

$$\nabla_x \mu[c(x,z)] = \nabla_x \left(\mu[c_0(x)] - U(z)\right) = \nabla_x \mu[c_0(x)]$$

independent of z.
Using the Gibbs-Duhem relation

$$c_0(x)\nabla_x \mu[c_0(x)] = \nabla_x \Pi[c_0(x)]$$

One obtains a more transparent expression for the diffusio-osmotic velocity:

$$\mathbf{V}_{DO} = K_{DO} \times \nabla\Pi[c_0(x)] \qquad (1.44)$$

with the diffusio-osmotic mobility K_{DO} thus defined as

$$K_{DO} = -\frac{1}{\eta}\int_0^\infty dz'\, z' \left(\frac{c_0(x,z)}{c_0(x)} - 1\right) \qquad (1.45)$$

This result demonstrates that diffusio-osmotic transport is osmotic *by nature* and points the osmotic pressure Π as the *proper* thermodynamic variable of interest. It ultimately shows that the "logarithmic-sensing" of the *diffusio* velocity: $V_{DO} \propto \nabla \log c \sim$

[15] Also shown directly: $\nabla\Pi = c\,\partial_c^2 f(c)\nabla c$, while $\nabla\mu = \partial_c^2 f(c)\nabla c$

$\nabla\mu$[16] (see Eq-1.32) is not related to a gradient of a gradient of free energy as could be thought naively.
Additionally the non-linear "sensing", *i.e.* the non linear dependence of the velocity w.r.t. the solute concentration may originate from non-linearities of the osmotic pressure (as for polymers) or from the mobility K_{DO} (case of an electrolyte). Such a non-linearity can be harnessed for interesting out-of-equilibrium properties as patterning (see section 2.3) which gives the mechanism a wide range of applicable solute.

[16] Assuming the case of an ideal solution with chemical potential $\mu = k_B T \log(c)$.

1.3 Further insights on *diffusio* transport

1.3.1 Massive amplification by hydrodynamic slip

We previously reviewed the generation of flow, electro-osmotic or diffusio-osmotic, within the diffuse layer by application of a macroscopic, respectively electric potential or osmotic pressure gradient. As an interfacially-driven phenomenon, we now report the impact of *slippage* on the transport and outline the physical ingredients that lead to its massive amplification.

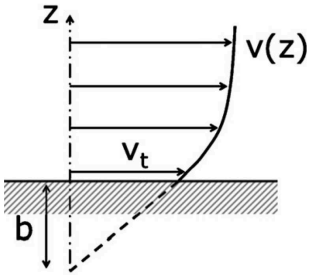

Figure 1.4: **Slip length b.** The slip length is the distance in the solid at which the linear extrapolation of the velocity vanishes. Reprint from [1].

Slippage

The question of hydrodynamic boundary conditions for simple fluids has motivated large amount of recent, theoretical and experimental, work recently. Usually, when a simple liquid flows over a motionless solid wall, its velocity is assumed to be zero near the wall. This assumption postulated by hydrodynamics is called the Navier non-slip boundary condition. Although it is widely verified for macroscopic flows, the nature of the boundary

condition at small scales has been revived by the investigation of flows at nanoscale [1] by means of Surface Force Apparatus [24], nanoPIV [25]... These experiments have shown evidence for the existence of slip BC with velocity $\mathbf{V}_s$ along the wall . Formally, wall slippage is usually described in terms of a *slip length* b defined as the distance inside the solid at which the linearly extrapolated slippage velocity becomes zero (see Fig-1.4) [1]:

$$V_s = b\frac{\partial V}{\partial z} \tag{1.46}$$

On flat hydrophobic surfaces

We now consider a flat surface which hydrophobicity is characterized by its contact angle θ_c. The slip length b on the surface can be determined *via* the simple scaling relationship $b \propto (1 + cos\theta_c)^{-2}$ predicted in [26].
We now explore the consequences of the slippage on the interfacial transport and reproduce the physical reasoning proposed in [15]. A solute gradient $\nabla c_0(x)$, (respectively an electric potential gradient) is imposed to the bulk and and generates a volume driving force f_d integrated over the diffuse layer of thickness λ which can be thus rewritten as a driving stress:

$$\sigma_d = \mathbf{f}_d \times \lambda$$

$\mathbf{f}_d = -\nabla k_B T c_0$ for diffusio-osmosis (respectively $\mathbf{f}_d = -\rho\mathbf{E}$ for electro-osmosis). It is balanced by the viscous stress in the diffuse layer. Given the slip velocity $\mathbf{V}_s$ at the wall and the diffusio-osmotic (respectively electro-osmotic) velocity outside

the diffuse layer, the viscous stress reads:

$$\sigma_\eta \sim \eta \frac{\mathbf{V}_O}{\lambda + b} \tag{1.47}$$

using the definition of the slip length b as the equivalent position, in the solid, where the non-slip BC would apply. The mechanical equilibrium finally gives an effective slip velocity V_O^b, enhanced by the hydrodynamic slip, by a factor $1 + b/\lambda$ where λ measure the interfacial thickness:

$$\mathbf{V^b}_O \sim -(1 + b/\lambda)\frac{\lambda^2}{\eta}\mathbf{f}_d \sim (1 + b/\lambda)\mathbf{V}_O^0 \tag{1.48}$$

where $\mathbf{V}_O^0$ stands for the effective slip velocity without slippage and $\mathbf{V}_O^b$ with a slip length b.
The enhancement of interfacial transport, notably electro or diffusio osmosis, by hydrodynamic slippage can actually be very large. For molecular solutes, the interaction range can be very short: $\lambda \sim 0.3\,\text{nm}$. As the slip length can be up to $b \sim 20{-}30\,\text{nm}$ [24] on smooth hydrophobic surfaces, one can expect *giant amplification* of the flow by a factor of 100, or at least by an order of magnitude !

On superhydrophobic surfaces

Previous results encourage to increase the slip-length to magnify even more the amplification of the transport. In this scope the recent development of artificial superhydrophobic (SH) surfaces, which couple chemical hydrophobicity with multi and large scale roughness with exceptional non wetting properties ($\theta_c \sim 180$)

seem to be a relevant avenue to take up the challenge. Indeed, it was shown that one could define an "effective slip length" b_{eff} on SH surface up to a few microns. With $b_{eff}/\lambda \sim 10^2 - 10^4$ on these surfaces, one could expect massive amplification of interfacial transport, and thus extremely efficient microfluidic pumping based on electro-osmosis or chemical diffusio-osmotic transduction. In fact the problem is slightly more tricky and the massive amplifification depends on the interfacial transport: no amplification is obtained for electro-osmosis on SH surface while amplification of more than 3 orders of magnitude can be achieved for diffusio-osmosis. This result was recently obtained in [27] by molecular dynamics (MD) simulations and we will only give a basic idea of the physical reasons which make diffusio-osmosis and electro-osmosis so different on SH surfaces.

We consider a SH surface with slipping length b_{eff} (see Fig-). As for smooth surface, the effective slip velocity $V^{b_{eff}}$ is given by:

$$\mathbf{V_O^{b_{eff}}} \sim -(1 + b_{eff}/\lambda)\frac{\lambda}{\eta}\langle \mathbf{F}_d \rangle_{eff} \qquad (1.49)$$

where $\langle \mathbf{F}_d \rangle_{eff}$ is the "effective" driving force integrated over the diffuse layer, *i.e.* averaged over the pattern.

Electro-osmosis
As liquid-air interface is not charged, the driving force of the electro-osmotic flow only takes place in the regions where the liquid is in contact with the solid surface. One thus expresses the effective driving force on SH surface $\langle \mathbf{F}_d \rangle_{eff}$ in terms of the

integrated driving force $\mathbf{F}_d^0$ on a smooth, non slipping surface :

$$\langle \mathbf{F}_d \rangle_{eff} \sim \Phi_s \mathbf{F}_d \tag{1.50}$$

with $\Phi_s \sim a/L$ the solid fraction of the SH surface where a and L are characteristics of the SH surface. a is the typical length scale for solid/liquid contact areas and L is the roughness periodicity and height.
Using the expression of the effective slip length $b_{eff} \sim a/\Phi_s$ as in [28] and gathering Eq-1.49 and Eq-1.50, one does not expect a large increase of the velocity [29]. This scaling argument has been confirmed numerically by MD simulations [27]. Super hydrophobicity does not amplify electro-osmotic transport as the driving force is reduced as much as the viscous dissipation on such surfaces.

Diffusio-osmosis
We now turn to the case of diffusio-osmosis which is significantly different. The key point is that due to the interactions of ions with the air-water interface (*e.g* image charge repulsion of specific adsorption), a diffuse layer still exists at the air water-interface (contrary to electro-osmosis) [30]. The driving force $\mathbf{F}_d$ is thus approximately uniformly distributed and the effective driving force on SH surface rewrites:

$$\langle \mathbf{F}_d \rangle_{eff} \sim \mathbf{F}_d \tag{1.51}$$

Finally using Eq-1.49, one gets a giant amplification of the diffusio-osmotic flow by a factor $b_{eff}/\lambda \sim 1000$ on SH surfaces.

These theoretical expectations still remain to be supported and used experimentally to reach a new class of "high velocity" microfluidic flows.

1.3.2 Thermo-phoresis *vs* Diffusio-phoresis

We discussed previously the motion of a colloidal particle under a solute gradient or an electric field. We now present a very brief overview of an other class of interfacial transport, the motion of a particle induced by a temperature gradient, so called *thermophoresis*.

Thermo-phoresis

When a colloid is placed in a temperature gradient $\nabla T_0(x)$, it presents a steady drift velocity along the gradient [31]:

$$\mathbf{V}_T = -D_T \nabla T_0(x) \tag{1.52}$$

where D_T is the thermo-phoretic mobility, positive for *thermophobic* particles and *thermophilic* otherwise. Most colloids preferentially move to colder regions while macromolecular solute as DNA present thermophilic characteristics.
For most investigated systems, the order of magnitude of $\mid D_T \mid$ is rather universal and varies within a limited range $10^{-12} < \mid D_T \mid < 10^{-11}\,\mathrm{m^2/s^{-1}K^{-1}}$. But predictions on the mobility are tedious and strongly depend on the system [31]. Additionally the sign of D_T may depend on the temperature and present a temperature inversion T^* of thermophobic to thermophilic transition. Moreover a size dependance of the mobility recently

reported [32] and unexpected for interfacial transport recently reported is at the core of a controversy feeding experimental debate as well as theoretical developments [32–34].

Thermo-phoresis *vs* Diffusio-phoresis in microfluidics

Gradient establishment
We consider a microfluidic situation with a channel filled with particles. An external operator imposes a gradient of solute (respectively temperature) to move particles by diffusio-phoresis (respectively thermo-phoresis) across the channel. The gradient is imposed through boundary conditions, *i.e.* side of the channel distant of a length ℓ, and the typical time to achieve the steady gradient is dimensionally given by $\tau \sim \ell^2/K$ where K is the diffusivity of the considered observable, *i.e.* $K = D_s$ the solute diffusion coefficient for diffusio-osmosis and $K = \lambda_T$ the thermal diffusivity. The thermal diffusivity of water is $\lambda_T \sim 10^6\,\mu\text{m}^2/\text{s}$ and thus much larger that the diffusivity of a typical solute $D_s \sim 1000\,\mu\text{m}^2/\text{s}$ which gives for the transient time:

$$\tau_T \sim \tau_{DP}/1000 \ll \tau_{DP}$$

For $\ell \sim 100\,\mu\text{m}$ which is a typical scale for microfluidic channels, $\tau_T \sim 10^{-2}\,\text{s}$ while it can take up to $10\,\text{s}$ to develop the solute gradient.

Response time
The time τ can be seen on a slightly different perspective as the "response time" of the system. Let us imagine now that

the external operator varies the boundary conditions with a frequency f. If $\tau \gg 1/f$, the gradient does not develop and thus no phoretic motion of particles is observed. For smaller frequencies $1/f \gg \tau$, the phoretic migration is recovered. The microfluidic system behaves as a *low-pass filter* of cutoff frequency $f^* = \tau^{-1}$ for the interfacial transport of particles.
In this scope, the thermo-phoresis appears as a *high speed* microfluidic tool as it can respond to high frequency $10 - 1000\,\mathrm{Hz}$ stimuli while diffusio-phoresis is strongly limited in its microfluidic applicability by very low response time ($10 - 100\,\mathrm{s}$). Thanks to the use of IR laser which makes possible to heat locally, the developments of the thermo-phoresis in microfluidics [35,36] (or more generally temperature driven motion [37,38]) are now booming.
The counterpart of the high-speed response is a fast relaxation for thermo-phoresis. If for some reasons the BC fluctuate the thermal gradient is modified by these fluctuations and the relaxation of the gradient once the external constraints are released is very fast. In order to take advantage of controlled thermo-phoresis, a system must provide a steady energy supply which is very costly. This might be the reason why thermo-phoresis in nature is up to now only reported in geological systems such as hydrothermal pores [39]. On the contrary, the slow particle diffusion transport smoothens changes in BC and make the gradient quite robust to fluctuating environments. Moreover a track of the gradient lasts for seconds even after suppressing the BC. In that respect, one could imagine that living micro-systems may use diffusio-phoresis as a relevant transport phenomenon of macromolecules inside the cell in the noisy biological environ-

ment. Nevertheless, this point is for now purely speculative as no diffusio-phoretic flow has ever been reported in micro-organisms.

1.4 Take home message

Surface-driven transport thus appears as particularly interesting in the scope of micron-size systems. The flow generation in the diffuse layer at the solid-liquid interface by field gradient (electric potential, temperature, concentration) appears as an "effective slip velocity" at the wall and thus strongly impacts the velocity profile on much higher scale.
In this manuscript, I will mainly focus on *diffusio-phoretic* transport: motion induced by a solute gradient. This phenomenon has been little studied experimentally and thus needs further experimental and theoretical investigations. Furthermore, it proposes in essence a transducer of free energy into mechanical power. This opens new routes in a context of new sources of energy by harnessing natural solute gradient. Moreover, a giant amplification of the effect is expected with SH surfaces which makes of *diffusio* an outstanding avenue for high efficiency microfluidic pumps and chemical-mechanical transducers.
Two natural scenarii can be considered for diffusio-phoresis: *(i)* an external operator imposes a solute gradient and particles move within or *(ii)* particles generates autonomously the gradient and propel. I have developed these two axes during my PhD on two different classes of systems: microfluidics and swimmers.

1. *Microfluidic.* I have designed a specific hydrogel microfluidic technology and device to maintain and accurately control spatially and temporally solute gradients. Such a setup makes it possible to study the diffusio-phoretic migration of particles in a controlled environment.

2. *Swimmers.* I have synthetized self propelled micro-swimmers using a catalytic reaction on one half of a colloid to generate the solute gradient. These active particles constitute the building bricks for the study of collective behaviors of suspensions of self propelled particles thus intrinsically out-of-equilibrium.

Each of the scenario is a chapter of this thesis manuscript.

C'est véritablement utile puisque c'est joli
A. St Exupéry, Le Petit Prince

2

Diffusio-phoresis in a controlled gradient : a gel device

In the previous chapter we have focused on simple physical arguments to build an intuition of interfacial and particularly diffusio-phoretic transport. We now turn to an experimental investigation of the phenomenon. Pioneering works were performed with membranes to establish the solute gradient, thus introducing additional complexity both into the experience and into the data analysis [16] or poor control of the gradient in macroscale experiments [40,41]. Recently the use of microfluidic tool has made possible to study the diffusiophoretic migration of colloids in a well-defined electrolyte gradient [17,42]. Quantitative agreement with theoretical diffusio-phoretic behavior has been recently achieved by Abecassis *et al.* and the experiment has shown (i) a solute driven motion of colloids and (ii) a steady observations under flow. This microfluidic setup also leads to

quantitative predictions of the solute gradient but no temporal or spatial control.

Aim of this work

An important achievement of my PhD has been to develop and use new experimental approaches allowing to go one step beyond in the exploration of diffusio-phoresis phenomena. This requires *(i)* the building-up of controlled concentration gradients and *(ii)* the observations of particles in a *convection-free* environment. We have therefore developed a specific microfluidic device based on an agarose *hydrogel* technology, studied diffusio-phoretic migration and unveiled new osmotically-driven effects.

Organization of the chapter

This chapter first begins with a presentation of the experimental setup. In particular we demonstrate how to generate a convection-free spatial gradient, together with its temporal actuation.
In a second part, we use this experimental device to study the diffusio-phoretic migration of various particles, colloids as well as biological macromolecules, in a benchmark configuration and compare our results with the theoretical expectations. Then the hydrogel microfluidic device is used to unravel new osmotically-driven effects such as patterning and localization. The localization process with time-dependent solute gradients originates in the non-linearity of the diffusio-phoretic velocity and is rationalized by an asymptotic model of *rectification of oscillations* as

well as numerical predictions. Conversely another trapping or localization is also demonstrated in a transient "osmotic shock" provided by the extreme sensibility of the *logarithmic sensing* of diffusio-phoresis to vanishing solute concentrations.
We finally discuss a few perspectives of study of diffusio-phoresis both fundamentaly or applied to microfluidic applications. We will end up by putting forward an iconoclast questioning on the possible role of diffusio-phoresis in living soft matter as concentration gradients are common in living organisms.

Principle

The detailed study of diffusio-phoretic motion relies on our ability to *generate* and *control* concentration gradients. Following the route proposed for the study of bacterial chemotaxis in a microfluidic environment [43, 44], I have developed a microfluidic device made of agarose hydrogel. The principle of the final device is sketched in Fig. 2.1. It relies on the porous nature of the hydrogel [45]: the hydrogel matrix acts as solid walls for the flow but allows the free diffusion of salt and small molecules. In a nutshell, a solute gradient is created across the system by imposing two different concentrations in boundary channels: the source, with concentration $c_1 = c_0$, and the sink $c_2 = 0$. An external operator can therefore control the gradient in a microfluidic chamber *at rest*, *i.e.* without any flow containing the particles (colloids or DNA) under investigation. The setup, sketched in Fig. 2.2-a, allows to impose stationary, as well as temporally switchable, solute gradients in various microflu-

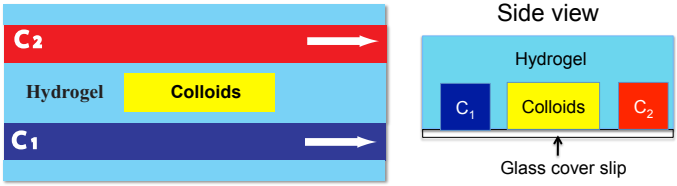

Figure 2.1: **Principle of the hydrogel microfluidic device.** The porous nature of the gel makes possible to impose solute boundary conditions with concentration c_1 and c_2 *via* two side channels and thus control the concentration gradient. Particles under investigation are enclosed in a central chamber.

idic designs[1]. *Although the present manuscript will essentially focus on the experimental study -using this new device- of different physical phenomenon, it should be stressed that the development of the setup itself is actually an important achievement of this PhD work, and mobilized a large amount of work to ensure a proper reliability and reproducibility. Overall, experimental and technical details corresponding to the final configuration are gathered in Appendices A to C for the sake of clarity and a more pleasant reading.*

Globally, a solute gradient, here either of fluorescein, or of a salt[2] or a molecular species as H_2O_2 is created in the central

[1]The microfluidic design is made of two side channels along microfluidic chambers of various sizes (typically 300-600 μm) and shape (rectangular or circular).

[2]We have used LiCl, NaCl and KCl salts.

microfluidic chambers containing the particles *via* two side channels imposing the concentration boundary conditions. The latter can be switched on demand thanks to a manual microfluidic switch that allows modification of the side-channels solute concentrations. After a transient due to the diffusion of boundary conditions across the middle item of the device, a steady profile of the gradient is reached. The concentration gradient is the solution of the diffusion equation:

$$D_s \Delta c = \partial_t c \tag{2.1}$$

with D_s the salt diffusivity and the boundary conditions given by the concentration c_1 and c_2 injected by the syringe pump in the two side channels.
Under stationary conditions, the equation 2.1 reduces to $\Delta c = 0$ which gives at one dimension a linear profile for the concentration with slope $(c_2 - c_1)/\ell$, with ℓ the distance between side channels. For a 2D circular geometry, the solution is given by series of Bessel functions according to the boundary conditions.

2.1 Calibration of the gradient

The gradient profile is calibrated using a fluorescein solution (Roth) of concentration $c_0 = 10^{-4}$ M. In this range of concentration, Diao *et al.* showed a linear relation between the fluorescein concentration and fluorescence intensity [43] making a fluorescent measurement a straightforward visualization of the chemical concentration field in the channel. A syringe

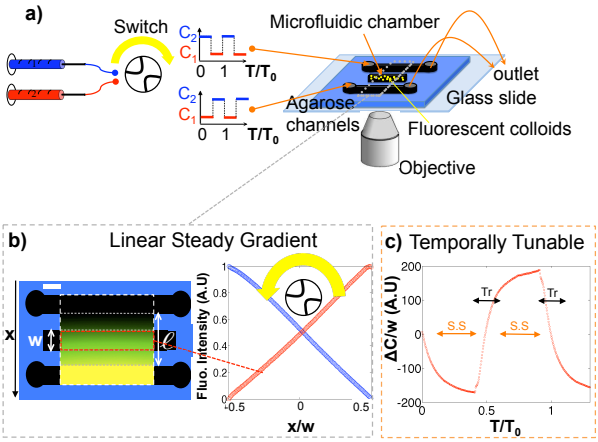

Figure 2.2: *(a)* **Experimental Setup.** hydrogel microfluidic device. A double syringe pump with two solutions of salt of concentration c_1 and c_2 fills the two side channels. A microfluidic switch allows to exchange the salt solutions in the side channels, leading to a time-dependent tuning of the gradient. Particles under investigation (colloids and λ-DNA) are located in the center microfluidic chamber.
(b)-(Left) **Visualization of the fluorescein gradient.** Top view of the microfluidic device setup. The inner box shows the experimental fluorescence intensity image measured for the stationary gradient (gel walls not represented) of a fluorescein solution ($c_1 - c_2 = 10^{-4}$M)). The central chamber width is $w = 300\,\mu$m while $\ell = 800\,\mu$m is the total diffusion width (scale bar is $300\,\mu$m). *(b)-(Right)* **Steady fluorescence intensity profiles.** Steady linear concentration gradient. Temporal changes in boundary conditions upon actuation of the microfluidic switch lead to gradient inversion (red and blue curves). *(c)* **Temporal evolution of the gradient** – for periodic actuation $T_0 = 10$ mins– of the difference Δc of fluorescence intensity on both sides of the central chamber following a gradient inversion. Orange arrows stand for steady gradients whereas the black ones stand for transient states.

pump fills one channel with a fluorescein solution of concentration 10^{-4} M (*the source*) and the other with distilled water (*the sink*). A manual switch allows to invert the role of source and sink and thus reverse the gradient. Measurements are performed for linear channels *i.e.* linear side channels and a rectangular microfluidic chamber. In the following experiments we did not observe interactions between the electrolyte solutions we used and the hydrogel structure of the microfluidic device.

Steady concentration gradient
We consider a linear 1D geometry and define $x = 0$ in the middle of the microfluidic chamber. The length scale ℓ is the length over which the gradient develops, *i.e.* the distance between the side channels as defined previously. The boundary conditions are given by $c(-\ell/2) = c_1$ and $c(\ell/2) = c_2$. As previously stated, a steady profile of the solute concentration is achieved, with slope $(c_2 - c_1)/\ell$. The concentration can be written as:

$$c(x) = \frac{c_0}{2}(1 \pm 2\frac{x}{\ell}) \qquad (2.2)$$

$\pm$ depending whether the source is the side channel on $\pm\ell/2$.
The concentration profile is measured *via the* fluorescence intensity of fluorescein (see Fig. 2.2-b). As expected for this geometry, the steady gradient is linear. The microfluidic switch allows to reverse the role of source and sinks and therefore to mirror the gradient with respect to the center of the channel (red and blue curves). I checked experimentally that the solute flux in the source/sink was sufficient to define constant boundary conditions along the channel. This can be understood in terms of a

definition of a Peclet number. The Peclet $Pe \equiv \tau_D/\tau_C$ compares the diffusive time τ_D for the boundary conditions to diffuse along the length scale ℓ to the convective time τ_C for the fluid to go from the inlet to the outlet. In our experiments, $\tau_D = \ell^2/D_f$, $\tau_C = L/U$ and therefore $Pe = \frac{\ell^2 U}{D_f L}$ where $L \sim 10\,\text{cm}$ is the length of the side channels, $U \sim 3\,\text{cm/s}$ the velocity of the injected solutions, $\ell \sim 800\,\mu\text{m}$ and $D_f = 420\,\mu\text{m}^2/\text{s}$ [46], the fluorescein diffusion coefficient. Under the present conditions, the Peclet number is of order $Pe \sim 450$, much larger than unity. This ensures the stability of the boundary conditions both during the calibration step and the experiment as LiCl diffuses faster than fluorescein salt[3].

Transient concentration gradient.
Following the reversal of the side boundary conditions, the concentration profile is in a transient state. As a diffusive process, the transient duration τ_{tr} thus scales as ℓ^2/D. Experimental visualization of the transient gradient is performed once again with a fluorescein solution monitoring the temporal evolution of the difference Δc of the fluorescence intensity on both sides of the central chamber (see Fig-2.2-c). Both steady and transient states are represented on this figure. After a sharp increase during the transient state, Δc is constant. We nevertheless observe a slow increase of the difference of the concentration. We attribute this "drift" in fluorescence intensity to the 3D diffusion

[3]Indeed the diffusion constant for LiCl is $D'_s = 1360\,\mu\text{m}^2/\text{s}$ which corresponds to a Peclet number of $Pe' \sim 140$.

of the fluorescent salt at the top of the microfluidic chamber[4]. We measure a transient time $\tau_{tr} \sim 2\,\text{mins}$ for fluorescein and $\ell = 800\,\mu\text{m}$. One can then estimate the transient time for LiCl salt given the diffusion constant of fluorescein $D_f = 430\,\mu\text{m}^2/\text{s}$ and LiCl salt $D_s = 1360\,\mu\text{m}^2/\text{s}$ [47]. It gives a typical transient time $\tau_{tr} \sim \frac{430}{1360} \times 2\,\text{min} \sim 35\,\text{s}$.
Finally after after a few tens of seconds for salts, we can assume a linear and steady concentration profile in the microfluidic chamber containing the particles under investigation.

2.2 Diffusio-phoretic migration

We now consider the situation where particles have been enclosed in the central chamber. We first concentrate on the case of latex colloids of diameter $200nm$. The step by step protocol to perform an experient, *i.e. (1).* mold the hydrogel microfuidics and *(2).* fill a microfluidic chamber with the particles under investigation is thoroughly developed in Appendix B and C at the end of the chapter.

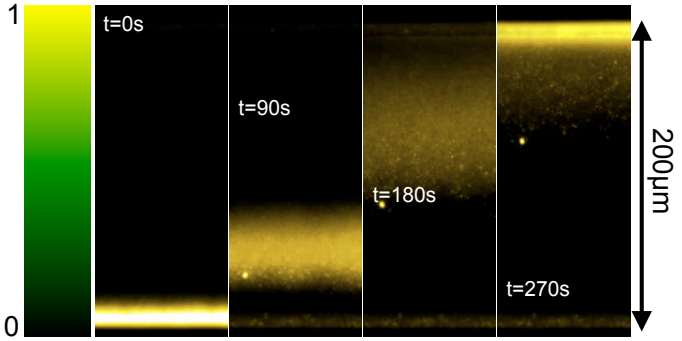

Figure 2.3: **Diffusio-phoretic migration of fluorescent colloids** towards high concentration of LiCl. The salt concentration normalized by c_0 is sketched by the lateral bar.

2.2.1 Diffusio-phoretic migration in a solute gradient: first approach

We start from a configuration where all particles are on one side of the channel. At $t = 0$ the salt gradient is reversed with now the high concentration on the opposite side. Under the imposed solute gradients, the colloids are observed to exhibit a purely transverse motion (see Fig-2.3). The drift is along the salt concentration gradient and towards the higher solute concentration thus revealing a **diffusio-phoretic migration**

[4]Indeed the channels are typically 100 μm high while the PDMS spacer defines agarose stamps of thickness 700 μm. As a consequence, a 600 μm layer of gel is at the top the channels/chambers

of the colloids thanks to a salt gradient (see Fig-2.3). The diffusio-phoretic velocity is of order $1\,\mu$m/s. When particles have gathered at the opposite wall, the gradient is reversed again thus showing a symmetrical behavior with a reversed transverse motion (see Fig. 2.4-a and supplementary movie 1).

2.2.2 Experimental validation

Before a quantitative analysis of the diffusio-phoretic transport of particles in a controlled gradient, we want to underline a few experimental validation of the designed microfluidic device.

Experimental checks

I first checked that without any salt gradient the colloids dynamics is purely Brownian. A slight longitudinal drift can be observed in some experiments by the following of a few bunches of colloids as markers. The upper bound for this occasional drift speed is 50 nm/s which is small compared to the diffusio-phoretic velocity of the particles and thus **negligible**. We infer this a Darcy flow through the porous gel[5]. This observation may ap-

[5]The pressure gradient originates in the pressure drop due to the Poiseuille flow in the side channels. The pressure gradient induced by the flow in lateral channel is of order $\nabla P \sim -\frac{\eta}{h^2}U$ with η the viscosity of the solution, $h \sim 100\,\mu$m the height of the microfluidic chamber and U the velocity of the injected solution. This pressure gradient is transmitted through the gel walls to the microfluidic chamber and induces flow along the chamber thanks to the porosity of the gel. At steady state, the drift in the chamber is related to the pressure gradient by the Darcy relationship $V_{dr} = -\frac{\kappa}{\eta}\nabla P$ (b). For a flow velocity $U \sim 5\,$cm$/s$ and a Darcy permeabil-

pear trivial but actually constitutes an essential test. First, the reproducible and reliable absence of leakage is not an easy task to reach in microfluidics. Second, devicing an observation chamber maintened at rest with residual drifts of only a few nm/s goes far beyond the standard accuracy required in microfluidics, even for pressure-driven flows.

Sedimentation

We use 200 nm latex colloids with a sedimentation length $\delta = k_BT/mg \sim 100\,\mu$m, with k_B the Boltzmann constant, T the room temperature, m the boyant mass of colloid and g the gravity[6]. δ is thus of the same order of magnitude as the height of the microfluidic chamber ($h \sim 120\,\mu$m) which provides a reasonable vertical uniformity of the colloid concentration. Additionally, the sedimentation velocity[7] $v_{sed} = mg/6\pi\eta R$ for these particles is typically $v_{sed} \sim 1$ nm/s which ensures a weak effect of the sedimentation during the typical time of an experiment ($\sim 1-2$ h). Finally, combined with the solute gradient calibration by fluorescence, these control experiments and order of magnitude calculations demonstrate that our microfluidic device can **generate a tunable and steady gradient in a chamber containing particles with no convective flow and without any leakage**.

ity $\kappa \sim 500nm^2$ (extracted from the litterature for a 3% agarose gel [48]), we obtain $V_{dr} \sim 2.5$ nm/s which is in reasonable agreement with what we observed experimentally.

[6] This result will be discussed thoroughly in chapter 3.

[7] η being the viscosity of the fluid and R the radius of the colloid.

2.2.3 Analysis of the experiments

Quantitative analysis

In order to quantify the diffusio-phoretic motion, we plot in figure 2.4-b the time dependent location of the colloid population. It is defined as the maximum of the fluorescence intensity profile, measured using image analysis (Matlab)[8]. As can be seen, the observed drift is close to linear with a slight deviation observed at long times. Neglecting the transient regime (lasting about 30-60s for salt, see section 2.1), the stationary salt concentration takes the form: $c(x) = \frac{c_0}{2}(1 \pm 2\frac{x}{\ell})$, with ℓ^{-1} the slope of the concentration gradient, and x the distance to the center of the observation channel. Using the expression of the diffusio-phoretic velocity $V_{DP} = D_{DP}\frac{\nabla c}{c}$ (see Eq-1.32) in a steady linear concentration (see Eq-2.2), the position X_0 of a colloid obeys the equation:

$$\frac{dX_0}{dt} = \pm D_{\mathrm{DP}} \frac{1}{\left(\frac{\ell}{2} \pm X_0\right)}, \qquad (2.3)$$

$\pm$ depending whether the source is the side channel on $\pm\ell/2$. Initially, all colloids are concentrated at a position $X_0(t=0) = \mp w/2$ where w denotes the width of the central channel. For

[8]The process is the following. First, the intensity profile is averaged on the all picture to give a 1D profile. Then the maximum of the profile is determined. In order to limit the influence of intensity fluctuations in the profile, a local quadratic fit of the intensity is carried to determine the position of the maximum of intensity, X_0.

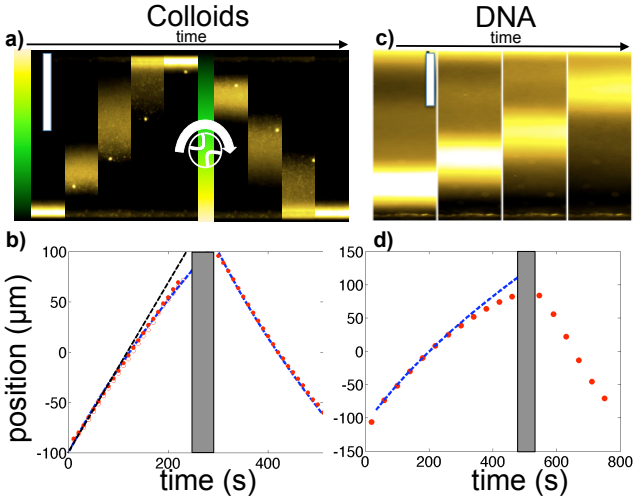

Figure 2.4: **Diffusiophoretic transport of fluorescent colloids and λ-DNA under a LiCl gradient.** (Δc_s[LiCl] $= |c_2 - c_1| = 100$ mM with a 1 mM buffer in both channels to fix the pH (TRIS buffer for colloids and TRIS-EDTA buffer for DNA). Central channels are 200 μm (a) or 300 μm (c) wide with an identical $\ell = 800\,\mu$m, scale bar 100μm). *(a)-(c)*). **Motion of particles under a salt gradient**, sketched by the lateral bar, towards higher salt concentrations. Images are separated by 90 s for the colloids and for DNA the images were taken at t =100, 150, 200, 300 s. *(b)-(d)* **Time evolution of the particles population location** characterized by the maximum in particles density (measured from fluorescence intensity). Experimental data (symbols) are fitted according to the theoretical description Eq-2.3 (dashed lines), with D_{DP} as the only fitting parameter (see text). In (b), open symbols correspond to a subsequent migration, and fully superimposes on the previous results. The solid straight line in (b) is a guide line corresponding to constant drift velocity. Shaded regions correspond to time periods where wall effects prevent from proper fluorescence measurements.

short times $dX_0/dt = \pm 2D_{DP}/(\ell \mp w)$ and the maximum of the colloid density exhibits a quasi-linear dependence on time, as observed experimentally in figure 2.4-b. For longer time, slight deviations from the linear dependence are expected from equation 2.3 and indeed observed in figure 2.4-b. Physically, these non-linearities in $X_0(t)$ take their origin in the logarithmic-sensing obeyed by the diffusio-phoretic phenomenon, *i.e.* the fact that the velocity is proportional to the gradient of the logarithm of the concentration (see Eq-1.32). The diffusiophoretic velocity V_{DP} is thus expected to decrease during the migration in a linear solute profile. Furthermore, given the experimental initial conditions $X_0(t=0) = \mp w/2$, equation 2.3 can be analytically solved and leads to:

$$D_{DP}t = \begin{cases} X_0^2/2 + \ell X_0/2 - w^2/8 + w\ell/4 & \text{if } c(\ell/2) = c_0 \\ X_0^2/2 - \ell X_0/2 - w^2/8 + w\ell/4 & \text{if } c(-\ell/2) = c_0 \end{cases} \quad (2.4)$$

Overall, Eq-2.4 provides an excellent fitting expression for the experimental data (Fig. 2.4-b) and gives access to the colloids diffusio-phoretic mobility D_{DP} (see Table 2.5). We used this method to measure D_{DP} for various salts and obtain the diffusio-phoretic mobility of latex colloids with great accuracy for LiCl. For NaCl and KCl salt, the migration is slower and the diffusive spreading of the colloid population increases. The determination of the maximum X_0 becomes less accurate which affects the diffusio-phoretic mobility D_{DP} determination. Alternatively, diffusio-phoretic mobilities can be determined with the total crossing time T_{cr}, rather than the full dynamics of the

population maximum. Indeed, equation 2.4 for $t = T_{cr}$ rewrites $D_{DP}T_{cr} = f(w, \ell)$, where f depends only on geometrical parameters: w and ℓ, fixed on a serial of experiments. Given a couple (T_{cr}, D_{DP}) for a salt, the diffusio-phoretic mobility D'_{DP} of an unknown salt can thus be determined measuring the crossing time T'_{cr} following:

$$T'_{cr}/T_{cr} = D'_{DP}/D_{DP}$$

This "integrated" method yields to D_{DP} similar to the values determined by fitting without describing the complete displacement $X_0(t)$. In the case of colloids, the diffusiophoretic mobility was measured for three different salts, exhibiting values for the mobility in the order LiCl>NaCl>KCl (see Table 2.5). This salt specifity effect is predicted by the theory. As a quick reminder, it takes its origin in the difference of diffusivity between anions and cations of a salt and consequent self-induced-electrophoresis (electro-phoretic contribution of diffusio-phoresis, see section 1.2.2-*ion specificity* in the previous chapter).

While most of the experiments have been conducted with colloids in salt gradients, the physical mechanism explored is not limited to this "colloids in electrolytes" configuration. We then turn to the diffusio-phoretic migration of alternative systems such as "biological colloids" (DNA) in salt gradient or colloids in a neutral solute: hydrogen peroxyde.

Salt		Colloid LiCl	Colloid NaCl	Colloid KCl	DNA LiCl
D_{DP} (μm^2/s)		290 ± 5	150 ± 10	70 ± 10	150 ± 20
$(K\ell^2/k_BT)^{1/2}$	Exp.	22 ± 2	16 ± 1.5	N.A.	12.5 ± 3
	Theo.	23 ± 0.5	16.5 ± 1	13 ± 2	16.5 ± 1

Figure 2.5: **Value for the diffusiophoretic mobility** D_{DP} extracted from the channel crossing experiments (see text). Experimental trap strength K extracted from the trapping experiments (see section 2.3) and compared to the predicted value from Eq-2.8.

Diffusio-phoretic migration of biological macromolecules

First, the moving particles are not bound to be spherical colloids but can also be macromolecules. As a demonstration, the same motility experiments as presented above in figure 2.4-a,b were also conducted with λ-DNA: phage-λ DNA (48kbp, Fermentas, Germany) diluted 10 times in Tris-EDTA buffer is enclosed in the microfluidic chamber (see Appendix B and C of this chapter for more experimental details). A salt gradient -LiCl, NaCl, KCl- is imposed *via* the boundary conditions in the hydrogel microfluidic chamber. The solute gradients induces the migration of the *biological colloid* (gyration radius of typically 200 nm) towards the high concentration of salt (see Fig. 2.4-c,d). We then demonstrate the motion of DNA molecules under salt concentration gradients. The determination of the diffusio-phoretic mobility of DNA by the fitting method is more tedious as the non linearity of the velocity is much higher for the experiment than for

simple diffusio-phoresis predictions (see Table 2.5). This result shows that the simple prediction (Eq 1.32) derived for spherical solid colloids does not fully capture the specifity of the dynamics of a complex macromolecule as DNA. For example, the gyration radius of DNA can depend on the salt concentration through the screening of charges as well as the zeta potential of this polymeric ball. Nevertheless we confirme the diffusiophoretic migration of DNA towards higher concentrations of salt.

Diffusio-phoretic migration in a neutral solute

As a final remark, we emphasize that salt is used here because of its simplicity, other solutes could be used as an alternative. Theoretically, a diffusio-phoretic migration will occur with any solute having non-vanishing interactions with the particle [15, 23], while the details of such interaction (attractivity, repulsivity, strength, etc.) determines the amplitude and direction of the particle response. Experimentally, the diffusio-phoretic response with neutral polymer as solutes have indeed been recently observed [36]. We here further demonstrate experimentally the diffusio-phoretic migration with a non-charged specie: the hydrogen peroxide H_2O_2 solution. In contrast to LiCl, NaCl or KCl salt gradients, latex colloids escape the high concentration of hydrogen peroxide. H_20_2 acts as a repellent for latex colloids ($D_{DP} < 0$)[9].

[9] This sign for D_{DP} must originate at microscopic scale in a depletion of H_2O_2 molecules at the solid latex surface according to Eq-1.19.

To summarize, we have shown that the diffusio-phoretic migration of particles in electrolyte thus exhibits three main features: motility driven by concentration gradient, salt specificity effects and logarithmic-sensing. Moreover, the logarithmic expression of the velocity $V_{DP} = D_{DP}\nabla \log c$ presents two specificities: *(i)* it is non linear and *(ii)* the velocity "diverges"[10] when the solute concentration goes to zero. In the following, we will address each of this point and show how it leads to versatile and interesting localization processes.

[10] In the limit of our model

2.3 Trapping by rectified diffusio-phoresis

As noted previously, the diffusio-phoretic motion in electrolyte gradients is characterized by a logarithmic-sensing which introduces a slight non-linearity in the velocity to concentration relationship. Such a non-linearity actually suggests that under periodic oscillations of the salt gradients, a rectification of the particles motion may be induced: we now explore this feature for particles trapping and patterning.

2.3.1 Osmotic trapping of colloids

While the diffusiophoretic migration was studied under a stationary gradient, we now generate concentration gradients oscillations as in figure 2.2-b,c by periodic inversions of the concentration boundary conditions (period T_0). As stated in the previous section, we choose $T_0 \sim 6 - 10$ mins depending on the salt and therefore on the crossing time. We start from an homogeneous concentrated population of colloids (F8888, 200 nm, Molecular Probes) in the central chamber[11]. After each oscillation the population of colloids is depleted close to the wall of the channels and after 3-4 oscillations, the colloids are trapped in the center of the channel. The period of oscillations is then reduced and the band keeps oscillating around the center with the

[11] As previously detailed the concentration profile of the colloids inside the chamber is imaged by the spatial fluorescence intensity in the chamber with a 20x objective. The fluorescence intensity is strongly attenuated by microscope filters and shutted between pictures to limit colloids bleaching phenomenon.

salt cycles, but its width remains stationary. The experiment is shown in Fig. 2.6-a) for colloids: starting from a homogeneous distribution, the particles population evolves after a few cycles towards a band with a stationary width. This band is Gaussian to a very good approximation (see Fig. 2.6-a). Note that the process is robust: starting from inhomogeneous particles distribution, or changing the oscillation frequency -*within our limited accessible range as specified earlier*- yields the same width for the trapped band. Finally as for the colloids motility, the width of the trapped band depends on the salt nature: LiCl > NaCl > KCl in terms of trapping efficiency.
Additionally, we also performed similar experiments with λ-DNA as motile particles: Fig. 2.6-b) shows that trapping is equally achieved with macromolecules, namely *biological colloids*, the latter gathering also in a narrow band with Gaussian profile. Despite a slow migration of DNA and a low D_{DP} which should *in principle* limit the trapping efficiency, the experimental observations show very effective localization. This originates in the strong non-linearity of the DNA diffusio-phoretic migration (see figure Fig. 2.4-b): the front particles nearly stop while the back ones still advance. This makes the trapping easy and efficient.

2.3.2 Principle in a nutshell

We now present a cartoon picture that captures the physics at work in the phenomenon of particles segregation observed during experiments with oscillating concentration gradients. Consider that one syringe pump contains a salt with given concen-

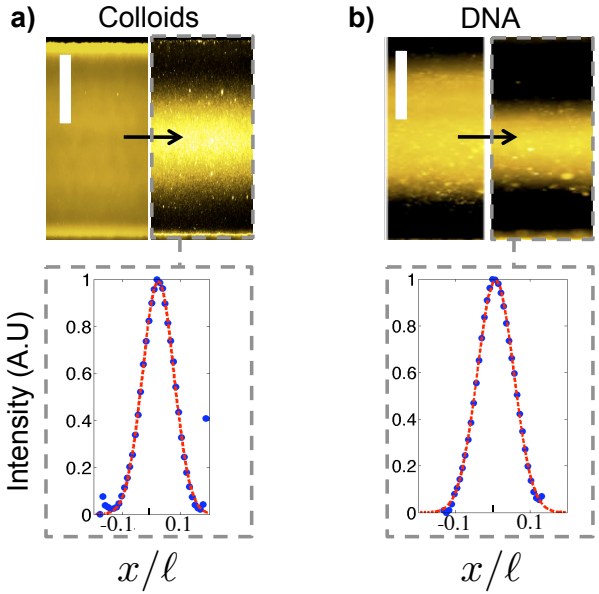

Figure 2.6: **Trapping under salt gradient oscillations.** Trapping of colloids, (a), and λ-DNA with YOYO-1, (b), under salt gradient oscillations (buffers and salt concentration as in Fig. 2.4; $T_0 = 600\,\mathrm{s}$). *(Top)*: Starting from a homogeneous population, the particles focus to a band of stationary width (scale bar 100μm), independent of the oscillation frequency (300 μm width channels with 250 μm gel walls). (*Bottom*): symbols, experimental particles density profile in stationary state, as obtained from the fluorescence images; dashed line, Gaussian fit from which experimental trapping strengths K are deduced through $K = k_B T/\sigma^2$, with σ the Gaussian width. They are compared to theoretical expectations according to Eq-(2.8) in Table 2.5.

tration c_0 while the other syringe contains only buffer. For the sake of simplicity, we will first suppose that the linear steady profile of the gradient is instantaneous reached after a reversal of the boundary conditions *i.e.* we neglige the transient regime. Initially, we suppose that the high concentration of the salt is on the right side of the chamber: *source on the right, sink on the left* (see Fig. 2.7) . A colloid on the left side on the chamber at $t = 0$ will migrate to the right thanks to diffusio-phoresis phenomenon (see Fig. 2.7-a). After a time $T_0/2$, the colloid has crossed a part of the chamber and the salt gradient is reversed. The colloid attracted by the high concentrations of salt reverse the direction of its motion and migrates to the left (see Fig. 2.7-b). At time T_0, the concentration gradient is reversed and so on... After one period and a complete oscillation of the boundary conditions, the colloid has experienced a net displacement to the center of the chamber (see Fig. 2.7-c). After a few oscillations, any colloid initially in the chamber ends up in $x = 0$. In other words, under a constant solute gradient, the velocity of particles is larger in regions with smaller solute concentration. Accordingly, the front particles move slower than the ones at the back: iterated over the oscillations, such a process leads to the observed focusing. This phenomenon takes its origin in the logarithmic-sensing of the diffusio-phoretic migration in electrolyte solutions (see Eq-1.32). The distance covered during the first half-period $[0; T_0/2]$ is not the same during the second half-period $[T_0/2; T_0]$. After one period the colloid motion is therefore rectified towards the center of the channel.

Through this cartoon, we have pictured the phenomenon of trapping by rectified oscillations of concentrations.

From cartoon to real life: time scales in the real experiment.
In the cartoon picture of the trapping phenomenon we neglect –for the sake of simplicity– the transient state of the gradient. Nevertheless as we pinpointed in section 2.1, after a switch of the syringe, the side channels must be refilled by the new solution and boudary conditions need finite time to diffuse from the side channels to the microfluidic chamber. Therefore, a *real* experiment is slightly more complex that the previous sketch. Experimentally, the trapping scenario must take into account 3 different time scales: the transient time T_{tr} to refill the side channels and for the salt to diffuse through ℓ, the time T_{cr} for a colloid to cross the chamber and finally the oscillation period T_0 of the concentration gradient. In order to follow the trapping scenario, T_0 is smaller than T_{cr}. In addition, to limit limit-size effects and accumulation of colloids blocked along the chamber walls, T_0 must be taken much lower than the crossing time. But it must also be bigger than the transient time T_{tr} to assume rectified linear concentration gradient with good approximationAn *ideal* trapping experiment thus follows $T_{tr} \ll T_0 \ll T_{cr}$.
With constant $\ell = 800\,\mu$m in all experiments, the transient time is $T_{tr} \sim 30 - 60\,$s (see section 2.2) and the crossing time $T_{cr} \sim 7 - 15\,$mins. Given the experimental parameters – given channel geometry and colloids– the oscillation period is the only experimentally tunable parameter. It is chosen in the range 6 to 10 mins *i.e.* the time for colloids to cross typically 1/5 to 1/3 of the channel.

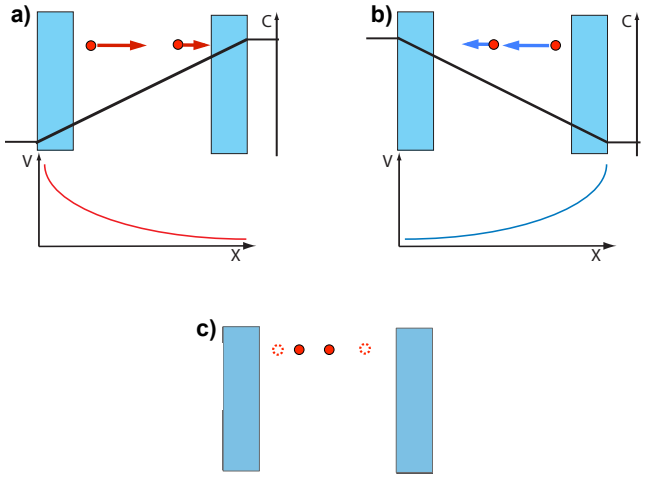

Figure 2.7: **Sketch of the phenomenon of trapping by rectified oscillations of concentrations.** We suppose instantaneous reversals of the steady linear concentration profile (solid black line). The boundary conditions oscillate with a period T_0. Only the microfluidic chamber containing the colloids (red circles) is represented with the gel walls (blue). Color arrows stand for the colloids displacements.For clarity, effects are accentuated. The velocities are represented accordingly to equation 1.32: $V \sim \nabla c/c$. *(a)* $0 < t < T_0/2$, the source channel on the right, the sink is on the left. The colloids migrate towards the high concentration of salt, *i.e.* on the right. The colloid on the left is faster than on the right given the expression for the diffusio-phoretic velocity. At $T_0/2$, the boundary conditions are reversed and the reversed linear profile is instantaneously reached. *(b)* $T_0/2 < t < T_0$, the migration is reversed to the right towards the regions rich of salt. Once again, the colloid in the lower concentration region is faster. (c) After one oscillation, the colloids has experience a net displacement to the center. This trapping effect is thus a direct consequence of the non linear dependance of the velocity with the concentration.

2.3.3 Theoretical Predictions

In order to get further insight into the trapping mechanism at work, we have conducted a detailed investigation of the particles dynamics. As we now show, the trapping of the particles results from the rectification of their motion under the oscillating driving field of the salt concentration. The rectification is accordingly induced by the non-linear sensing of the diffusiophoretic motion, $V_{DP} \propto \nabla[\log c]$ (see Eq-(1.32)) where $c(x,t)$ stands for the salt concentration field.

Our starting point for the modelization is the Smoluchowski equation for the particles concentration, $\rho(x,t)$, here coupled to the salt diffusive dynamics:

$$\begin{aligned} \partial_t \rho &= -\nabla \cdot (-D_c \nabla \rho + D_{\rm DP} \nabla[\log c]\rho) \\ \partial_t c &= D_s \Delta c \end{aligned} \qquad (2.5)$$

with D_c the particle diffusion constant, D_s that of the salt with concentration c and $D_{\rm DP}$ the particle diffusio-phoretic mobility. These equations are coupled to the time-dependent boundary conditions for the salt concentration: every $T_0/2$, the salt concentration at the boundaries switches from 0 to c_0 for one side and vice-versa for the other side. At time $t = 0$ the particles repartition is chosen homogeneous[12]. The geometry fits that of the experiments, with particles confined in the central channel while the salt gradient develops over the central channel and the gel walls.

[12] But various initial conditions of the particles population could be implemented.

Numerical Resolution

In a first step, the above coupled equations 2.5 are solved numerically using Matlab®. The geometry as well as the boundary conditions match the experiments. The salt concentrations in the side channels oscillate with a stepwise function of period T_0. Accordingly the gel walls are implemented in the numerical simulations as impermeable frontiers *only for particles* and a free-diffusion medium for salt.
The problem is made dimensionless, using ℓ as the unit of length and determining the unit of time with D_s. Additional variables are the following: $\tilde{x} \equiv x/\ell$, $\tilde{t} \equiv t/\tau$ with $\tau \equiv \ell^2/D_s$. And the diffusion coefficient expresses in units of the salt diffusivity: $\tilde{D}_s = 1$, $\tilde{D}_c \equiv D_c/D_s$ and $\tilde{D}_{DP} \equiv D_{DP}/D_s$. For an mulitvalent electrolyte solution for which anion and cation do not present the same diffusivity, the salt diffusivity is defined as $D_s = \frac{(|z_-|+z_+)D_-D_+}{z_+D_+ + |z_-|D_-}$ where D_+ and D_- the diffusivities of the consituent ions and z_+ and z_- their valence [23]. In the following, $\tilde{D}_c$ is set to 0.0016 to match the experimental value for colloids of diameter $\Phi = 200\,\text{nm}$ in a LiCl salt. Finally, the coupled partial equations are solved with Matlab in 1D with D_c/D_{DP} as the variable parameter.
Results are shown in figure 2.8-a. Starting from a homogeneous spatial distribution of colloids in the channel, after a short transient of a few oscillations the particles population focuses within a band with a stationary and constant width. In these simulations the oscillation period $T_0 = 470\,\text{s}$ is chosen as in the experiments. We checked that except for the first oscillation the wall effects are limited and that the trapped state is not a con-

sequence of the accumulation of the colloids against the wall. The colloids population is additionally very well described by a Gaussian distribution (see Fig. 2.8-b) while its center position oscillates with the solute oscillations, as observed experimentally. We also checked that the trapped state does not depend on the initial conditions: a homogeneous as well as a dirac-like distribution relax to the same steady Gaussian distribution. Moreover we tested the independence of the trap with the oscillation period T_0 varying the period in the same range as in the experiments Numerical simulations allow to test conditions that are not accessible in our experiments as very thin gel walls which experimentally do not prevent from leakage. Indeed we could suppress gel walls in our simulations[13] to increase the range of accessible T_0. Once again, modifying the oscillation frequency does not affect the final state.

Consequently the final Gaussian state depends neither on the oscillation period nor on the initial distribution of colloids nor on the presence of confining walls.

Finally we explored numerically the influence on the trapped state of the ratio D_C/D_{DP} in the range 10^{-2} to typically unity. For $D_C/D_{DP} < 10^{-2}$, *ie* high diffusio-phoretic mobility, the colloid migration is fast and the assumption of time scale separation between transient gradient and crossing-time breaks. Therefore colloid population goes from one side to the other and "crashes" the gel walls systematically. The distribution is never steady and artificially narrowed by periodic blockage against the wall.

[13]The removal of the walls does not affect the transient time T_{tr} as the length scale ℓ is not modified and the salt freely diffuses in walls.

For low diffusio-phoretic mobility $D_C/D_{DP} > 1$, the colloid migrates so slowly that the thermal diffusion spreads the distribution in the whole channel. The population is weakly trapped and as a large number of colloids is close to the walls, side effects can not be neglicted anymore. In the range $10^{-2} < D_C/D_{DP} < 1$, the numerical results suggest a width of the Gaussian distribution σ scaling as $\sigma \propto \ell\sqrt{D_c/D_{\mathrm{DP}}}$, with a prefactor $1/2$ (see Fig. 2.8-c).

Asymptotic model

A simple asymptotic interpretation of the above results can be proposed. First, due to the fast salt diffusion, one may neglect the gradient establishment thanks to the diffusion of the boundary conditions. The solute concentration profile thus writes as:

$$c(x,t) = c_0/2 + c_0 f(t) x/\ell \qquad (2.6)$$

with x distance to the channel center, $\ell \equiv c/\nabla c$ the distance over which the gradient establishes and $f(t)$ a time-dependent function, oscillating with the salt concentration oscillation periodicity T_0. Typically in our experiments, $f(t)$ is a ± 1 step-function, in the limit of immediate renewal of the side channels solutions, so that $\langle f(t)\rangle = 0$ while $\langle f(t)^2\rangle = 1 \neq 0$, with $\langle\cdot\rangle$ the time average over T_0.
Now, as in the first part of the study, the mean position $X_0(t)$ of the particle population is expected to obey Eq-2.3. For small excursions around the center ($X_0 \ll \ell$), one can write

$$dX_0/dt \simeq 2D_{\mathrm{DP}} f(t) \left[1 - 2f(t)(X_0/\ell) + \ldots\right]/\ell \qquad (2.7)$$

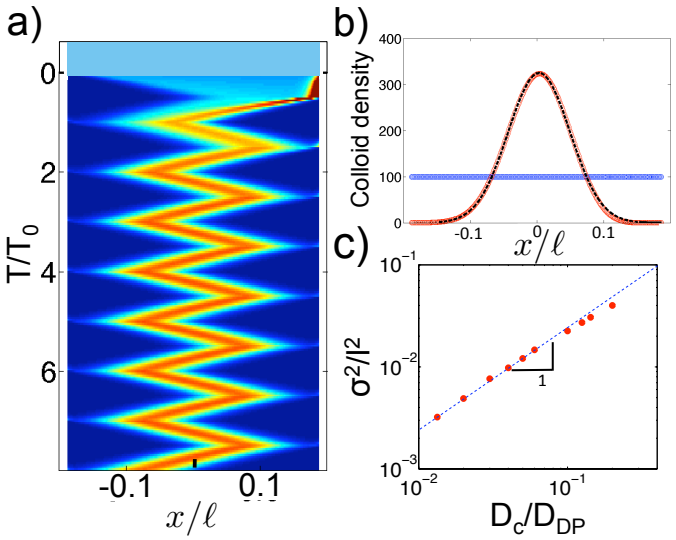

Figure 2.8: **Numerical resolution of the particles dynamics under oscillating salt gradients**: *(a)* **Spatio-temporal evolution of the colloid density** ρ, where parameters have been set according to experiments Fig. 2.6-a): for $D_s = 1360\,\mu\text{m}^2/\text{s}$, $D_c/D_s = 0.0016$, $D_c/D_{\text{DP}} = 0.01$, $\ell = 800\,\mu\text{m}$, $w = 300\,\mu\text{m}$ and $T_0 = 470\,\text{s}$. White borders represent the gel walls. The color code ranges from blue (low density) to red (high density). *(b)* **Instantaneous particles distribution**: (blue circles) initial distribution, $t = 0$; (red circles) stationary state distribution; (dashed line) Gaussian profile fit. *(c)* **Evolution of the normalized squared Gaussian width** $(\sigma/\ell)^2$ as extracted from figure 2.8-b) as a function of D_c/D_{DP}: (red cercles) numerical simulations; (dotted line) fit with linear relationship, according to theoretical prediction (Eq-2.8).

In this limit of fast salt oscillations[14], one expects the distribution in steady state to behave to leading order as $\rho(x,t) \simeq \bar{\rho}(x - X_0(t))$, *i.e.* the distribution is steady in the reference of the mean position of the population. Inserting this guess into the Schmoluchowski equations for the particles gives:

$$\begin{aligned} \mathbf{J} &= -D_c \nabla_x \rho + V\rho \\ &\simeq -D_c \nabla_x \bar{\rho} + \tfrac{2D_{\rm DP} f(t)}{\ell} \left[1 - 2f(t)(X_0/\ell)\right] \times \bar{\rho} \end{aligned}$$

Making the variable change yields $\delta x = x - X_0(t)$ and averaging out the fast salt variables yields to $\langle J \rangle = -D_c \nabla_{\delta x} \bar{\rho} + (4D_{\rm DP}/\ell^2)\langle f^2 \rangle \delta x \times \bar{\rho}$. Altogether, at steady state $\langle J \rangle = 0$, we predict a stationary Gaussian distribution for the particles:

$$\bar{\rho}(\delta x) \propto e^{-\frac{\delta x^2}{2\sigma^2}} \text{ with } \sigma = \frac{1}{2}\sqrt{\frac{D_c}{D_{\rm DP}}}\,\ell \qquad (2.8)$$

The gaussian distribution is steady in the reference of the mean position X_0 and oscillates as a whole around the channel central position.

The asymptotic model stresses the origin of the trapping. The non linearity of the diffusio-phoretic velocity gathers the particles ultimately up to a Dirac distribution, while the natural thermal diffusivity of the colloids widens the trap. Finally the steady state is of Gaussian shape with a width which results from the balance between the diffusio-phoretic narrowing and the Brownian

[14] corresponding to fast gradient oscillations compared to the time evolution of the colloids distribution $T_1' \sim \ell^2/(4D_{\rm DP})$

motion spreading.
The predicted Gaussian shape and the expression of its width are in full agreement with the above numerical resolution of the coupled dynamics (see Fig. 2.8-b,c). Indeed the the numerical results collapse on the master curve derived from this asympotic model with small discrepancies only observed in regimes for which the wall effects are not negligible ($D_C/D_{DP} > 1$) or for which the time scale separation assumption clearly breaks ($D_C/D_{DP} < 10^{-2}$).
We also point that this trapping process can be formally interpreted in terms of an harmonic "osmotic" trapping potential,

$$\mathcal{V}_{\rm trap}(x) = \frac{1}{2}\frac{k_{\rm B}T}{\sigma^2}x^2. \qquad (2.9)$$

While the $k_{\rm B}T$ prefactor suggests an entropic origin, the trapping process is non-equilibrium in its root. Furthermore, the trapping strength is accordingly characterized by an harmonic strength $K = k_{\rm B}T/\sigma^2$. The experimental values for the measured trapping strength K are gathered in Table 2.5 for various salts. These are compared to the theoretical predictions, in which $D_{\rm DP}$ was set to the mobility measured independently in channel-crossing experiments (Fig. 2.4). Results in Table 2.5 show a good agreement between experimental trapping and predicted theoretical values from Eq-(2.8). A final important remark is that the trapping potential is strong: over the cell-chamber scale –with overall size ℓ– the trapping free-energy well has a depth of $\Delta\mathcal{F} \approx k_{\rm B}T\frac{D_{\rm DP}}{D_c} \sim 100k_{\rm B}T$.

2.3.4 Pattern symmetry versus temporal signal

We now generalize the previous results to more complex geometries in order to demonstrate the robustness and generic character of the above scenario. To this end, we have tested this segregation phenomenon in a circular, "cell shaped", chamber.

Experimental observations

The experimental setup is derived from the previous experiments replacing a rectangular by a circular chamber and modifying the side channels in order to impose a gradient of circular geometry. A sketch of the channels is represented in figure 2.9-a,b: a circular chamber (650 μm in diameter) is surrounded by two side-channels conveying the salt and the particles –here colloids with 200 nm of diameter – are initially homogeneously spread in the chamber. Two different concentration gradient forcings are explored: an *antisymmetric forcing* where the salt boundary concentrations c_1 and c_2 are switched periodically between 0 and c_0 with antisymmetric phase as in the previous section; and a *symmetric forcing* where $c_1 = c_2$ switches periodically between 0 and c_0 in phase . We want to stress here that the origin of the diffusio-phoretic migration depends on the nature of the forcing. The colloids move thanks to the steady concentration gradient in the antisymmetric driving, but the transient gradient -between two steady states of constant salt concentration- is the source of the migration in the symmetric case.
As demonstrated in figures 2.9-c,d, the salt oscillations again

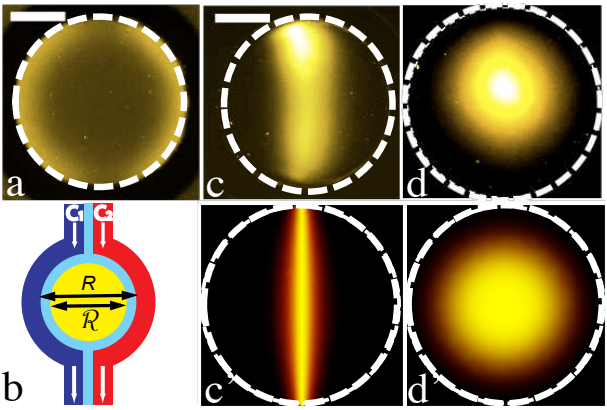

Figure 2.9: **Trapping of colloids in a "cell-shaped" chamber, under anti-symmetric and symmetric time-dependent salt concentration oscillation.** *(a)-(b)* Initial colloids distribution (fluorescence image) and sketch of the experimental set-up, the light blue represents the gel. The concentration of the salt (here LiCl) in the two side channels, $c_1(t)$, $c_2(t)$, oscillates (period $T_0 = 480\,\mathrm{s}$) either anti-symmetrically, $c_1(t) - \langle c_1 \rangle = -[c_2(t) - \langle c_2 \rangle]$, or symmetrically $c_1(t) = c_2(t)$, between $c_0 = 0$ (TRIS buffer alone) and 100 mM. Circular well is $650\,\mu$m in diameter with gel walls 125μm wide ($\ell = 900\,\mu$m; scale bar $200\,\mu$m). *(c)* Stationary colloidal distribution under an *antisymmetric* concentration gradient driving. It takes the form of a band dividing the cell-chamber and centered in the middle plane. *(c′)* Theoretical prediction for the stationary colloid density profile under antisymmetric concentration gradient driving, the predicted expression (see section 2.3.4-*antisymmetric forcing*) with the parameters set to the experimental values. *(d)* Stationary colloidal distribution under a *symmetric* concentration gradient driving. It takes the form of an axi-circular shape centered in the cell-chamber. *(d′)*. Theoretical prediction for the stationary colloid density profile under symmetric concentration gradient driving, using the predicted expression (see section 2.3.4-*symmetric forcing*) with the parameters set to the experimental values.

produce a localization of the particles in the cell chamber (see also supplementary movies 3 and 4). Furthermore the symmetry of the pattern depends directly on the symmetry of the driving: one observes a linear localization with a"cat eye" shape for the antisymmetric driving, and a circular egg-shape localization for the symmetric driving. This demonstrates the versatility of the trapping process. Once again, we observed experimentally that this localization process is also robust versus the initial distribution of the particles.

Theoretical predictions

These different experimental patterns can be understood along similar lines as above. A prediction for the trapping potential associated with the particles localization is obtained by averaging out the fast salt variables.
We consider the circular cell-like configuration sketched in Fig. 2.9. The colloids are embedded in an inner chamber with diameter $\mathcal{R}$, while the salt boundary condition ring has a diameter R (see Fig. 2.9-b). The salt concentration $c(r, \theta, t)$ obeys the diffusion equation

$$\partial_t c = D_s \Delta c$$

with boundary conditions depending on the nature of the forcing.

Antisymmetric forcing
For the antisymmetric geometry with T_0-periodic temporal inversion of the boundary conditions, the boundary conditions

rewrites with the polar coordinates r, θ:

$$\text{For } 0 < t < T_0/2,\ c(R/2,\theta,t) = \begin{cases} c_0 & \text{if } \theta \in [0;\pi] \\ 0 & \text{if } \theta \in [\pi;2\pi] \end{cases}$$

$$\text{For } T_0/2 < t < T_0,\ c(R/2,\theta,t) = \begin{cases} 0 & \text{if } \theta \in [0;\pi] \\ c_0 & \text{if } \theta \in [\pi;2\pi] \end{cases}$$

As for the 1D linear geometry, we neglect the gradient establishment due to the diffusion of the boundary conditions and consider only the steady concentration profile given by $\Delta c(r,\theta,t) = 0$. The solution of this equation given the boundary conditions takes the form:

$$c(r,\theta,t) = \frac{c_0}{2}\left[1 + \frac{\delta(r,\theta)}{R/2}\, f(t)\right] \tag{2.10}$$

with $\delta(r,\theta) = \frac{4}{\pi}\sum_{k,odd}\frac{1}{k}\,(r)^k \sin[k\theta]$, and $f(t)$ the periodic step-like function with period T_0. Averaging over the flux of particles over the fast salt oscillations the stationary colloid density profile is then obtained as

$$\rho[r,\theta] \propto \exp\left[-\frac{1}{2}\frac{D_{DP}}{D_c}\frac{\delta(r,\theta)^2}{(R/2)^2}\right] \tag{2.11}$$

Symmetric forcing

For the symmetric geometry, a *uniform* ring of salt oscillates periodically between 0 and c_0 and the boundary conditions take the form:

$$c(R/2,\theta,t) = c_b(\theta,t) = \begin{cases} c_0 & \text{for } 0 < t < T_0/2 \\ 0 & \text{for } T_0/2 < t < T_0 \end{cases}$$

which rewrites with Fourier series:

$$c_b(\theta,t) = \frac{c_0}{2}\left(1 + \frac{4}{\pi}\sum_{k,odd}\frac{1}{k}\sin[k\omega t]\right)$$

$$= \frac{c_0}{2}\left(1 + \frac{4}{\pi}\sum_{k,odd}\frac{1}{k}\mathrm{Im}[\exp(jk\omega t)]\right)$$

with $\omega = 2\pi/T_0$.
Here the steady concentration is uniform and one has to take into account the transient concentration profile. One obtains the salt concentration in the form

$$c(r,t) = \frac{c_0}{2}\left[1 + \delta(r,t)\right]$$

with $\delta(r,t) = \frac{4}{\pi}\sum_{k,odd}\frac{1}{k}\mathrm{Im}\left(f_k(r)\exp[j\,k\omega\,t]\right)$.
For each mode $k\omega$, f_k is the 2D solution of the steady diffusion equation and rewrites with the Bessel function of order 0 $I_0(r/\delta_k)$, with $\delta_k = \sqrt{\frac{jD_s}{k\,\omega}}$, the salt diffusive length. By superposition, the salt concentration rewrites:

$$c_b(r,t) = \frac{c_0}{2}\left(1 + \frac{4}{\pi}\sum_{k,odd}\frac{1}{k}\mathrm{Im}\left[\exp(jk\omega t)\frac{I_0(\frac{r}{\delta_k})}{I_0(\frac{R}{2\delta_k})}\right]\right)$$

It gives, developing the logarithm and averaging over the fast salt variables

$$\log c \sim \log \frac{c_0}{2} + \frac{1}{2}\left(\frac{4}{\pi}\right)^2 \sum_{k,odd} \frac{1}{k^2} I_0^2\left(\frac{r}{\delta_k}\right)\frac{1}{2}$$

Finally, one gets the asymptotic[15] colloid density as:

$$\rho[r] \propto \exp\left[-\frac{1}{4}\frac{D_{DP}}{D_c}\kappa_0 r^4\right] \tag{2.12}$$

with $\kappa_0^{-1} = 16\pi\delta_1^5 \cosh(R/\sqrt{2}\delta_1)/R$.

These predicted localization patterns are exhibited in Figs. 2.9-c′,d′, showing a good qualitative and semi-quantitative agreement with the experimental results, Figs. 2.9-c,d. As in the previous section, the trapping potential results again from a rectified diffusio-phoretic drift under the salt oscillations.

2.4 Localization by osmotic shock

We have already mentionned the logarithmic expression of the diffusio-phoretic velocity: $V_{DP} = D_{DP}\nabla \log c$. In the previous section, we demonstrated how we could harness the non-linearity to trap and localize particles by rectification of oscillating concentration gradients.
We now turn to the consequences of the extreme sensibility of

[15] At long times, only the term for $k = 1$ matters.

diffusio-phoresis to vanishing electrolytes concentration. Notably, it is expected from the expression of the diffusio-phoretic velocity that a vanishing gradient can lead to measurable velocity provided that the solute concentration is low enough. We explore further this point via experiments in an "osmotic shock" configuration.

2.4.1 Experimental observations

We start with a solution of 200 nm latex colloids in solution with LiCl salt of concentration $c_0 = 100\,\text{mM}$. The colloidal suspension is enclosed in a microfluidic chamber soaked with LiCl salt solution (see Fig. 2.10-a).
At $t = 0$, distilled water plus buffer is injected with the syringe-pump and the boundary conditions (BC) for the salt are thus changed from $c = c_0$ to $c = 0$[16]. The salt concentration in the chamber relaxes by diffusion and reaches in the long time limit the conditions imposed by the BC: $c = 0$. During this process, the colloids are observed to strongly concentrate in the center of the cell (see Fig. 2.10-b) and the migration surprinsingly lasts $15 - 16\,\text{mins}$. For longer time, the Brownian motion dominates, the colloids do not focus anymore and the distribution widens by thermal diffusion of the colloids.

[16] In the following, we will omit the buffer and thus write that the salt concentration is $c = 0$. The important role of the buffer will be explicitly discussed further in the section.

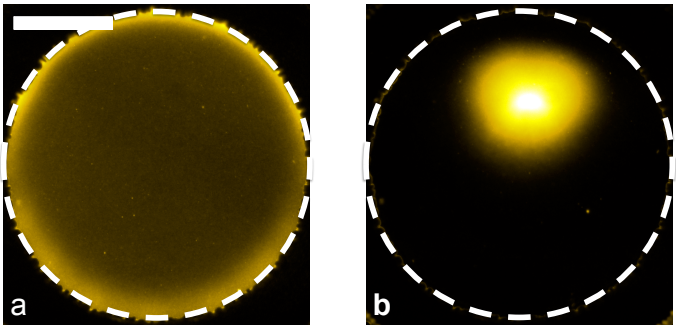

Figure 2.10: **Localization by osmotic shock.** Circular well is 650 μm in diameter with gel walls 125μm wide (ℓ = 900 μm; scale bar 200 μm). Initially, the colloid solution and the gel are in a LiCl salt solution of concentration c_0 = 100 mM of salt. For $t < 0$, salt concentration is thus homogeneous, with value c_0 in the system. *(a)* Initial colloids distribution (fluorescence image). A t=0, boundary conditions $c = 0$ is imposed by a syringe pump. And for $t > 0$, the concentration profile relaxes to reach in the long time limit $c = 0$. *(b)* The system undergoes an "osmotic shock" and the colloids move towards the high concentration of salt, *e.g.* the center of the chamber. The migration lasts up to 15 mins leading to an efficient focusing of the colloid population. The colloid distribution thereafter spreads by Brownian diffusion.

2.4.2 Principle in a nutshell

The directed motion to the center of the cell is of course of diffusio-phoretic origin as the salt concentration is higher in the center of the chamber than close to the wall (see Fig. 2.11) where the salt is sucked by side channels acting as sinks. At steady state, the salt concentration is *zero* and homogeneous. As previously discussed in benchmarks experiments, the steady state *should be* reached after $\sim$ 1 min which makes the experimental observations surprising. Actually, a key point of diffusio-phoresis *with electrolytes* originates in the expression of the diffusio-phoretic velocity $V \propto \nabla c/c$. This makes the diffusio-phoretic drift very sensitive to regions where the concentration vanishes ($c \to 0$), as long as $\frac{\nabla c}{c} \neq 0$. We anticipate that this *log-sensing* of the velocity is at the origin of the long term evolution –over 15 mins– of the colloid migration. We now present a formal derivation of the colloidal density $\rho(\mathbf{r}, t)$ under an osmotic shock. It will develop and underline the role of the logarithmic expression of the velocity in such a long term evolution.

2.4.3 Theoretical predictions

The aim of this part is to obtain the equation for the colloidal density, $\rho(\mathbf{r}, t)$. To this end we first need to describe the evolution of the solute concentration which drives the colloidal motion. The description is derived in a 2D circular cell and the parameters are set to the experimental values.

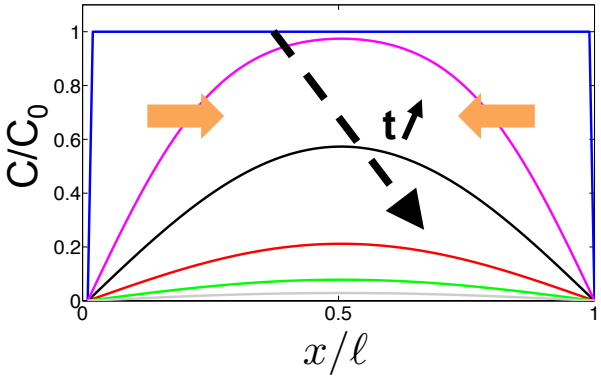

Figure 2.11: **Solute concentration evolution during an osmotic shock.** Initially, $c = c_0$ uniform (blue line). At $t > 0$, BC $c(x = 0, t) = 0$ and $c(x = \ell, t) = 0$ are imposed with side channels as sink. The solute concentration evolves and relaxes with time to $c = 0$. Numerical resolutions of the 1D diffusion equation for t =0, 20 s, 50 s, 100 s, 150 s and 200 s for LiCl salt. Orange arrows stand for the diffusio-phoretic migration of latex colloids towards high concentration of salt. Osmotic shock localization originates in the high sensibility to this solute gradient.

Solute dynamics in an osmotic shock configuration

The salt concentration c obeys the diffusion equation, together with the boundary conditions at the chamber perimeter. For the osmotic shock the boundary conditions are $c(r = R, t < 0) = c_0$ and $c(r = R, t > 0) = 0$ (same notations as for the trapping in a circular chamber).
We first determine a basis of separable functions $c = f(t).g(r)$ solutions of the time-dependent diffusion equation. We get

$$f'/f = D_s \Delta g/g = -K$$

K being a constant. Developing the Laplacian operator in cylindrical geometry to agree with the experimental geometry, g is solution of the following ODE: $r^2.g'' + r.g' + r^2.\frac{K}{D_s}g = 0$. After a change of variables $u = r.\sqrt{K/D_s}$, we obtain a Bessel equation of order 0 defined at $r = 0$ [49]. Therefore, $g(u) = J_0(u)$ where J_0 is the Bessel function of first kind. Boundary conditions of null concentration at the border impose $J_0(R.\sqrt{K/D_s}) = 0$ which lead to discrete values of K: $R.\sqrt{K_n/D_s} = \alpha_n$, with α_n the n^{th} zero of J_0.
One can thus rewrite any solution with separated variables as follows:

$$c(r,t) = \sum_n a_n \, e^{-K_n t} \, J_0 \left[r \sqrt{\frac{K_n}{D_s}} \right] \qquad (2.13)$$

The coefficients a_n are defined by the initial condition $c(r, t = 0)$[17]:

$$c_0 = \sum_n a_n J_0 \left[r \sqrt{\frac{K_n}{D_s}} \right], \text{ for r < R} \tag{2.14}$$

In the long-time limit, as $K_n > 0$ and increases with n, only the first term in Eq.(2.13) remains and

$$c(r, t) \simeq a_1 e^{-D_s \left(\frac{\alpha_1}{R}\right)^2 t} J_0 \left[\alpha_1 \frac{r}{R} \right] \tag{2.15}$$

with $\alpha_1 \simeq 2.4$the first zero of J_0. This leads to a diffusio-phoretic velocity of the following form:

$$\mathbf{V}_{DP} = D_{DP} \frac{\nabla c}{c} = D_{DP} \nabla \log J_0 \left[\alpha_1 \frac{r}{R} \right] \mathbf{e}_r \tag{2.16}$$

The (radial) asymptotic velocity is towards the center and *time independent*! It underlines the role of the log-sensing of the diffusio-phoretic transport in the long time evolution of the colloid distribution during the osmotic shock. The cut-off of the effect observed experimentally is related to the presence of buffer which gives a lower bound to the total solute concentration. We neglected the buffer so far and will continue to do so in the theoretical description. We will add its role and consequences as a refinement of the model and we will discuss it later in this part.

[17] A full resolution of the 1D case with the determination of the a_n coefficient is presented in Appendix D.

Fokker-Planck equation for the colloid evolution

Now, we go back to the colloid evolution. As a first approximation, one may use the above form for the diffusio-phoretic drift. This is strictly valid for sufficiently long times ($t > K_1^{-1} \sim$30 s), but in the present problem there is a time-scale separation between the solute dynamics and the colloid dynamics (evolution over ∼15 min), so that this is a reliable approximation.
One may then write the equation for the colloid density ρ as

$$\partial_t \rho = \nabla \cdot \left[D_{DP} \nabla \log J_0 \left[\alpha_1 \frac{r}{R} \right] \times \rho \right] + D_c \nabla^2 \rho \qquad (2.17)$$

Stationary distribution
Following the argument given in the osmotic trapping by rectified oscillations, the steady distribution is given by:

$$\langle J \rangle = -D_c \nabla_r \bar{\rho} + V_{DP} \bar{\rho} \simeq 0$$

leading to the steady colloid distribution:

$$\bar{\rho}(r) \sim \left(J_0[r. \frac{\alpha_1}{R}] \right)^{\beta} \qquad (2.18)$$

with $\beta = D_{DP}/D_C \sim 145$. We thus obtain a trap width $\Gamma \sim 32\,\mu$m with Γ defined as the half width at $1/e$. This prediction is in reasonable agreement with experimental measurements $\Gamma_{exp} \sim 75 \pm 5\,\mu$m. We come back on this difference below.

Time dependent evolution of the colloid distribution $\rho(r,t)$

For small distances r to the center, one may furthermore approximate the diffusio-phoretic drift term of Eq-2.17 using

$$\nabla \log J_0 \left[\alpha_1 \frac{r}{R}\right] \simeq \frac{1}{2}\frac{\alpha_1^2}{R^2} \times \mathbf{r} \tag{2.19}$$

which gives a Fokker-Planck equation for ρ:

$$\partial_t \rho = \nabla \cdot \left[\frac{D_{DP}}{2}\frac{\alpha_1^2}{R^2} \times \mathbf{r}\rho\right] + D_c \nabla^2 \rho \tag{2.20}$$

This can be rewritten as

$$\partial_t \rho = \frac{1}{\tau}\nabla \cdot \left[\mathbf{r}\rho + \sigma^2 \nabla \rho\right] \tag{2.21}$$

with $\tau^{-1} = \frac{1}{2} D_{DP} \frac{\alpha_1^2}{R^2}$ and $\sigma^2 = \frac{2}{\alpha_1^2}\frac{D_c}{D_{DP}} \times R^2$. Note that $\tau = \sigma^2/D_c$.
This is the so-called *Orstein-Uhlenbeck process* [50].
The stationary solution is a Gaussian with width σ^2:

$$\rho(r,t) \propto \exp\left(-\frac{r^2}{2\sigma^2}\right) \tag{2.22}$$

which is in full agreement with Eq-2.18, as J_0^β can be approximated by a Gaussian with very good accuracy.
The analytical solution of this Orstein-Uhlenbeck equation can be expressed analytically [50].
First the propagator – solution of Eq- 2.21 with a point-like initial condition, $P(\mathbf{r}, t=0|\mathbf{r}') = \delta(\mathbf{r}-\mathbf{r}')$ – takes the form in a d

dimension space:

$$P(\mathbf{r},t|\mathbf{r}') = \frac{1}{\left(2\pi\sigma^2(1-\exp(-2\gamma t))\right)^{d/2}} \times \exp\left[-\frac{1}{2\sigma^2}\frac{\left(\mathbf{r}-e^{-\gamma t}\mathbf{r}'\right)^2}{1-e^{-2\gamma t}}\right] \quad (2.23)$$

Then the complete solution for the colloid density is given by "propagating" the initial colloid distribution:

$$\rho(\mathbf{r},t) = \int d\mathbf{r}'\,\rho_0(\mathbf{r}') \times\ P(\mathbf{r},t|\mathbf{r}') \quad (2.24)$$

with $\rho_0(\mathbf{r})$ the initial condition for the colloid density. In line with the experimental conditions, we assume a uniform initial density over a circle of radius $\mathcal{R}$ (not to be confused with R the radius of the salt boundary condition), so that

$$\rho(\mathbf{r},t) = \rho_0 \int_{|\mathbf{r}'|<\mathcal{R}} d\mathbf{r}'\ P(\mathbf{r},t|\mathbf{r}') \quad (2.25)$$

This integral can be calculated after some straightforward – but cumbersome – calculations. In the present 2D geometry, this gives with I_0 the zero order Bessel function:

$$\rho(r,t) = \rho_0\, A(t)\, e^{-r^2} \int_0^R 2\pi r' dr' I_0(2\alpha\beta r r') e^{-\alpha\beta^2 r'} \quad (2.26)$$

where we introduced: $A(t) = \left[2\pi\sigma^2(1-e^{-2\gamma t})\right]^{-1}$ with $\gamma = \tau^{-1}$ and

$\alpha(t) = \left[2\sigma^2(1-e^{-2\gamma t})\right]^{-1}$, $\beta(t) = e^{-\gamma t}$.

Additional remark
We could predict in a more simple way the exponential decay of time evolution of the rms width of the colloid distribution. Let us first define the rms width of the colloid distribution as $\langle r^2\rangle = 1/d \int d\mathbf{r} r^2 \rho(r,t)$ with d with the space dimension. Integrating the Fokker-Plank equation for the colloid density $\rho(\mathbf{r},t)$ (see Eq-2.17) with part integrations, one obtains the temporal ordinary differential equation for $\langle r^2\rangle$:

$$\partial_t \langle r^2\rangle(t) = -\frac{2}{\tau}\left(\langle r^2\rangle - d\sigma^2\right) \qquad \boxed{2.27}$$

The rms width of the colloid distribution is linearly related to the radius $\Gamma(t)$ (radius at $1/e$ defined in experiments and previous theoretical description) by: $R^2(t) = \alpha \times \langle r^2\rangle$. This thus predics an exponential decay of the squared radius of the distribution over a time scale fixed by $\tau/2$ in qualitative agreement with the analytical solution of this Orstein-Uhlenbeck equation.

Comparison with the experiments

Let us arbitrarily define the radius Γ of the distribution as $\rho(r=\Gamma(t),t) = \rho(r=0,t)/e$. We extract numerically this radius from Eq- 2.26. The same procedure is applied in the experiment. We superimpose on Fig. 2.12 the experimental measurements of $\Gamma(t)$ and compare them with the theoretical predictions derived above. The red dashed curve is the prediction using the experimental parameters: $D_c = 2\,\mu\mathrm{m}^2/\mathrm{s}$, $D_{DP} = 290\,\mu\mathrm{m}^2/\mathrm{s}$

(measured independently in diffusio-phoretic migration, experiments, see section-2.2), $R = 450\,\mu$m and $\mathcal{R} = 325\,\mu$m. Using the above expressions, one obtains $\sigma = 22.3\,\mu$m and an exponential decay over a time $\tau = \sigma^2/D_c \sim 250s$. These are in qualitative and semi-quantitative agreement with the experiments. A much better agreement can be obtained by relaxing the constraint on the relaxation time and using $\tau = 290\,$s as a "best fit" while keeping the value of σ to the predicted one: (see green dashed line on Fig. 2.26)

The very good agreement between the theoretical predictions and the experiments shows that this scenario really captures the physics at work. We now discuss the discrepancy at long time between theory and experiments as consequences of the buffer presence.

Role of the buffer

Without buffer, one would expect a time-independent diffusio-phoretic velocity towards the center of the cell and an always decreasing function $\Gamma(t)$. But we observe a slight increase of the radius Γ of the distribution at long time, for $t > 500\,\text{s} \approx 2\tau$. Such an effect is actually expected due to the finite buffer concentration which acts as a *cut-off* for the osmotic-shock process. Up to now we neglected the presence of the buffer by imposing boundary conditions $c = 0$ for $t > 0$. This is a reasonable assumption at small times as $c = c_0 = 100\,\text{mM} \gg c_b = 1\,\text{mM}$, c_b being the buffer concentration. But it becomes inappropriate for small solute concentrations. The buffer concentration

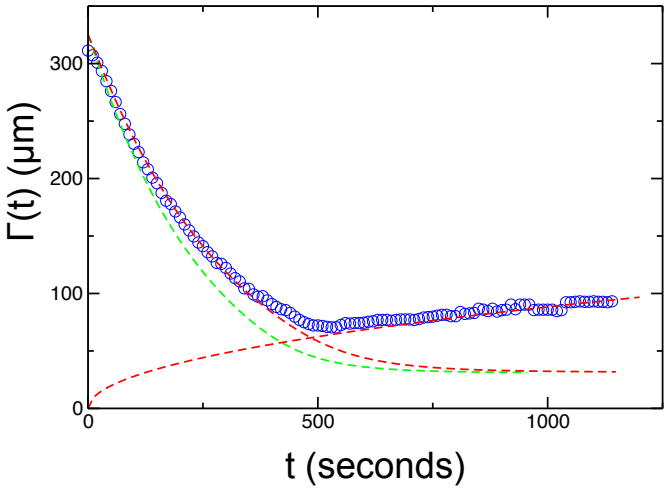

Figure 2.12: **Radius of the colloid distribution versus time.** Comparison to theoretical predictions. Radius $\Gamma(t)$ measured in experiments from the colloid density profiles (blue symbols). The red dashed curve is the prediction using the experimental parameters $D_c = 2\,\mu\text{m}^2/\text{s}$, $D_{DP} = 290\,\mu\text{m}^2/\text{s}$ (measured independently by diffusio-phoretic migration experiments), $R = 450\,\mu\text{m}$, $\mathcal{R} = 325\,\mu\text{m}$, yielding $\sigma = 22.3\,\mu\text{m}$ and $\tau = 250\,\text{s}$. The green dashed is obtained with the same value of $\sigma = 22.3\,\mu\text{m}$ and $\tau = 290\,\text{s}$, chosen to obtain a 'best fit' to the experimental data. The dashed black line is the purely diffusive motion: $\Gamma(t) = \alpha\sqrt{D_c t}$ with $\alpha = 1.9$ to fit the data.

then matters and one needs to use the total expression for the diffusio-phoretic velocity: $V_{DP} = D_{DP}\nabla c/(c + c_b)$. For long times, such that $c(r,t) < c_b$, $\nabla c/(c + c_b) \to 0$ and so does the diffusio-phoretic velocity.
Typically, as $a_1 \approx c_0$, this occurs for a time $T \approx \frac{1}{\alpha_1^2}\frac{R^2}{D_s} \times \log(c_0/c_b)$. For experiments in microfluidic cells $R = 450\,\mu$m with LiCl salt, $D_s \sim 1350\,\mu\text{m}^2/\text{s}$, one finds $T \sim 2\,$mins. In this long time limit, $t > T$ (with T the cut-off time introduced above), the size of the colloid distribution will re-increase diffusively, as $R^2 \sim D_c t$. We have plotted this prediction on the figure 2.26 (green dashed line, $R(t) = 1.9\sqrt{D_c t}$). This is in very good agreement with the tendency observed experimentally (see Fig. 2.12). The expression of the cutoff time can be rewritten $T \approx \tau \times D_{DP}/D_s \times \log(c_0/c_s) \sim \tau \sim 250\,$s. This is in rough agreement with the experimental observation of a cut-off time of $T_{exp} \approx 500\,$s.

We have verified this cut-off behavior by performing numerical analysis to explore more quantitatively the role of the buffer. We have simulated the time-dependent diffusion equation in a 2D circular chamber *with and without* buffer, the parameters being set to experimental values (notably $c_b = c_0/100$ when the buffer is present). We then extract the average quantity:

$$\frac{1}{2R}\langle \nabla c/(c + c_b)\rangle = \frac{1}{2R}\int_{cell} \frac{\nabla c(r,t)}{c(r,t) + c_b} = \int_{cell} \frac{V_{DP}(r,t)D_{DP}}{2R}$$

It is a measurement of the mean diffusio-phoretic velocity in the microfluidic chamber. The numerical results are represented on

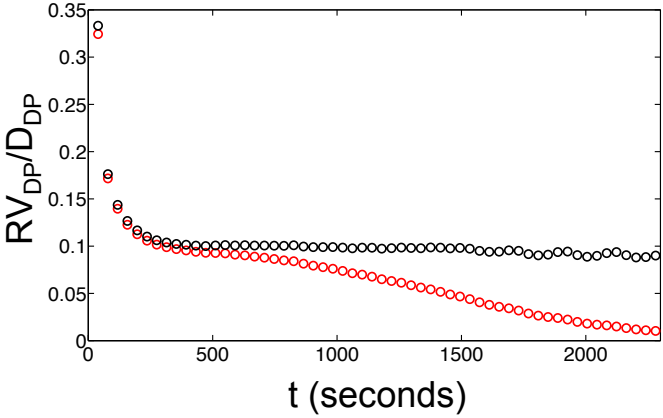

Figure 2.13: **Cut-off of the osmotic shock by the buffer.** The diffusion equation of the salt is solved *numerically* with Matlab ®in a 2D circular microfluidic cell with the parameters set to the experimental values)and the average dimensionless diffusio-phoretic velocity calculated with $\frac{1}{2R}\langle \nabla c/(c+c_b)\rangle$ (see text). Symbols stand for the diffusio-phoretic velocity averaged in the whole cell with buffer of concentration $c_b = \frac{c_0}{100}$ (red symbols) or without buffer (black symbols). The cut-off by the buffer appears clearly for times $t > 500s = 2\tau$ in agreement with the experiments.

figure 2.13 and indeed show the cut-off role of the buffer on the diffusio-phoretic effects. We can estimate the cut-off from these simulations to $T_{num} \approx 500\,\mathrm{s}$ which is in good agreement with experimental observations.

2.4.4 To sum up on localization by osmotic shock

Altogether the temporal dynamics of the localization induced by osmotic shock is a two steps process:

1. $R(t)$ follows an exponential decay for $t < T$ related to the sensibility to vanishing concentrations of electrolyte solution of diffusio-phoresis

2. $R(t)$ is in a diffusive regime for $t > T$. The buffer acts as a cut-off for the diffusio-phoretic migration and the thermal motion of the particles dominates the dynamics in this regime

And the time $T \approx \tau \times D_{DP}/D_s \times \log(c_0/c_s) \sim \tau$ is given by the cut-off role of the buffer on the osmotic shock.

2.5 Further physical perspectives

Up to now, we have mainly discussed the diffusio-phoretic behavior of latex colloids in a solute gradient and demonstrated various use of the phenomenon as particles carriers or patterning. We now open the discussion to perspectives on different

physical systems or applications. Any of the proposed experiments would gain to be performed in a non-convective environment and controlled solute gradient as provided by our setup. This underlines the versatility of our gel microfluidic device in the thorough exploration of diffusio-phoresis.

2.5.1 Preliminary results: crystallisation and self-healing by osmotic compression

We end this section by presenting physical perspectives and preliminary experiments on colloidal crystal formation under osmotic compression. Such crystals present very interesting properties of "self healing" which we attribute to the interfacial diffusio-phoretic flow at the colloidal surface.

Experiments

A dilute solution of latex colloids of diameter 1 μm is enclosed in the microfluidic chamber of an hydrogel device as described previously. A LiCl gradient is imposed in the chamber ($c_1 = 100\,\mathrm{mM}$, $c_2 = 0$ for LiCl) and colloids migrate by diffusio-phoresis towards the chamber wall with high concentration of salt. At the wall, particles pack and a colloidal crystal grows as the diffusio-phoretic compression overhauls thermal noise. The colloidal crystal is not perfect and presents various symmetries *e.g* square or hexagonal lattices as can be seen in figure. 2.14-a. One can attribute the geometry defects to the non-flatness of the wall due to the "hydrogel technology" used here. Colloidal crystal thus forms with different orientations leading to geomet-

rical frustration.
Nevertheless the crystals present very few holes and an interesting ability to "self-healing": it grows *(i)* row after row from the wall and *(ii)* when a colloid reaches the crystal, it displaces until "spontaneously" filling a void in a row (see Fig. 2.14-b).

First interpretation of self-healing

The ability of the colloidal crystal to self-organize and minimize the number of holes is related to the interfacial origin of the compression force. Colloids are pushed to the wall by diffusiophoresis. A colloid 1 is pinned at the wall but still generates a diffusio-phoretic interfacial flow at the surface. This results in a pumping of the fluid (see Fig. 2.14-c). A colloid 2 reaching the crystal explores thermally the vicinity of the crystal until it is dragged by the pumping flow created by 1 acting as an attractive pseudo-force. Colloid 2 displaces until it fills the void next to Colloid 1. This scenario of a row "self-healing" explains the dynamics observed experimentally (see Fig. 2.14-b). This hydrodynamic attraction arises from the slip flow on the particle surface, common to all phoretic phenomena, and has thus been observed for thermo-phoresis [51, 52] or electrophoresis [53]. Further study of this phenomenon and its application for osmotic annealing remains to be done and might be of great interest for colloidal crystal application as photonics.

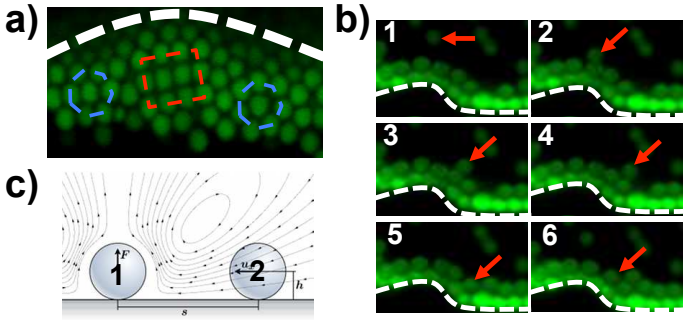

Figure 2.14: *(a)* Colloidal crystallisation under osmotic compression. 1 μm latex colloids migrate by diffusio-phoresis and form a crystal against the chamber wall (dashed white line). This crystal is imperfect and present various lattices: square (red) or hexagonal (blue) but no voids. Fluorescence observations of only the first layer of colloid performed by confocal microscopy. *(b)* Self-healing of the diffusio-phoretic crystal. (1) A colloid (pointed by a red arrow) migrates to the wall (dashed white line) by diffusio-phoresis. $(2-4)$ It explores the crystal surface thanks to thermal motion until it reaches a "defect", *i.e.* a hole in a crystal row. (5) It fills the void and erases the structural defect (6). A new row of the crystal then grows. Fluorescence episcopic observations with $60\times$ of high numerical aperture (N.A 1.2). *(c)* The slip velocity on colloidal particle 1 pinned ad the wall by diffusio-phoresis generates a flow (black lines) leading to an attractive pseudo force for colloid 2 and thus to the healing-process observed. This mechanism is common to any phoretic phenomenon. Reprint from [51] for colloidal attraction under thermo-phoretic flow.

2.5.2 Further perspectives

Diffusio-phoresis of "complex" colloids

Until now both experimental and theoretical work have considered only simple colloids. It would be interesting to test diffusio-phoresis with more complex systems:

- **Anisotropic colloids.** Recent progress in colloidal engineering allowed to synthesize particles of various shapes: ellipsoids, rods or even fancier non uniform materials like Janus colloids. Diffusio-phoresis on anisotropic colloids, anisotropic form or non uniform ζ-potential for Janus particles, is still to be explored, notably the relative position of the anisotropy axis with the migration direction.

- **Macromolecules.** As exposed in this chapter, diffusio-phoresis is observed with biological macromolecules as DNA. Nevertheless the dynamics of the migration more complex than for latex colloids requires further theoretical description of diffusio-phoresis of macromolecules.

Diffusio-phoresis on superhydrophobic surfaces

We mentioned in the first chapter the predictions for the giant amplification of the diffusio-phoretic transport induced by slippage. Experimental investigations of this aspect are necessary, *e.g.* using the large effective slip length obtained with superhydrophobic surfaces . It can be practically realized with a microfluidic chanel composed of one superhydrophobic wall and

three non-slipping walls. A concentration gradient is built up either using the simple Ψ geometry proposed in [17] or with an hydrogel device as described along this chapter. The diffusio-osmotic flow can be measured by PIV to test the massive amplification of diffusio-osmotic transport. If so, such system would present interesting applications in efficient mixing or pumping depending on the geometry of the superhydrophobic surface [27]. An alternative perspective would be the study of self-propelled diffusio-phoretic microswimmers in the vicinity of liquid-air interfaces, *e.g.*the Cassie state of the SH surface. At the interface, the particle generates autonomously a concentration gradient, and thus propels by a real *Marangoni-effect* leading to propulslons velocities of order cm/s. This scenario also remains to be tested experimentally.

Extreme sensitivity and vanishing concentrations

We discussed in section-2.4 some consequences of the logarithmic sensing of the diffusio-phoretic velocity and underlined the role played by the buffer as the cut-off concentration for the phenomenon. If we now suppose the absence of buffer in utrapure water the cut-off concentration should be given by water auto-protolysis with $c_a = 10^{-7}\,\mathrm{M}$. A salt concentration of $c_s = c_a$ represents 10^{-2} salt molecules in $1\,\mu\mathrm{m}^3$, the typical volume of a colloid. In this utra-dilute regime, the validity of the continuum description of diffusio-phoresis interfacial transport becomes questionable.

Impact of diffusio-phoresis on evaporation

A droplet containing initially a uniform concentration of solute will develop concentration gradients during the evaporation process [54]. The concentration gradient should lead to an additional diffusio-phoretic transport of colloidal particles over the capillary flow causing ring stains from dried liquid drops [55]. The question is whether this effect is large enough to be visible out of the fast recirculating flows, and *e.g.* presenting solute and notably salt specificity effects. The additional diffusio-phoretic contribution would therefore be of interest in many industrial processes suchas coating, printing or washing...

2.6 Biological perspectives: an iconoclast questioning

I don't think that it will make enough impact on the biologists and there is no reason to publish it otherwise

A PNAS editor (2009)

Nota Bene. In this section we underline analogies between diffusio-phoresis and some purely biological mechanisms: chemotaxis or localization. In this regard we will raise iconoclast questioning on the possible role of the physical phenomenon in the complex machinery of life. We will elude to give conclusive answers on the role of this physical mechanism in a most complicated biological problem and will prefer pro and cons arguments. The aim of this section is rather to open doors and ultimately motivate further experimental work to test the validity of the proposed scenario, *e.g.* localization, in living systems.

2.6.1 A toy model for chemotaxis?

As shown in previous sections, *diffusio-phoresis* is a *physical* mechanism for –literally– a chemotactic-like motion of inert particles: motion under the gradient of chemical solutes. On purely semantic basis, diffusio-phoresis can then be denoted as "physical chemotaxis". This echoes the *biological* phenomenon of *chemotaxis* by which biological systems –cells, bacteria, or

multicellular organisms- direct their motion according to chemicals gradients [56–59]. It is a complex phenomenon which relies on the orchestration of protein networks to achieve directed motion but of prime importance for living systems life as they need to be attracted by food and repelled from poison.
Of course diffusio-phoresis does not involve the complex machinery involved on biological chemotaxis but the analogy raises interrogations:

Q1: Do some biological systems make use of diffusio-phoresis as a supplementary component on their chemotactic motion?
We present some puzzling analogies in the context of bacterial chemotaxis, notably *E. Coli* chemotaxis. An interesting fact is that the chemotaxis of bacteria could present *salt specificity* effects. Qi *et. al* reported that (i) chloride salts of various alkali metals behave as attractants for wild type *E.Coli* and measured (ii) salt specificity with "attractiveness" following Hofmeister series LiCl>NaCl>KCl (see Fig. 2.15-a). Both results are conversely observed and expected in the context of diffusio-phoresis and might be some hints of a possible additional role of the physical phenomenon in the biological migration.

Q2: Can diffusio-phoresis be used as a biomimetic phenomenon?
It is generally assumed in the literature that the chemotactic velocity follows a Keller-Segel model [60] thus proportional to the concentration gradient $V_{chemo} = \kappa \nabla c$. The chemotactic coefficient κ *a priori* depends on the concentration but is

usually defined as a constant to successfully describe experimental results [61–64]. However a careful study by Kalinin *et al.*, in a well controlled concentration gradient has recently unveiled a *logarithmic sensing* of the chemotactic response of *E. Coli* $V_{chemo} \propto \nabla c/c$ [65]. While its origin is different from the *logarithmic sensing* of diffusio-phoresis[18], the non-linearity should induce a trapping of the bacteria under chemo-attractant concentration oscillations rectification (see section 2.3). The strength of the trap would be given by the balance between the "attractiveness" of the chemo-attractant and the effective diffusion constant D_{eff} of the bacteria and thus gives a versatile tool to change *on the fly* the density of bacteria in a system. Finally beyond these analogies it is still difficult to confirm or infirm the role played by diffusio-phoresis in the chemotaxis of bacteria or cells.

2.6.2 Diffusio-phoresis and spatial cell biology

In this chapter we have demonstrated robust *localization* mechanisms of synthetic or biological–DNA– colloids by diffusio-phoresis. Alternatively, *spatial cell biology*, *i.e.* the spatial patterning inside cells or at the multi-cellular level, and spatial organization appears crucial for development and physical integrity. As part of cancer metastasis, cancer cells develop the ability to escape their usual physical niche and set up residence elsewhere

[18] We briefly remind that the *logarithmic sensing* of diffusio-phoresis is given by an electrostatic interaction between an electrolyte and the charged surface of a particle and the concentration dependance of the Debye length: $\lambda_D^2 \propto 1/c$ (see section 1.2.2).

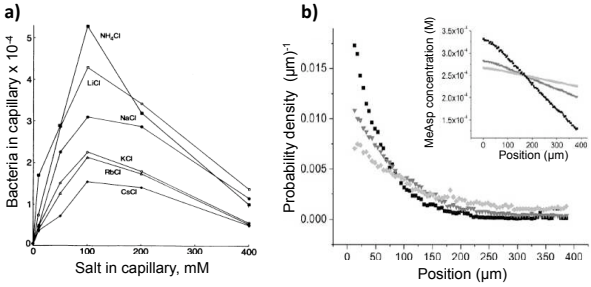

Figure 2.15: **Analogies between the biological chemotaxis and the diffusio-phoresis.** *(a)* The chemotaxis migration of *E. Coli* bacteria towards monovalent-cation chloride salts ($CsCl, RbCl, KCl, NaCl, LiCl, NH_4Cl$). Salt gradients generated with a filled capillary. These salts are (i) attractant and (ii) the chemotactic behavior presents salt specificity. The migration follows the series LiCl>NaCl>KCl. (i) and (ii) are both expected from theory and observed for diffusio-phoresis. *Reprint from [66].(b)* Logarithmic sensing of chemotactic migration of *E. Coli*. The chemotactic migration is balanced by the random swimming of the bacteria leading to a dynamic equilibrium with bacteria population following $n(x) = n_0 \exp(-x/\delta)$, with x the position in the channel, zero being on the wall. The figure represents *E. Coli* density distribution as a function of the position in the channel. The density distribution presents an exponential decay, with a length scale decay which depends on the chemoattractant gradient (inset). Kalinin *et al.* showed from these measurements that *E.Coli* present a logarithmic sensing $V_{chemo} \propto \nabla c/c$. Reprint from [65].

within the body. Position within the body is coded by specific gene expressions programs and affects cell's differenciation and functional characteristics [67]. For successfull cytokinesis, *i.e.* the last step of the cell cycle with physical separation into two daughter cells, it is crucial to place the cleavage furrow in the right place between the separated chromosones, at the cell equator, task performed by actin cytoskeleton [68]. The transcription to proteins is regulated in animal cells by the intracellular localization of RNAs [69]. And bacteria control their cellular anatomy through the intracellular location of individual proteins during growth and division in response to external *stimuli* [70].

These examples demonstrate the key role played by spatial organization in biological systems and this domain has been very active over the recent years. In this context, concentration gradients of species, namely *morphogens*, are of prime importance in the toolbox of living systems and provide readily sophisticated functionalities associated with spatial signaling, localization and pattern formation [71]. In order to figure out the positional information given by a concentration gradient, we consider a 1D cell for the sake of simplicity. A biological process, not defined here, imposes a smooth gradient of a morphogen A in the cell, with high concentration on one pole and low concentration of A on the other pole. We consider a gene B which is expressed in B^* presence of A, A is the activator of the B gene. The smooth gradient of A is translated, by threshold effect related to the activation kinetics, into a sharp boundary of B^* leading to varying expressions of a gene in the cell, *i.e.* spatial organization in a cell ! Structural patterns thus have their origins in

spatial patterns of morphogen molecules both at intra or supra-cellular level.

At the supra-cell level.
The primary determinant of patterning along the anterior-posterior axis in the fly *Drosophilia* is the gradient of the Bicoid (Bcd) morphogen, established by maternal displacement of Bcd RNA at the anterior end of the embryo. Bcd regulates genes expressions which generates a reproducible spatial patterns [72]. Similar mechanism with BMP morphogens are also reported in the dorsal region of *Drosophilia* embryos [73].

At the intra-cellular cell level.
In the bacterium *E. Coli*, the Min[19] proteins oscillate between the cell poles to select the cell center as division site by reaction-diffusion type mechanism. Furthermore, the same proteins spontaneously form spatial planar surface waves on a flat membrane *in vitro* with only limited number of proteins (MinD and MinE), ATP and a membrane. It underlines how complex behavior can emerge from strongly non-linear reaction-diffusion dynamics despite a small number of components at use [74]. Alternatively, the cell polarity protein Pom1 localized at the cell end regulates a signaling network that contributes to the control of mitotic entry at the beginning of the cell division [75]. Morphogen gradients are at the core of the location of the cell division plane for bacteria [70, 76, 77]. Mathematically the emergence of spa-

[19] Min is a family of proteins. Here the system consists of proteins MinC, MinD and MinE.

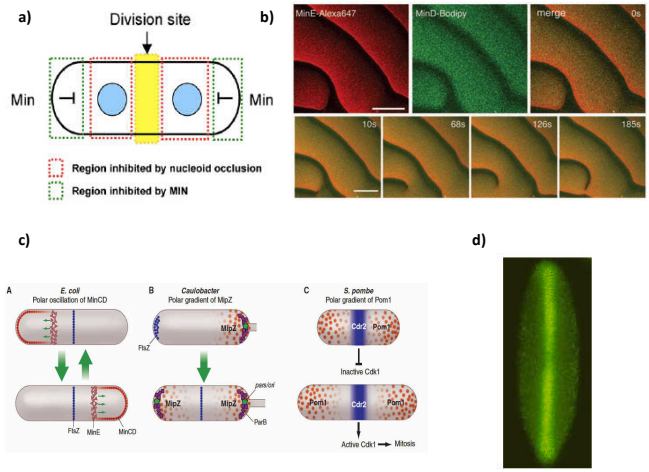

Figure 2.16: **Spatial Cell Biology and biological counterparts of the ingredients of the diffusiophoretic trapping.** *(a)* **Gradient of a signaling protein (Min)** and selection of the center of the bacteria as the division site by two overlapping inhibitory mechanisms. The Min proteins prevent presence of Z-ring at the poles and the nucleoid occlusion machinery prevents its presence in the vicinity of the nucleoids. That leads to a division site in the middle of the cell. Reprint from [77]. *(b)* **Min-protein surface waves in vitro.** Confocal images of self-organized protein waves on a supported lipid membrane. It does show static oscillations of biological signaling proteins. Scale bar is 50 μm. Reprint from [74]. *(c)* **Polar ocillations of signaling proteins (Min)** determining the cell topology through repression and inhibition mechanism. MinCD repressor from pole to pole restricts the site of division ring assembly to the center of the cell. Reprint from [70]. *(d)* **Localization of the BMP protein during the morphogenesis** of a *Drosophila* embryo (2h after egg lay). A peak is visible in the dorsal region (Reprint from [73]). The pattern presents a puzzling resemblance with the cat-eye shape obtained with an *abiotic* scenario of rectified diffusio-phoresis trapping (see Fig. 2.9).

tial patterns relies in a strong non-linearity in the evolution equation of the system and its components. In the context of spatial cell biology, various feedback mechanisms have been proposed, all supported by reaction-diffusion equation in a Turing like approach [78]. The biological system presents sources and sinks of various signaling protein [77, 79] leading to a gradient (see Fig. 2.16-a). Other species are inhibited or expressed by the presence of signaling proteins leading to the emergence of patterns. Thanks to the non-linearity of the chemical reaction kinetics and the coupling of a large number of these complex equations involving many intermediate chemicals, various patterns can be achieved and a good agreement between experimental and numerical predictions are achieved [73, 80].
This makes diffusion-reaction approach the "standard" description of self organization in biological systems. Nevertheless the precise positioning mechanism remains elusive and still raises many questions, concerning the building-up of the gradients themselves [81] and the process by which these gradients are read by the organizing entities. Also the accuracy and robustness of the positioning mechanisms especially in the noisy environment of biological systems remain puzzling [72]. Finally spatial cell biology strongly relates patterning mechanisms with concentration gradient of species, the morphogens. In this context, we address the question of the potential role of the diffusiophoretic trapping mechanism we unveiled –trapping by rectified oscillations and osmotic shock– in the spatial organization of biological systems. Again this question is very iconoclastic but deserves to be raised.

Q3: Could the diffusio-phoretic patterning mechanisms play any role in the spatial organization of biological systems?

This questioning is mainly speculative and we can not make clear statement on the role played by diffusio-phoresis in spatial cell biology. But some characteristics of the physical phenomenon further support its potential relevance in biological environment. As main point, diffusio-phoresis is sensitive to vanishing concentration gradients, quite compatible with biological morphogens concentrations, typically μM. Moreover, as a side remark, the spatial extension of the diffusio-phoretic trapping is proportionnal to the length scale of the gradient (see equation 2.8). Patterning can thus be achieved at the scale of a single cell bacterium or during morphogenesis on much larger scale.
Actually they are cons and pro for the possible role of diffusio-phoresis in these systems:

Cons:

Spatial cell biology is strongly specific, *e.g.* only very specific genes are spatially expressed in a morphogen gradient, and proteins react only to specific markers, by key-lock interaction. By contrast diffusio-phoresis is very generic and the phenomenon takes place each time the particle surface interacts with the solute through the interaction potential U. But this argument can be partially answered if the potential U is itself very *specific*, *i.e.* requires specific interaction between the morphogen and the biological particle.

Pros:

2.6. BIOLOGICAL PERSPECTIVES: AN ICONOCLAST QUESTIONING

1. Biological systems present concentration gradients of morphogens in which biological colloids –proteins– should migrate by diffusio-phoresis.

2. Temporal oscillations of concentration occur in many experimental systems: Min proteins concentration oscillates from pole to pole in cell which is crucial to determine the cell topology and define the equator as the division site. (see Fig. 2.16-c), [74]. Moreover, pH as well as Ca^{2+} gradients oscillations are observed in pollen tubes, even if the mechanisms underlying the oscillations as well as their physiological role remain unknown [82].

Several biological systems present all the necessary ingredients for a diffusio-phoretic migration and possibly the localization of species induced by concentration oscillations. Nonetheless answering the question deserves a complete and specific study which has not been done up to now.
Finally, given the robustness of diffusio-phoresis mechanism, it is interesting to go reverse and ask the following -open- question as a conclusion of this section on the role of diffusio-phoresis in the context of spatial cell biology:

All the ingredients being present, why would diffusio-phoresis not play any role in biological systems?

The big picture

In this chapter, I studied diffusio-phoresis with colloids or biological macromolecules in a controlled concentration gradient which required the development of hydrogel microfluidics. I characterized the diffusio-phoretic migration of the particles and measured –in agreement with theoretical predictions– a diffusio-phoretic velocity in electrolyte gradients:

$$V_{DP} \propto \nabla \log c$$

I demonstrated experimentally that patterning of particles arise from the *logarithmic sensing*. The non-linearity of the expression leads to *(i)* trapping of particles by rectification of oscillations while the high sensibility to vanishing concentrations of the log-sensing is harnessed to obtain *(ii)* particles segregation by osmotic shock. The observations are rationalized by theoretical and numerical predictions. Finally, I discussed further perspectives of diffusio-phoresis and arose an iconoclast questioning of the relevance of the phenomenon in biology.

2.7 Appendices

Appendix A: Soft Lithography of Microfluidic Masks

The design and realisation of the silicon mold are based on standard soft lithography techniques. I will consequently briefly report the steps and the interested reader can refer to [83, 84] to learn more on the *art of microfabrication*.
The desired features are designed on Adobe Illustrator ®(see Fig. 2.2) and printed at 3600 dpi on transparent films (APO Lyon). The microfabrication is performed at the INL (Institute of Nanotechnology Lyon) clean room. The positive relief features on the silicon mask are obtained with a SU8 permanent epoxy negative photoresist (SU8-2100, Microchem). The experimental parameter are adaptated from the standard processing guideline to obtain channels of $\sim 120\,\mu$m thickness in our facilities [85]. The following steps of lithography with their parameters are the following.

1. **Dehydration and Silicon Etching.** A 4 inch diameter silicon wafer is first dehydrated on a hotplate at $200°C$ for $30'$ and cleaned with a plasma etching (RIE 51 MRC) at 200 mTorr with 0_2 during $2'30"$. The oxygen plasma is used to clean the silicon surface by reacting with the organic residues. The resulting volatile products are swept away by the pumping action of the vacuum.

2. **Spin-Coating.** The silicon wafer is spin-coated to obtain an approximately 120 μm thick layer of SU8-2100. The photoresist is first spinned at 500 rpm during 10 s under an acceleration of 100 rpm/s and then spinned at 2000 rpm during 30 s under an acceleration of 300 rpm/s.

3. **Soft Bake.** The wafer covered by a thin layer of SU8 is baked during 5′ on a hotplate at 65°C and then transferred to another hotplate at 95°C for a 27' bake. Finally the hotplate is switched off and the wafer slowly cools down with the plate until room temperature. During these steps the wafer is partially covered by a glass petri dish to smooth the layer and fill small defects.

4. **Exposure.** The pattern designed on the transparent film is transferred to the resin layer thanks to a mask aligner (SET MA 701, Suss) by exposing the wafer to UV light at 255 mJ.cm^{-2} (Hg lamp, $\lambda = 375$ nm).

5. **Post Exposure Bake.** This step takes place directly after expose. The exposed wafer is baked during 5' on a hotplate at 65°C and then transferred to another hotplate at 95°C for a 12' bake (at this step, the channels can be seen in the photoresist). The 95° Chotplate is switched off and the wafer slowly cools down with the hotplate until room temperature. It is crucial that the cooling is slow to avoid any cracks that could be induced by the mechanical stresses on exposed channels. Consequently the cooling step is performed covering the wafer with a glass petri

dish and preferentially on a hotplate with high thermal inertia. The cooling time is typically 2 h.

6. **Development.** The wafer is immersed in a development solution of PGMEA, vigorously agitated during $30'$ and then rinced with acetone and ethanol. If a thin film of photoresist remains on the wafer or between the channel, this development step is repeated until removal of all non-reticulated photoresist.

7. **Hard Bake.** We make a post hard-bake procedure on the mask to strengthen the mechanical properties of the SU8 and its adhesion on the silicon wafer given the thermal cycles imposed by the molding process. The mask is baked at $150°C$ during $1 - 2$ h and let cool on the switch off hotplate during a couple of hours.

Appendix B: Hydrogel Microfluidic Channels

Hydrogel preparation

Agarose hydrogel powder (Agarose ME, for biochemistry, Acros) is weighted with a precision balance and added to ultra-pure water (resistivity 18.2 MΩ, MilliQ) up to a $4.5-5\%$ w/v solution. This concentration is much higher that what biologist usually use for cell cultures and presents a good compromise for both a good mechanical response after settling of the gel (high enough Young modulus, good stiffness) and a low enough viscosity and aging time of the liquid phase essential for the molding step. The solution is vortexed 30 s and appears as a cloudy suspension. It is microwaved at maximum power in a 50 ml centrifugating tube during ~ 30 s until boiling. The solution is then shaked and microwaved again for five additionnal seconds. After these heating steps, the agarose powder is fully dissolved in water and the solution is homogeneous and transparent. Otherwise the solution is shaken and microwaved again. The liquid hydrogel is poured in a beaker on a hotplate at $80-90°$C and gently stirred at typically $100-200$ rpm. The magnetic stirrer is necessary to ensure a good thermal homogeneity in such a highly viscous solution but must not inject bubbles in the hydrogel. The beaker is covered to limit evaporation and settling at the surface until subsequent use and molding of hydrogel channels.

Agarose gel microchannels

The silicon master is placed on a hotplate at $75°C$. A volume of hot liquid agarose typically $1.5 - 2ml$ is poured onto the mold. The silicon wafer is then removed from the hotplate . Then a plexiglas manifod with a PDMS spacer (item 2 of figure 2.17) is pressed onto the mask. The PDMS spacer is a rectangular ring of thickness $\sim 700\,\mu$m higher than the depth of the channels ($\sim 120\,\mu$m) and defines the shape and the thickness of the gel stamp. The agarose gel covered by the manifold is cooled at room temperature during $40 - 60\,$s until settling of the hydrogel matrix. The agarose stamp is carefully peeled off the mask and stored in ultra-pure water at 6° C until subsequent use. The inlets and outlets of the channels are holed with a metal tip prior to any use of the agarose stamp.

Appendix C: Running an experiment, step by step

Assembly of the device, filling of the microfluidic chambers

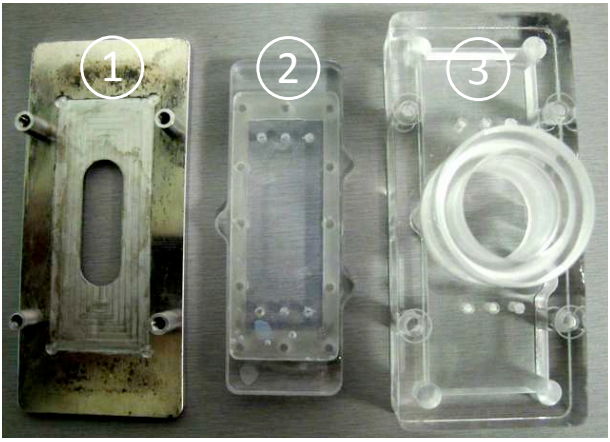

Figure 2.17: **Photograph of the microfluidic device developed for the gel system.** Item-1 is the metal framework. Item-2 is the plexiglas manifold to support the agarose stamp. Item-3 is the plexiglas cover of the system and ensures a proper sealing of the system.

The traditionnal sealing for PDMS soft lithography techniques is based on the covalent bonding of plasma activated glass coverslip and PDMS microchannels. Such a covalent seal-

ing cannot be achieved with hydrogel channels on a cover slip and we therefore developed a microfluidic device to seal agarose channels on coverslips thanks to the applied pressure. A clean coverslip of thickness $130 - 170\,\mu$m is placed on a aluminium framework (item-1, see Fig. 2.17)[20]. A recently holed agarose stamp is placed in the PDMS spacer frame of the plexiglas manifold (item-2, see Fig. 2.17) with the channels opposite to the plexiglas side. The plexiglas manifold is then inserted in the plexiglas cover (item-3, see Fig. 2.17) with the channels opposite to the plexiglas screw unscrewed (item 3') Particles are introduced in central chambers prior to the beginning of the experiment because microfluidic chambers do not have inlet or outlets. A large drop ($\sim 1 - 2$ml) of the colloidal solution is deposited on the clean glass slide. The item 3' is tightly bound to the metal framework (item 1) thanks to 4 screws driven in the 4 cylindric blocks of the metal frame. The colloidal drop is then pressed and one has to avoid capturing bubbles in the microfluidic chamber while bubbles in the side channels will be expelled by the syringe-pump. Finally, the plexiglas screw is snugged up until the applied necessary torque strongly increases due to the contact of the PDMS frame-microchannels on the coverslip. We let the system relax for a few minutes. The system is then tightly sealed without any leakage!

[20] Different designs of this framework were manufactured to adapt various objectives. Indeed some objectives -in particular with high numerical aperture- have a working distance much shorter than the average metal thickness necessary to maintain the planarity essential for an efficient sealing of the device. The metal frame was therefore machined to allow close approach of the objective to the cover-slip

Microfluidic chambers and temporally tunable gradients

The microfluidic device described in the previous section is ready to be used and can be completed by microfluidic inlets and outlets. The side-channels, used to impose the salt concentration boundary condition in the system, are filled with a double syringe pump (Kd Scientific) at a flow rate of $Q = 0.1$ml/min by means of 5 ml plastic syringes (Braun) [21]. Each syringe is filled up with the buffer solution or 100 mM salt (LiCl, NaCl or KCl) in buffer solution. Salt molecules diffuse freely in the patterned agarose gel while the solid hydrogel matrix prevents from convective flow between channels. Pressure differences in side channel and Darcy's permeability of hydrogel walls makes for negligible transverse flows as checked experimentally. Overall, side channels thus allows to set a concentration boundary condition, and the transverse gradient of salt in the central channel is linear and solution of the steady diffusion equation $\Delta c = 0$ (see Fig. 2.2-b). Temporal control is achieved with a manual microfludic switch (V140D, Upchurch) to reverse the concentration boundary conditions. Finally, we used two types of motile particles: polystyren-carboxylated fluorescent colloids (F8888 200 nm, Molecular Probes, 2% w/v), diluted 10 times in Tris

[21] Note that the use of glass syringes systematically induces uncontrolled dissymetry between the channels and top-bottom bias in the chamber. It is therefore necessary to use plastic syringes.The plastic syringes probably deform to compensate the differences of heigth (and therefore pressure applied at a given flux) between the 2 side channels which is precluded with the much rigid glass syringes.

buffer (1 mM Trizma, pH9), and fluorescent phage-λ DNA (48 kbp, Fermentas, Germany) at a concentration of 0.9nM in Tris-EDTA buffer (1 mM Tris, 0.1 mM EDTA, pH7.6).
All the observations were carried out with an inverted microscope (DMI4000B, Leica®) and a fluorescence camera (Orca, Hamamatsu®). The fluorescence signal is recorded with a 20x objective (ELWD, corrected for glass 0-2mm, N.A.0.4, 11506204, Leica) at 0.1 Hz.

Appendix D: 1D concentration profile during an osmotic shock

Calculations of the salt concentration profile are more transparent in 1D, with a system confined in the interval $|x| < \ell/2$.

$$c(x,t) = \sum_k a_k \, e^{-K_k t} \, \cos((2k+1)\frac{\pi}{\ell}x) \qquad (2.28)$$

with $K_n = D_s \left(\frac{n\pi}{\ell}\right)^2$.

The initial condition is such that $c(x, t = 0) = c_0$ for $|x| < \ell/2$. One uses the identity:

$$c(x,0) = \frac{4}{\pi}\sum_{k=0}^{\infty} \frac{1}{2k+1}(-1)^k \cos((2k+1)\frac{\pi}{\ell}x) \qquad (2.29)$$

This leads to

$$c(x,t) = \frac{4}{\pi}\sum_{k=0}^{\infty} \frac{1}{2k+1}(-1)^k e^{-K_k t} \cos((2k+1)\frac{\pi}{\ell}x) \qquad (2.30)$$

Une face double, un charmant Janus, et, au-dessus, la devise de la maison: "Ne vous y fiez pas"

A. Camus, La Chute

3

Janus microswimmers

The collective behavior of self-propelled entities has raised considerable interest over the recent years in the context of non-equilibrium statistical physics [86–91]. Assemblies of active elements are rather commonly encountered in "societies" of biological organisms and encompass systems as diverse -notably in scale- as swimming cells and bacteria colonies [92–99] , flocks of birds or sheeps and schools of fishes [87, 100]. All these entities move actively by consuming energy and their behavior is thus intrinsically out of equilibrium. Building a general framework describing their collective properties remains accordingly a challenging task and has led to a considerable amount of theoretical work along these lines [86–91, 101]. By contrast, much less work has been performed on the experimental side, and mainly on assemblies of living micro-organisms – which are naturally self-propelled – [92–96, 98, 99, 102–104] however at the expense of a lack of control and flexibility of the individual particles and

their interactions. There is therefore a need to develop new experiments based on *artificial* model systems, involving suspensions of microscopic active particles with controlled propulsion and interaction mechanisms? Several routes to design individual artificial microscopic swimmers have been explored in recent years [105–109], taking advantage of the recent progresses made to shape and design colloidal particles at microscales. However going from the individual to the many particles situation remains a challenging task and has not been achieved up to now with artificial motile particles.

Aim of this work

We aim at studying the properties of *active matter*, i.e. with active particles, and the additional degrees of freedom given by out-of-equilibrium phenomena over equilibrium paradigms. This out-of-equilibrium nature of the system leads to a rich variety of new phenomena: collective behaviors, pattern emergence, break-down of the second principle ... We address this problem using artificial diffusio-phoretic swimmers, namely *Janus* colloids. The idea is to generate a solute gradient on the particle itself which in turn leads to a motion *via* diffusio-phoresis. This is done by means of a non uniform chemical activity on the particle surface. Here we will follow a route proposed by proposed by Howse *et al.* [108]. And use the dismutation of hydrogen peroxyde H_2O_2 on platinum catalyst asymmetrically coated on the colloid. These particles convert the free energy into propulsion by diffusio-phoresis and provide synthetic "toy-models" in the study of the out-of-equilibrium properties of *self-propelled par-*

ticles (SPP). Moreover "chemical swimmers" interact through hydrodynamic fields but also *via* the *non-local* concentration-field gradients they generate by the chemical reaction [110] and could *a priori* present richer behaviors than simple SPP. The consequences of the chemical coupling with active systems have not been considered up to now in the literature and appears as a relevant path to study collective behaviors out-of-equilibrium.

Organization of the chapter

I will first present the basics of life at low Reynolds number. This general part will describe the specificity of the dynamics of microorganisms and micro-swimmers and review a few swimming strategies developed to overcome the time reversibility of Stokes equation. In particular I will briefly review the case of bio-mimetic synthetic swimmers. I will then introduce "phoretic" swimmers driven by interfacial motor and notably chemical Janus colloids, the *core* of the present work. I will report the first results obtained by Howse *et al.* with these systems in the *"infinitely dilute"*.
To go further and study more concentrated regimes and ultimately collective effects, I developed improvements of the Janus synthesis. In a first step, I will characterize the high speed dynamics of *individual* swimmers and show that it is a persistent random walk. Then, in the same spirit as the equilibrium statistical physics, I will turn to the response of a dilute assembly of active colloids under force field through a sedimentation experiment. I will show that in the *"semi-dilute"* regime, the system is properly described as an *equilibrium ideal gas of hot colloids* at

temperature T_{eff}, related to the energy injection by activity in the system. This experiment is to my knowledge the only experimental measurement of effective temperature of active systems. *Note that the experimental description of the synthesis of large collections of Janus colloids as well as benchmark experiments are gathered for clarity in appendices A-C at the end of the chapter.*

3.1 The harsh life of swimmers at low Reynolds

Swimming microorganisms are ubiquitous in our world: algae swim in oceans before feeding whales, bacteria travel in our guts, and spermatozoa are challengers during the fertilization race... But one has to keep in mind that the strategies developed by all these microswimmers are very far from *macro* swimming techniques. The frontier between these two "worlds" is related to the Reynolds number, $Re \equiv UL/\nu$ which compares inertial and viscous forces (U and L characteristic velocity and length scales of the swimmer, respectively and ν the dynamic viscosity of the medium). While we experience at the human scale high Reynolds number, typically 10^6 in a swimming pool or during a sprint, a micron-size bacterium moving in water at $10\,\mu$m/s, will present a Reynolds number of $Re = 10^{-5}$. The world of microorganisms is the world of low Reynolds numbers.
In this world, the inertia does not play any role and viscous damping dominates. It can be exemplified by the following situation extracted from the famous paper by Purcell [111]. Let us

imagine that we push a $1\,\mu$m bacterium by a force f to move it at $30\,\mu$m/s. Suddenly, we stop pushing and we wonder how far will it coast before it slows down. Solving the equation of motion with Stokes drag as the only force allows to answer -easily- the question. The bacterium moves 0.01 nm and the transient time before stoppage lasts $0.6\,\mu$s! At low Reynolds a microorganism experiences only the forces exerted and its dynamics doesn't not present any inertial memory of the past. In other words, the Newton's law becomes a simple statement of instantaneous balance between external and fluid forces and torques. Any attempt to move by imparting momentum to the fluid as in a breaststroke is doomed and microorganisms need to develop alternative strategies to overcome and exploit drag.

3.1.1 The scallop theorem.

Generally speaking, the flow field u and the pressure p in the surrounding, incompressible and **newtonian** of with viscosity η, of a swimming organism is given by the Navier-Stokes equation with the appropriate boundary conditions. At low Reynolds, this non-linear equation is reduced to the Stokes equation:

$$-\nabla p + \eta \nabla^2 u = 0 \text{ with } \nabla . u = 0 \qquad (3.1)$$

This equation is linear and independent of time. As a consequence it presents a *kinematic reversibility*. Consider the motion of a solid body with an instantaneous prescribed velocity U and rotation rate Ω together with the flow fluid surrounding it. If we apply the scaling $\mathbf{U} \to \alpha\mathbf{U}$ and $\mathbf{\Omega} \to \alpha\mathbf{\Omega}$, then by linearity the entire flow and pressure field transform as $\mathbf{u} \to \alpha\mathbf{u}$ and

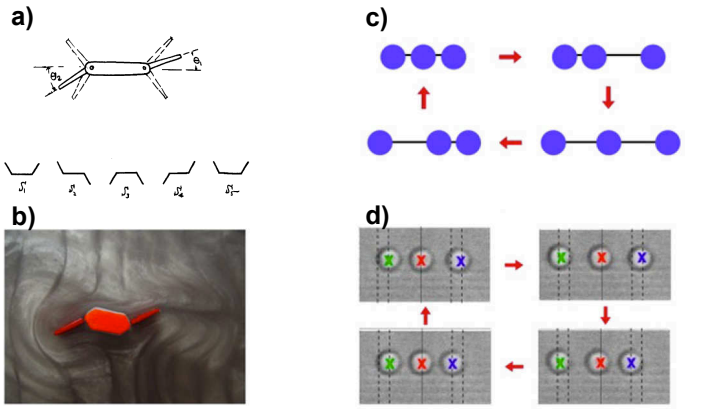

Figure 3.1: **Theoritical swimmers with two discrete degrees of freedom**. *(a)* **Purcell's swimmer.** Original drawing of Purcell's swimmer constituted of three linked rods. The sequence of motion is represented through 5 different conformations to make a non-reciprocal cycle. *(b)* **Macroscopic realization of a Purcell's swimmer.** Extracted from [112] and photo courtesy of Brian Chan and Peko Hosoi. *(c)* **Three-spheres low reynolds swimmers** proposed by Najafi *et al.*. Red arrows indicate change of conformation of the swimmer shape. Thanks to the 2 degrees of freedom, the cycle breaks the time-reversible symmetry and makes a non reciprocal sequence of shapes. Reprint from [112]. *(d)* **Experimental realization of a micropump with colloidal beads and optical tweezers** following the route proposed for the three-sphere swimmers. Reprint from [113].

$p \to \alpha p$. The instantaneous flow streamlines thus remain identical and the fluid stresses undergo a linear scaling, resulting in the symmetry $\mathbf{F} \to \alpha\mathbf{F}$ and $\mathbf{\Omega} \to \alpha\mathbf{\Omega}$, the force and the torque respectively, acting on the body. In particular, when $\alpha = -1$, an instantaneous reversing of the forcing does not modify the flow patterns, but only reverse its direction [112]. In short, at low Reynolds, time makes no difference and only changes in the conformation of the swimmer matter. This result has two consequences. First, the *rate independence* : if a swimmer performs a sequence of shapes, the distance travelled by the swimmer does not depend on the rate at which the surface deformation occur but only on the geometry of the configurations. The second main consequence is what is called the *scallop theorem*. If a swimmer performs a *reciprocal motion*, *i.e.* its body changes its shape and then goes back to the original shape by going through the sequence in reverse, it does not move. Thanks to the linearity and time independence underlined in Stokes equation (Eq- 3.1), fast or slow, the "swimmer" retraces exactly its trajectory. For this reason, a scallop opening its shell slowly and closing it fast squirting out water could not move if it lived at low Reynolds! As well as any animal that would try to swim by a reciprocal motion[1]...

[1] Nevertheless one has to keep in mind that *rate independence* and *scallop theorem* remain true only in newtonian fluids and/or for *individual* swimmers. Hydrodynamic interactions between reciprocal swimmers can break the time-reversibility and lead to collective locomotion. Moreover the dynamics of micro-swimmers in non-newtonian fluids like most biological ones is much more complex than in a newtonian fluid [114–116]. These situations are beyond the scope of this brief introduction on low Reynolds dynamics

Consequently, only systems with at least 2 degrees of freedom in the configuration space can swim. The famous "Purcell swimmer" is an hypothetic animal "like a boat with a rudder at both front and back and nothing else" [111] (see Fig. 3.1-a). It performs a cycle in the configuration space and a net displacement in space. Another theoretical swimmer with 2 degrees of freedom was proposed by Najafi *et al.* with a three-spheres swimmer [117]. An experimental realization of this swimmer, based on the forced motion of three colloidal beads by optical trapping recently showed the success of this system to generate flow [113]. Of course, Nature had to face the specificity of low Reynolds motion much before physicists and and regarding these constraints microorganisms developed in two classes: "corkscrew" and flexible swimmers. *Corkscrew swimmers* continuously rotate their flagella which

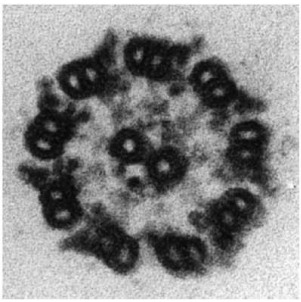

Figure 3.2: **Cross-section of an axonene from wild type** *Chlamydomonas***.** The diameter is approximately 200 nm. We can observe the nine peripheric and the central microtubules doublet separated by dynein motors. Courtesy of Steve King, extracted from [112].

and will not be developed in this manuscript. They are mentioned to point out that surprising situations can come up despite the apparent simplicity of Stokes equation.

propels the swimmer. This strategy is used by *spiroplasma* bacterium (see Fig. 3.3-c) which generates "kinks" to rotate its cork shape [118, 119]. Alternatively,*flexible swimmers* present a flexible flagella acting like an oar. While a stiff oar only presents one degree of freedom and can not propel, a flexible one will deform and change its shape during the first and the second half of the stroke leading to a non-reciprocal cycle. Eukaryotic organisms with flexible flagella and cilia belong to this class of swimmers. The beating is then actuated by a continuous distribution of molecular motors along the filament or *axonene*. The core of a eukaryotic flagellum consists in nine microtubules doublets spaced along the circumference of the flagellum, with two microtubules running along the center. The bending originates in the relative sliding of neighboring microtubule doublets while the sliding is driven by dynein motors regularly spaced along the microtubules (see Fig. 3.2). Non-reciprocal motion is not sufficient for multiflagellated of ciliated organisms, and synchronization of the beating filaments is needed to achieve propulsion. In that respect, the full dynamics of many biological systems goes far beyond the actuation of beating flagella.

The study of these mechanisms is under intensive research, and recent studies underlined the importance of hydrodynamics interactions [120] and flow patterns [121] to couple the beating motors -up to thousands of cilia for *Volvox* [98]- and propel the microorganisms. Nevertheless these results are far beyond the scope of this section -which is to give a general basic intuition of the completely different "way of life" experienced by swimming micro-organisms- and will not be developed here despite their great interest.

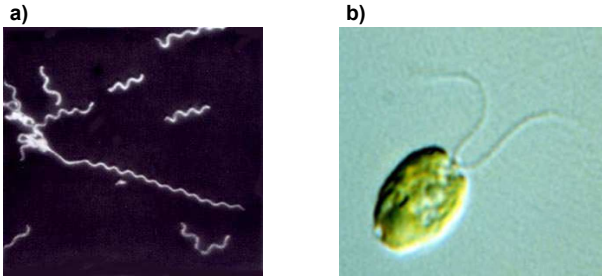

Figure 3.3: *(a)* **Spiroplasma : a corskrew swimmer.** "Kink" propagation in change of handedness of the helix propels the bacterium in viscous fluids [118]. Extracted from the illustrated glossary of plant pathology. *(b)* *Chlamydomonas*, **a flexible flagellated swimmer.** The propulsion of the organism relies on the time-reversibility breakage due to the flexibility of the flagella. The full dynamics of the organism relies on the complex synchronization of the beating flagella out of the scope of this manuscript [120]. Photograph from the Kamiya Lab, University of Tokyo.

3.2 Janus microswimmers

3.2.1 Artificial microswimmers

Besides the intense research to understand the fundamental mechanisms –both in biological and physical perspectives– underlying the motion of living microorganisms, swimming at low Reynolds is a keystone in the race for miniaturization. Microrobotics and microfluidics need autonomous artificial swimmers and motors to carry and perform tasks at small scales. Two different paths have been explored in this quest: a biomimetic approach or the use of interfacial "self-phoretic" phenomena. We consider the latter class of swimmers in this thesis.

Biomimetic swimmers

These synthetic swimmers mimic the surface distortion and swimming strategies that proved to be efficient in biological systems. Such approach was successfully followed by Dreyfus *et al.* to produce magnetic artificial microswimmers [105]. A linear chain of magnetic colloids constituted an artificial flagellum linked to a red blood cell, the head of the artificial organism. An oscillating transverse magnetic field induces a non-reciprocal beating pattern of the colloidal filament mimicking spermatozoa and a net displacement of the so-called "swimmer".

Interfacially-driven microswimmers

An alternative route is to take advantage of physical phenomena predominant at small scales, notably surface effects. Taking their origin in an interplay with the surface, "phoretic" effects

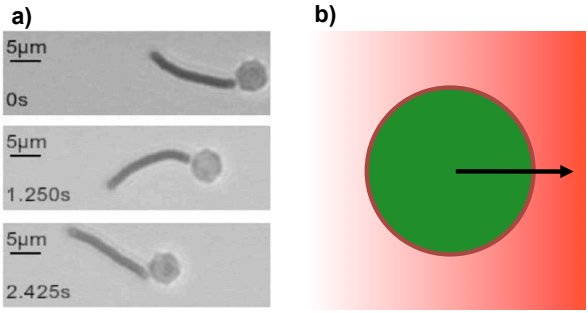

Figure 3.4: **Different strategies to develop synthetic microswimmers.**
(a) **Biomimetic approach.** Like a spermatozoid, the microswimmer has a head (red blood cell) and an tail (flexible magnetic filament). Filament beating is actuated by an oscillating magnetic field and propels the swimmer. Scale bar is $5\,\mu$m. Reprint from [105]. *(b)* **Phoretic swimmers.** A colloidal particle is driven under motion by the gradient of a field (red gradient on the sketch). The diffuse layer -close to the surface- (brown stroke) in a field gradient gives a slip velocity along the particle surface which consequently moves (black arrow).

present a natural path given the increased surface to volume ratio at small scales. As developed in the first part of this manuscript, a gradient of a field (electric potential, temperature, concentration of solute) leads to the motion of particles thanks to interfacial phenomena (electrophoresis, thermophoresis, and diffusio-phoresis respectively). In short, the diffuse nature of the charged interface leads to a slip velocity across the interface and flow generation (see [23] and chapter 1). Experiments such as those we described in the previous chapter underlined the relevance of phoretic phenomena to generate flow and motion at microscale. Macro-molecules and colloids move along temperature gradient by thermophoresis [31,32] or along concentration gradient by diffusio-phoresis [17]. Moreover, heterogeneous nanorods with various catalytic or chemical reactions at their different ends have been reported to propel despite the physical mechanism at the origin of the propulsion remains debated: self electrophoresis [106, 122] or Marangoni effect [107]. The reader interested in phoretic phenomena will find much complete developments in chapter 1.

3.2.2 Janus microswimmers

Janus particles

Janus particles are colloid-sized particles with two hemispheres of different surface chemical composition. Thanks to the asymmetry of their hemispheres, Janus particles appear as proper building block for supraparticular assemblies. This idea was first restrained by the lack of synthetic methods. But in recent years,

important efforts were devoted to the development of chemical engineering that allowed to provide access to particles with a wide range of shape and materials, making synthesis of Janus colloids possible [123,124]. The technological stepforward found applications in domains as diverse as: solid surfactants following the original idea of De Gennes, 'micro-shuttles" thanks to ICEO forces [8,125], or self assembly bricks [126,127] (see Fig. 3.5-a)... The interested reader can will find more informations about the synthesis and additional experimental Janus particles in recent reviews [123, 124].

Janus diffusio-phoretic microswimmers

Based on phoretic phenomena, Ajdari *et al.* proposed a simple model for a microswimmer based on self-diffusio-phoresis [110, 128]. A colloid is driven by an asymmetric chemical activity taking place on its surface and a consequent gradient of reaction products and reactants (see figure Fig. 3.5-b). In order to use the surrounding medium as an infinite reservoir and do not consume the colloid, the chemical activity of the surface should be catalytic. While Ajdari *et al.* addressed various and complex distributions of the chemical activity, we will focus on the case of the *Janus* colloids, *i.e.* one half chemically active and the other half bare. These Janus particles are conceptually easier to consider and developed experimentally. As well they constitute the first piece of all the experimental work we perform on swimmers.

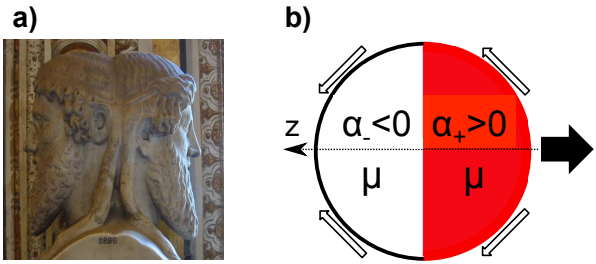

Figure 3.5: **Janus Microswimmers.** *(a)* **Bust of Janus**, roman god of gates, doors, beginnings and endings. He is most often depicted as having two faces in opposite directions looking both into the future and the past. Sculpture from Vatican Museums collections. *(b)* **Spherical Janus particle** sketched up by Ajdari *et al.*. The mobility μ is homogeneous on the sphere, while the chemical activity α depends on the hemisphere. The left half produces solute of concentration c with a constant surface reaction rate $\alpha_+ > 0$ while the right (red) hemisphere consumes c with a constant surface reaction rate $\alpha_- < 0$. The flux of the solute species is described by the open black arrows. The net swimming velocity of the particle is given by the thick black arrow (for $\mu > 0$). The formal description of the mechanism is developed in part 3.2.2.

Diffusio-phoretic propulsion

Self-propelled colloids generate themselves the gradients of concentration and move thanks to diffusio-phoresis. For the sake of simplicity, we consider the simple situation of only one solute at a given concentration $c(\mathbf{r}_s)$, where $\mathbf{r}_s$ is the considered position on the solid surface. The chemical activity is simplified in a consumption or creation of this species. The diffusio-phoretic velocity is proportional to the gradient and yields to:

$$V = \mu \nabla c \tag{3.2}$$

where μ is the so-called diffusio-phoretic mobility of the particle. At steady state, in the reference frame of the particle, and neglecting the effects of the motion of the colloid in the transport of the salt at small Peclet number [128] the solute concentration is given by:

$$\begin{cases} D\nabla^2 c = 0 \\ -D\mathbf{n} \cdot \nabla c(\mathbf{r}_s) = \alpha(\mathbf{r}_s) \end{cases} \tag{3.3}$$

where D is the solute diffusion coefficient. $\alpha(\mathbf{r}_s)$ measures the chemical activity of the surface at position $\mathbf{r}_s$, *e.g.* the generation or the consumption of the solute by the catalytic reaction on the surface. We assume for simplicity that α is a constant at given position on the surface, and only depends on the catalyst present at this point[2].

[2] *A priori*, the chemical activity is a complex quantity which depends on the number of available catalyst sites and on the concentration of solute at a given position. As a consequence, our assumption is not obvious.

The concentration gradient of Janus particles develops on the particle size R and Eq- 3.2 thus rewrites dimensionaly $V \sim \mu\Delta c/R$, where Δc is the typical concentration difference between the poles of the colloid and originates in the chemical reaction. Using equation 3.3 dimensionally leads to a typical propulsion velocity:

$$V \propto \alpha\mu/D \qquad (3.4)$$

This expression underlines the importance of the competition between the reaction rate α and the diffusivity D of the considered solute to maintain a driving force *via* the solute gradient. Moreover, for a given pattern of surface properties and particle shape, the velocity of the self-propelled particle is independent of the swimmer size R. This result is quite different from the scaling of the velocity for an object propelled by a body force F, *e.g.* gravity: the force $F \propto R^3$ is balanced by the Stokes viscous drag which leads to a velocity $V \propto R^2$. This point emphasizes the robustness to downsizing of phoretic motor and notably diffusio-phoresis for propulsion[3].

Nevertheless if the solvent contains an excess of the reactants necessary to produce or destroy the solute of interest, the density of active catalytic sites on the surface is what limits the reactions. In this case, α is reduced to a reaction rate constant per surface unit. $\alpha > 0$ represents the number of molecules of the solute of interest generated at the surface per second and per surface unit [128]. In our case, the solution acts as an infinite reservoir and one can reasonably think that the chemical reaction on the catalytic sites limit the reaction. Anyway, this hypothesis allows to catch the physics and the feeling of the phenomenon.

[3]The above description is especially derived in the case of self -diffusiophoretic swimmers, but the general formalism is still valid for any phoretic phenomenon. A particle which autonomously generates an electric field

A full resolution of the previous equations can be performed beyond the dimensional arguments. We consider chemical Janus colloids which generate autonomously the gradients of concentration *via* catalytic reactions on the two hemispheres. They are covered with two different catalytic materials with different chemical activities α_+ and α_-. In general, the mobilities can also differ for the speciess on each side and we note the μ_+ and μ_-. Ajdari *et al.* derived the full expression for the diffusiophoretic velocity of the swimmer [110]:

$$V = \frac{1}{8}\frac{1}{D}(\alpha_+ - \alpha_-)(\mu_+ + \mu_-)\hat{\mathbf{e}}_z \qquad (3.5)$$

This result once again pinpoints the importance of the symmetry breaking in the chemical activity to propel the colloid.

Platinum-bare Janus microswimmers

Howse *et al.* proposed in a recent work a route to synthesize artificial colloidal microswimmers [108]. Following the scheme proposed in the previous section and recent results of autonomous motion of platinum-gold nanorods [106,129], he synthesized platinum-bare *active* colloids. One half of a commercial latex colloid is coated by a thin layer (typically a few nm) of platinum while the second hemisphere of the colloid remains bare namely a *Janus colloid* (see figure Fig. 3.6-a).

Chemical reaction.

or thermal gradient will move along this gradient by, respectively self-electrophoresis or self-thermophoresis.

Hydrogen peroxide H_2O_2 aqueous solution (in the range 0 to 10% w/v) is added to the colloidal suspension of Janus particles. While hydrogen peroxide is thermodynamically unstable, it does not dismute at room temperature. The kinetic blockage is passed if the hydrogen peroxide solution is put in contact with an organic residue or any transition metal. The reduction of hydrogen peroxide then produces water and oxygen following the reaction:

$$2\ H_2O_2 \rightarrow O_2 + 2\,H_2O$$

Platinum-bare Janus particles thus present differential spatial chemical activity with hydrogen peroxide: the platinum side of the Janus catalyses the dismutation of H_2O_2 while the bare half is chemically inert. With the notation of the previous part, the chemical activity on the platinum side is $\alpha_{Pt} = \alpha \neq 0$, and the chemical activity on the bare side is $\alpha_b = 0$.
Finally, the particle presents on one side products of the reaction and on the other side a consumption of reactants. The chemicals gradients propel the particle by self-diffusio-phoresis, accordingly to equation Eq- 3.5 and assuming equal diffusiophoretic mobility of the speciess $\mu_+ = \mu_- = \mu$, the velocity (Eq- 3.5) rewrites as follows:

$$V_{DP} = \frac{\mu\ \alpha_{Pt}}{4D_0} \qquad (3.6)$$

Note that additionally to the solute gradient, the chemical reaction may also induce a temperature gradient. The dismutation reaction of hydrogen peroxide is indeed strongly exothermic ($\Delta_f H^0 = -188\,\mathrm{kJ/mol}$) and local heating along the platinum hemisphere may induce a temperature gradient propelling the

colloid thanks to thermophoresis. In our experiments, the apparent velocity $\tilde{V}$ is in a first approximation the sum of the different phoretic velocities:

$$\tilde{V} = V_{DP} + V_T \tag{3.7}$$

where V_{DP} is the diffusio-phoretic velocity of the particle in the solute gradient generated by the chemical reaction and V_T is the thermophoretic velocity of the particle in the thermal gradient generated by the exothermic dismutation. As our objective is to synthesize artificial microswimmers, we do not try to separate and extract the different phoretic contributions of the particles motion and focus on the measurement of propulsion velocity $\tilde{V}$ denoted as V in the following.

Howse has demonstrated that the particles added in a solution of "fuel" -H_2O_2- are propelled at a given velocity V whose amplitude is controlled by the concentration of fuel accordingly to a Michaelis-Menten behavior for the decomposition of hydrogen peroxide on platinum [108]. The velocity first linearly increases with the fuel concentration and then tends to saturate (see figure Fig 3.6-b) which can be interpreted as : *(i)* H_2O_2 forms a complex $[Pt(H_2O_2)]$ with rate per unit area $k_1[H_2O_2]$ and *(ii)* decomposes into water and oxygen with a rate per unit area k_2 independent of the peroxide concentration. Finally the effective surface reaction rate α, defined on equation Eq- 3.5, can be expressed as:

$$\alpha = k_2 \frac{[H_2O_2]}{[H_2O_2] + k_2/k_1} \tag{3.8}$$

The parameters k_1 and k_2 can be extracted by fitting the velocity dependence on hydrogen peroxide concentration and accord-

ing to equation Eq- 3.6. This derivation presents a very good agreement with experimental measurements (see Fig.3.6-b).

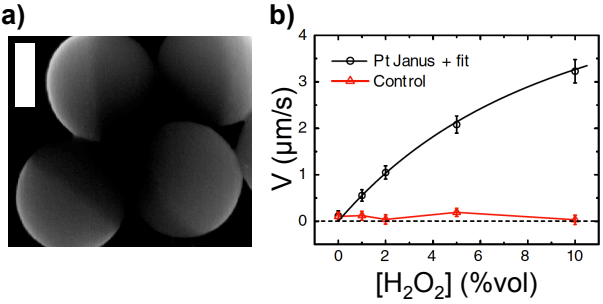

Figure 3.6: *(a)* **SEM picture of Janus**, platinum-latex , colloids (scale bar 500nm) synthesized during my PhD. The platinum coating is 2 nm on one hemisphere of the colloid and appears bright on the picture. The contrast is enhanced to enforce the brightness difference between the platinum and bare hemispheres. Grateful acknowledgments to J.M. Benoit. *(b)* **Velocity measurements for platinum-bare Janus colloids (black) or bare colloids (red)**. They are obtained for various concentration of the H_2O_2 fuel (expressed in $\%/vol$). The solid black line represents the fit of the velocity following a Michaelis-Menten kinetics for the dismutation of hydrogen peroxide on platinum. Reprint from [108].

The first part of this chapter reported previous results in the literature on microswimmers, *e.g.* low Reynolds number dynamics, Janus chemical microswimmers... From this point, I will discuss now original contributions to the field from my PhD work.

3.2.3 From individuals to larger collections of microswimmers

In the present work, we followed the route proposed by Howse *et al.* to build microswimmers [108]. Our final aim is to study the out-of-equilibrium properties of collectives of active self propelled particles. This *(i)* requires to build up large collections of Janus particles with "not too small" volume fraction –typically $\Phi \sim 0.05 - 0.1\%$– which *(ii)* leads to some experimental difficulties.

Synthesizing large number of Janus particles

Inspired from the synthesis of Janus colloids proposed by Howse *et al.* I developed an improved protocol to strongly increase the number of particles synthesized. A sufficient efficiency is required to obtain "concentrated" solutions of swimmers and explore the physics of suspensions beyond the *"infinitely dilute"* regime. As the process is mainly technical, the detailed protocol of the synthesis of platinum-bare Janus colloids is displaced in Appendix C at the end of the chapter and I present here only a summary.
A commercial solution of colloids is diluted –typically 200 times– in isopropanol and sonicated. A drop of the solution is deposited in a thin film on the *rough* side of a tilted $4''$ silicon wafer. The roughness of the the substrate captures the contact line during the evaporation of the alcohol leading to an *uniform dewetting* of the film and the formation of a monolayer of individual colloids, *i.e.* without ring stains. A thin layer of platinum (typically

$2-5\ nm$) is coated on the wafer by sputtering and one obtains platinum-bare Janus particles by shadowing effect. The particles are resuspended in pure water by sonication of the wafer and the solution is reconcentrated by centrifugation to finally obtain a Janus suspension of $\sim 50\,\mu$l with a maximal volume fraction $\Phi \sim 0.1\%$.
Nota Bene. The rough substrate prevents ring stains and droplets formation and strongly increases the density of the monolayer of colloids. In addition with the use of large $4''$ substrate, this experimental protocol makes possible the synthesis of large collections of Janus particles.

Unlocking experimental difficulties: a gel device

"Concentrated" suspensions of Janus particles (with volume fraction in the range $\phi \sim 0.01-0.1\%$) arise experimental difficulties. Large collections of swimmers *(i)* consume fuel -H_2O_2- and *(ii)* produce oxygen and oxygen bubbles which pollute the experiment. *(i)* can be verified experimentally monitoring the swimming velocity V along time checking that it remains constant[4] during the experiment. But *(ii)* prescribes the use of glass capillaries or "traditional" enclosed systems as observation cells. The released oxygen exceeds solubility in the bulk and gas bubbles appear. They strongly disturb measurements as they lead to fast recirculation flows and leakage.
In order to unlock these experimental difficulties, I developed a specifically designed microfluidic system based

[4] As pinpointed previously by Howse results, the amplitude of the propulsion velocity is related to the fuel concentration in the bulk.

on a gel-microdevice technology allowing a constant renewal of the *chemical fuel*, as well as removal of the *waste*, in an open reactor configuration.

A Gel microfluidic device
The swimmers are enclosed in a dedicated microfluidic device molded in agarose gel following the idea described in the previous chapter and inspired by [44]. Let us remind that the hydrogel nanoporous matrix acts as solid walls for the flow but allows free diffusion of molecules. The mold design is made of a circular microfluidic chamber and surrounded by two side channels separated by gel walls (see Fig. 3.10-a). The central chamber is initially filled with Janus colloids in water, while H_2O_2 solution at concentration C_0 is continuously circulated in lateral channels. This gel microsystem ensures a constant renewal of H_2O_2 fuel and removal of chemical waste products (O_2) by diffusion through hydrogel walls from the infinite reservoir and sink constitued by the circulating lateral channel. This provides a convection-free environnement[5] in the colloids chamber with stable chemical conditions over hours, allowing to study large assembly of active colloids. A similar study in a sealed capillary would be limited to a few seconds by the production of oxygen bubbles. Unlocking the main experimental problems related to the use of large collections of swimmers, we demonstrate the relevance of gel microfluidic tools to explore the properties of active colloidal suspensions.
Nevertheless, the hydrogel technology presents specificities. H_2O_2

[5] With a typical drift $V < 20\,\mathrm{nm/s}$, see chapter 2.

diffuses through the gel walls and alters the hydrogel structure. In order to quantify the consequences of the hydrogel aging, we performed benchmarks experiments reported in the Appendix B of this chapter. The gathered results of the benchmark are reported on figure 3.7-b. The conclusions of these benchmark experiments can be summarized as:

1. After a few hours in contact with hydrogen peroxide, the diffusivity of the colloids reaches a plateau $D_0 = 0.34 \pm 0.02\,\mu\text{m}^2/\text{s}$ independent of the H_2O_2 concentration and which remains stable up to 36 hours.

2. Beyond this time the degradation of the gel by H_2O_2 system is too strong to ensure good reliability of the system.

In the following experiments, we will inject H_2O_2 for a few hours before measurements of the mean squared displacement to attain the "steady" viscosity and take D_0 as the equilibrium value of the diffusion coefficient of 1μm Janus colloids enclosed in gel microfluidic device.

3.3 Microswimmer dynamics: a persistent random walk

We first characterize the individual dynamics of the active colloids using high speed tracking measurements for proper temporal resolution. While tracking the trajectories can be properly performed in a dilute sample from colloids films, we perform simultaneously sedimentation measurements (see next section).

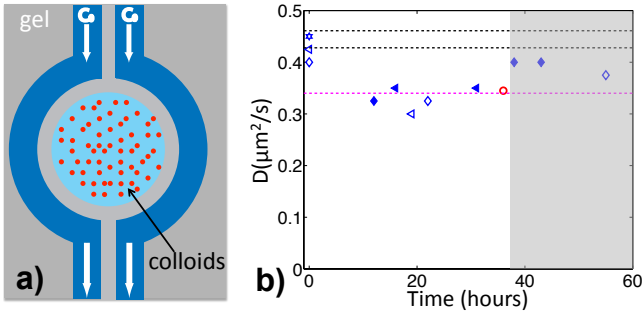

Figure 3.7: *(a)* **Sketch of the gel microfluidic device.** The design is made of a circular microfluidic chamber surrounded by two side channels separated by gel walls. The central chamber is initially filled with Janus colloids in water, while H_2O_2 solution at concentration C_0 is continuously circulated in lateral channels. This gel microsystem ensures a constant renewal of H_2O_2 fuel and removal of chemical waste products (O_2) by diffusion through hydrogel walls from the infinite reservoir and sink constitued by the circulating lateral channel. This provides a convection-free environnement to study mean squared displacements of colloids with high speed camera. *(b)* **Benchmark experiments on the effect of H_2O_2 on the gel device.** We quantify the effect of H_2O_2 on the gel structure with diffusion constants monitoring. The diffusion constants are extracted from mean squared displacements measurements *at equilibrium* for bare (blue) or Janus (red) colloids at. The diffusion coefficients measurements are performed at different times, in water (open symbols) and H_2O_2 (full symbols). ($\star$) is for an experiment in a glass capillary, the other experiments are performed with hydrogel systems. Black dashed lines represent the Stokes-Einstein equilibrium expectations $D_{SE} = 044 \pm 0.02\,\mu m^2/s$. The measured diffusion constants agree with this value just after the introduction in the microfluidic chamber (glass or gel). It then decreases to $D_0 = 034 \pm 0.02\,\mu m^2/s$ (magenta dashed line) with the introduction of H_2O_2 and remains stable up to 2 days for various concentration of hydrogen peroxide or in water. Beyond 2 days, the hydrogel presents aging and gets brittle. Measurements are then not reliable (grey zone).

For this purpose, one has to handle "concentrated" solutions of Janus particles (volume fraction $\phi \sim 0.01\%$) which requires, as discussed above, the use of the gel microdevice.

3.3.1 Dynamics of microswimmers

Experimental protocol

Measurements of the dynamics of microswimmers are performed for various H_2O_2 concentrations C_0 (in the range 0 to 10%) in a circular microfluidic chamber (diameter $\Phi = 650\,\mu$m, height$\simeq$ $80\,\mu$m, volume $V \simeq 30\,$nl) and surrounded by two side channels separated by $125\,\mu$m gel walls. The two-dimensional (x,y) motion of colloids is followed by fluorescent microscopy with a high speed camera (Phantom V5) at 100 Hz and carried on an inverted microscope (DMI4000B, Leica) with a 60× objective, water immersion and high numerical aperture (60x, Water Immersion, N.A.=1.2, Nikon). The (2D) instantaneous colloid positions $\mathbf{r}(t)$ are extracted from stack of images (typically 4000) with a single particle tracking algorithm (Spot Tracker, Image J [130]) to define the trajectories of the particles. As the origin of the movie is arbitrary, we perform sliding time average on the position denoted $\mathbf{r}(\Delta t)$ for a given time lag Δt which is *(i)* the relevant observable and *(ii)* strongly increases the statistics of "short" times measurements. Finally, the mean square displacement of the colloids at given fuel concentration C_0 is obtained computing $\Delta L^2(\Delta t) \equiv \langle(\mathbf{r}(t+\Delta t) - \mathbf{r}(t))^2\rangle$ where the average is performed over time for each individual trajectory and then over an ensemble of trajectories denoted by $\langle\cdot\rangle$. We

consider typically 20 independent particles which is sufficient for a statistical convergence.

Mean squared displacements

We plot in figure 3.8 $\Delta L^2(t)$ as a function of time for bare (non-active) and active colloids in a solution of hydrogen peroxide, confirming the impact of injected chemical power on the individual motion of the colloids, in agreement with Ref. [108].

Equilibrium Experiments
For bare (non-active) colloids, the dynamics is purely diffusive *i.e.* the mean squared displacement is linear with time, and we extract from the slope the diffusion coefficient of the colloid $\Delta L^2/4\Delta t = D_0 = 0.34 \pm 0.02\,\mu\mathrm{m}^2/\mathrm{s}$, which is found to be independent of the H_2O_2 concentration (see Fig. 3.7-b and Appendix B). We have furhermore measured the same value D_0 for the diffusion coefficient of Janus colloids in pure water, *at equilibrium*, in the absence of H_2O_2 fuel. This value for the equilibrium diffusion coefficient of $1.1\,\mu$m colloids is significantly smaller than the equilibrium Stokes Einstein value $D_{SE} = 0.44\,\mu\mathrm{m}^2/\mathrm{s}$ with the bulk water viscosity. As discussed above and in Appendix B, we infer that the difference is due to an increase of the viscosity of the hydrogen peroxide solution due to solubilized agarose gel.

Janus swimmers
For the Janus active colloids in a hydrogen peroxide solution, the mean square displacement differs drastically from the equi-

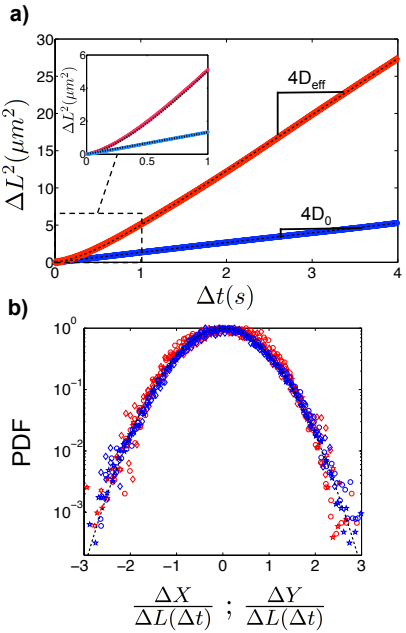

Figure 3.8: (a) **Experimental mean squared displacements** $\Delta L^2(\Delta t)$ for bare (blue) and active colloids (red) in 7.5% H_2O_2 solution. Bare colloids (bottom) show standard diffusion (ΔL^2 linear in time), while the mean squared displacement of active colloids is fitted according to equation (3.12). The measured diffusion coefficients are $D_0 = 0.33\,\mu\text{m}^2/\text{s}$ for bare and $D_{\text{eff}} = 1.90\,\mu\text{m}^2/\text{s}$ for active colloids. *(Inset)* Zoom of the mean squared displacement at short times scales. (b) **PDF of particle displacement** ΔR **for various lag time** Δt as a function of the normalized displacement $\Delta R/\Delta L(\Delta t)$. Δt=0.3 s ($\star$), 1 s ($\circ$), 3 s ($\diamond$) for bare (blue) and active colloids (red) in a solution of 7.5% of H_2O_2. The dashed lines is the gaussian equilibrium prediction.

librium diffusive dynamics and strongly depends on the fuel concentration. The colloid exhibits ballistic motion at short times, $\Delta L^2(t) \sim V^2 t^2$, while at longer times a diffusive regime, $\Delta L^2(t) \sim 4D_{\text{eff}}t$, is recovered with an effective diffusion coefficient D_{eff} much larger than the equilibrium coefficient D_0.

A persistent random walk
As discussed in [108,131], the active colloids perform a *persistent random walk*, due to the competition between ballistic motion under the locomotive power (with a constant swimming velocity V) and angular randomization by thermal rotational Brownian motion. The transition between the two regimes occurs at the rotational diffusion time τ_r of the colloids. Physically, this time scale represents the time for the direction of the particle to decorrelate. As the propulsion direction of a Janus swimmer is perpendicular to the equator of the colloid, τ_r also appears as the time scale for which the direction of propulsion decorrelates. For $t \ll \tau_r$, the colloid propels along the direction $\hat{\mathbf{u}}$ perpendicular to the equator and the rotational diffusion of the colloid is negligible. The colloid goes along a straight line with velocity V. For $t \sim \tau_r$, a colloid crossed the distance $V\tau_r$ along $\hat{\mathbf{u}}$. Then the direction of the propulsion is randomized and the colloid now propels along a new direction $\hat{\mathbf{u}}'$ decorrelated from the previous one. Finally, for $t \gg \tau_r$, the swimmer performs random steps of length $V\tau_r$ with direction randomized at rate τ_r^{-1}. Taking into account the thermal diffusivity D_0 of the colloid, the swimmer behaves at long times as a Brownian particle with an effective

diffusion coefficient :

$$D_{\text{eff}} = D_0 + \frac{1}{6} V^2 \tau_r \tag{3.9}$$

The full expression of the mean squared displacement at any time is given by [108] (where we corrected one prefactor). We present here the basics ingredients of the calculation and the full derivation can be found in Appendix C.
The swimmer obeys the Newton's equation:

$$\frac{d\mathbf{r}}{dt} = V\hat{\mathbf{u}}(t) + \frac{\tilde{\mathbf{f}}(t)}{m} \tag{3.10}$$

with V the swimming velocity along the (fluctuating) direction $\hat{\mathbf{u}}(t)$, m the mass of the particle, and $\tilde{\mathbf{f}}(t)$ the random force associated with the classical Brownian motion [13].
The mean squared displacement of the particle rewrites:

$$\langle (\mathbf{r}_s(t) - \mathbf{r}_s(0)\rangle^2 = V^2 \int_0^t ds\,(t-s) C(s) \tag{3.11}$$

with $C(s) = \langle \hat{\mathbf{u}}(s) \cdot \hat{\mathbf{u}}(0) \rangle$. Given the expression for the correlation function $C(t) = \exp[-2/\tau_r]$ (see Appendix C), we obtain the full expression for the 2D MSD which is the experimental observable:

$$\Delta L^2(\Delta t) = 4D_0 \Delta t + \frac{V^2 \tau_r^2}{3} \left[\frac{2\Delta t}{\tau_r} + e^{\frac{-2\Delta t}{\tau_r}} - 1 \right] \tag{3.12}$$

This dynamics is formally analogous to the dynamics of a Brownian particle predicted by a *Langevin model*, the microscopic

inertial time scale ($\sim$ ns) being replaced by the rotational time ($\sim$ s for 1 μm colloids).

Back to the experiment
We fit the experimental mean squared displacement (MSD) $\Delta L^2(\Delta t)$ using equation 3.12 with the propulsion velocity V as the only fitting parameter, while the value of D_0 is taken from the equilibrium diffusion coefficient measured in water for Janus colloids or in H_2O_2 for bare colloids. The rotational diffusion time τ_r is set at a constant value $\tau_r = 0.9$ s in good agreement with Stokes expectation $\tau_r = 8\pi\eta R^3/k_BT$ (for experiments with colloids of radius $R = 0.55\,\mu$m at 25°C in water $\eta(25°\text{C}) = 0.890$ mPa.s)[6]. As shown in Fig. 3.8-a, an excellent agreement with the experimental results is found with only one free parameter. The very good fit lasts for times smaller than the rotational diffusion time $\Delta t < \tau_r$ as well as for times larger that this cut-off[7].
This supports the *persistent random walk* –with persistence time τ_r and velocity V– to model the dynamics of microswimmers. Under the present conditions, we measure V in the range from 0.5 μm/s to 2.9 μm/s. In terms of enhanced diffusion, the effective diffusion constant D_{eff}[8] can be increased by the swimming

[6] Nevertheless the fit is weakly sensitive on the precise value of τ_r in the range $0.8-1$ s. As a consequence, we set the value to the Stokes equilibrium expectation. The translational propulsion of the swimmer is not expected to impact the angular balance between fluctuation and dissipation defining τ_r. This allows to use only one fitting parameter in equation 3.12.

[7] We also want to stress that we fit 400 data points with only one parameter.

[8] D_{eff} is obtained by measuring the slope in the linear region of the MSD *i.e* $\Delta t \gg \tau_r$

activity by a factor up to 5.5 compared to the equilibrium constant.

In the following we use this measure of D_{eff} as a probe of the colloidal "activity".

Probability distribution function

We can also extract from the trajectories of the colloids the probability distribution function (PDF) of the displacement. To a certain extent the PDF is mainly a convenient way to rephrase previous results with more sensitive *statistical physics tools* to probe events like long time tails, intermittent dynamics... We measure the PDF of the colloid displacement along x and y directions for a given time lag Δt both for bare (blue) and active (red) colloid particles (see Fig.3.8-b). We check that *(i)* the PDF along x and y can be superimposed and *(ii)* are even with respect to the zero axis for any time which ensures that there are no experimental bias! Finally, for both bare and active colloids, the PDF fits very well to a gaussian with variance $\Delta L^2(\Delta t)$ given in equation 3.12.

Although departures from a gaussian are expected at short time for the persistent random walk, these are within experimental uncertainty and we can not reasonably infer any specific *out of equilibrium* signatures from the PDF measurements. Indeed, more sophisticated theoretical predictions can also be performed on the dynamics of stochastic dynamics of diffusio-phoretic swimmers. In particular, Golestanian identified three times scales separating four different regimes for Janus particles and showed non-markovian effects due to the diffusion of the chemical cloud and anomalous diffusion behaviors [132]. These long-time cor-

relations due to chemical relaxation are of premier importance from a fundamental point of view, nevertheless the experimental validation of this result could be tricky: the contribution of these effects dominate at nm and ns in water and are robust to change in the colloid size and only depends on the viscosity of the medium.
To summarize, the active colloids are expected to perform a persistent random walk of persistence time τ_r due to the competition between ballistic motion under the locomotive power (with a con- stant swimming velocity V), and angular randomization due to thermal rotational Brownian motion.

3.4 Sedimentation of active colloids

In the previous section we addressed and characterized the dynamics of individual Janus particles and showed an out of equilibrium behavior of swimmers finally leading to an enhanced diffusion coefficient D_{eff} at long time-scale. The next step is to characterize the statistical behavior of an assembly of swimmers. Following a natural avenue in equilibrium statistical physics, we now turn to the response of a collection of active particles in a force field. In this scope we investigate the sedimentation properties of such an active suspension under gravitational field in the same spirit as the historical experiment performed by Jean Perrin in 1909 [133].

3.4.1 *"Mouvement brownien et réalité moléculaire"*, Jean Perrin (1909)

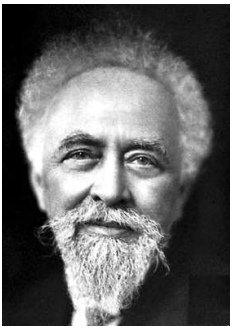

Figure 3.9: **Jean Perrin** received in 1926 the Nobel Prize in Physics for "his work on the discontinuous structure of matter, and especially for his discover of sedimentation equilibrium". Reprint from nobelprize.org

At thermal equilibrium with a bath at temperature T, it is well known from most physics text-book that a dilute population of colloid with (buoyant) mass m under gravity g exhibits a steady Boltzmann distribution profile which reads [134]:

$$\rho(z) = \rho_0 \exp(-z/\delta_0) \qquad (3.13)$$

with $\delta_0 = k_B T/mg$ the sedimentation length, which balances gravitational and thermal energy. This sedimentation equilibrium was first observed and quantified by Jean Perrin (1909) and represented a crucial step forward to establish the discontinuity of matter beyond doubt (Nobel Prize 1926). Alternatively, a microscopic modeling of the situation can also be performed. In this perspective, this density profile can be seen as the stationary solution of the Smoluchowsky diffusion-convection equation $\partial_t \rho + \nabla \cdot \mathbf{J} = 0$ with $\mathbf{J}$ the particle flux. The particles flux is the sum of a Fick term $\mathbf{J}_D = -D_0 \nabla \rho$ and a flux induced by a force field $\mathbf{J}_F = \mu \mathbf{F}$ with D_0 and μ the colloids diffusion coefficient and mobility.

Finally in the gravity field, the total flux of particles rewrites

$$\mathbf{J} = -D_0 \nabla \rho + \mu\, m\mathbf{g}\, \rho \qquad (3.14)$$

At equilibrium, the total flux is zero and the distribution profile of particles is given by $\rho(z) = \rho_0 \exp(-z \times \frac{mg\mu}{D_0})$. Matching the steady profile with the Boltzmann distribution of the population, one deduces the Fluctuation-Dissipation Theorem (FDT): $D = k_{\mathrm{B}} T \mu$.
In order to explore the validity of these concepts for the out-of-equilibrium active suspension, we have measured simultaneously to the individual particle tracking experiments the density profiles $\rho(z)$ of the colloids in the microfluidic chamber, for various fuel concentrations C_0 and related varying propulsion velocities.

3.4.2 Sedimentation of active swimmers

Experimental protocol

Colloid profiles are measured by scanning the chamber using a piezo-mounted microscope objective (PIFOC P-725.2CD, Physik Instrumente).
The microscope is first focused at $z = 0$, *i.e.* at the bottom of the microfluidic chamber, then a piezo is used to displace the focus point along the z axis with high accuracy. At each altitude z, a stack of images with lateral dimensions $150 \times 200\,\mu$m is acquired at 0.3 Hz with a fluorescence camera (Orca, Hamamatsu) and a 60x objective (60x, WI, N.A. 1.2, Nikon). A sketch of the experiment is depicted in figure 3.10. We use a high numerical

aperture (N.A.) objective[9] to define with good accuracy a slice of depth δ around the focus plane. On each stack, image analysis is performed with Matlab: first the maximum fluorescence intensity I_{foc} is determined from "in-focus" colloids, then a $0.3\,I_{foc}$ threshold criterion is applied in order to discard out-of-focus colloids, thus defining a slice with thickness of $\pm\ 2\,\mu$m [135] (see Appendix D for an experimental determination of the z dependence of fluorescence intensity $I(z)$). A stack of 100 images is used to obtain a good statistical convergence. Overall this allows to obtain the average number of colloids at each altitude z. Note that the adsorption or aggregates of colloids on the bottom surface are found to bias the density profiles for small altitudes z and we accordingly discard data from the first slices, *i.e.* we limit ourselves to $z \geq 5\,\mu$m.
We validated the experimental setup and protocol with equilibrium systems, i.e. bare colloids in H_2O_2 or Janus particles in water. The details of the benchmarks experiments are gathered in Appendix D at the end of the chapter.

Experimental results

The results of these "Jean-Perrin" experiments are presented in figure 3.11. We have first checked that a *stationary* state of the sedimentation profile is reached which is *a priori* a non-trivial point for an out of equilibrium phenomenon.
As shown in figure 3.11, the density profiles $\rho(z)$ of the active

[9] With consequently small depth of field $\delta_f \sim \frac{\lambda_0 n}{NA^2}$ with λ_0 the wavelength of the considered light and n the refractive index of the medium of immersion (here water)

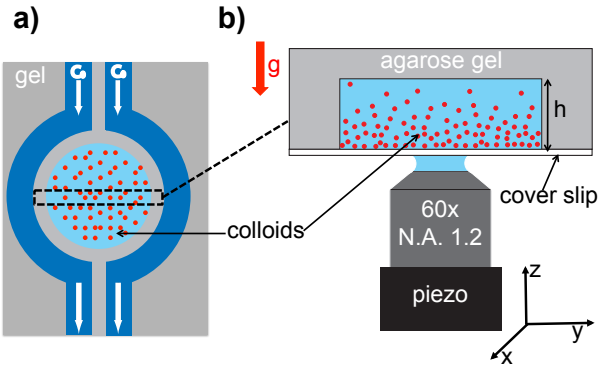

Figure 3.10: (a) **Sketch of the experimental setup.** A circular microfluidic chamber (diameter $\Phi = 650\,\mu$m, height $h \sim 80\,\mu$m) molded in agarose gel (gray areas) contains the $1\,\mu$m Janus colloids. H_2O_2 feeding is achieved by constant circulation (40μL/min flow rate) in side channels (dark blue). (b) **z-profile measurements.** The active colloidal suspension is observed through a piezo-driven high numerical aperture objective (Nikon, Water immersion 60×, N.A.=1.2) mounted on an inverted microscope.

colloidal suspension decreases with the altitudqe z and as in the equilibrium case can be very well fitted by an exponential decay $\rho(z) = \rho_0 \exp(-z/\delta_{\rm eff})$, where ρ_0 is used to normalize the different measurements[10]. We measure $\delta_{\rm eq} = 6 \pm 1\,\mu$m for equilibrium experiments with Janus colloids in water in good agreement with the theoretical expectation $\delta^*_{eq} = 5.5 \pm 0.5\,\mu$m for $1.1\,\mu$m latex colloids half-coated with 2 nm of platinum. We

[10] Note that the total number of colloids in the observation window ranges typically from $5.\,10^3$ to $3\,10^4$.

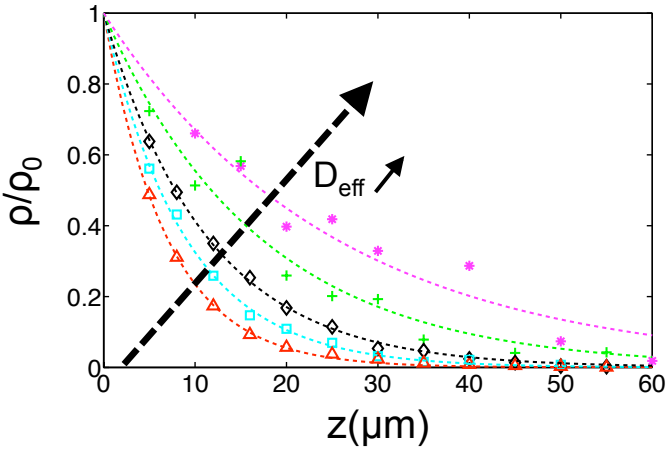

Figure 3.11: **Sedimentation profile in active suspensions.** Normalized density profiles $\rho/\rho_0(z)$ for the active colloidal suspension in stationary state, for increasing swimming activity, *i.e.* increasing $D_{\rm eff}$. Experimental data (symbols) are well fitted by an exponential decay $\rho(z) = \rho_0 \exp(-z/\delta_{\rm eff})$, with a sedimentation length $\delta_{\rm eff}$, which strongly depends on (and increases with) the swimming activity. Here $\delta_{\rm eff}$ varies from 6 μm at equilibrium up to 21 μm. *(Inset)* Same datas in a log-linear plot.

point out the large difference of sedimentation length between *Janus* and bare colloids in water (see Appendix D) due to the *heavy* cap of platinum of density $d_{Pt} = 20$. The sedimentation length δ_{eff} is found however to depend strongly on the activity of the colloids (see Fig. 3.11): δ_{eff} increases with an increased propulsion of the colloids, *i.e.* injected energy, as measured (independently) by their effective diffusion coefficient D_{eff} (see previous section).

Effective temperature of an active suspension

The exponential decay suggests that in the present limit of a dilute active suspension, the active colloids still obey an effective Smoluchowsky equation, with the current replaced by $\mathbf{J} = -D_{\text{eff}}\nabla\rho + \mu\, m\mathbf{g}\,\rho$. This predicts at steady state a sedimentation length in the form

$$\delta_{\text{eff}} = \frac{1}{v_T} \times D_{\text{eff}}, \qquad (3.15)$$

where $v_T = \mu\, mg$ is the sedimentation velocity in the gravity field.

We have checked this relationship by plotting the sedimentation length δ_{eff} measured from the colloid density profiles, against the effective diffusion coefficient D_{eff} measured in the individual tracking measurements. As shown in figure 3.12, the predicted proportionality between sedimentation length and effective diffusion coefficient is demonstrated experimentally for all propelling activities, with a proportionality constant which is

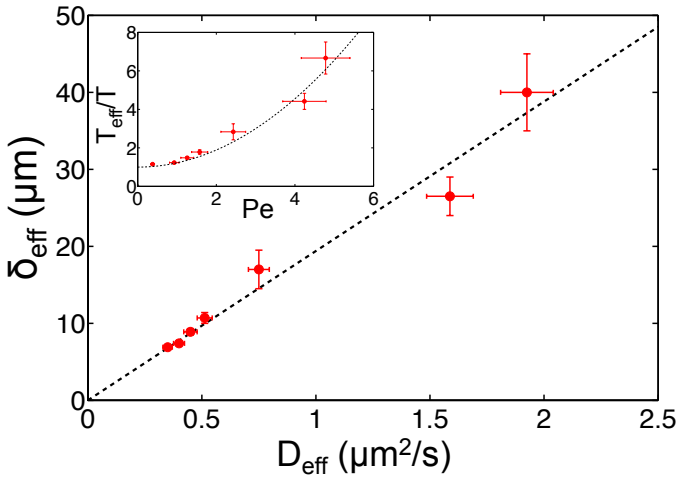

Figure 3.12: **Sedimentation length δ_{eff} as a function of effective diffusion** D_{eff} extracted from figures 3.8 and 3.11 respectively. The dashed line is a linear fit, $\delta_{\text{eff}} = \alpha \times D_{\text{eff}}$ as expected from equation 3.15. The measured slope α =19.5±2.0 μm^{-1}.s is furthermore in good agreement with the expected value $\alpha = 1/v_T = \delta_0/D_0 = 16.2 \pm 2.5\,\mu\text{m}^{-1}$.s, with δ_0 and D_0 measured independently in the absence of injected H_2O_2. *(Inset)* **Plot of the effective temperature** normalized to the ambient temperature T_{eff}/T versus the motility Peclet number of the active colloids, $Pe \equiv V.R/D_0$. The dashed line is the theoretical expectation (see Eq-3.16).

furthermore found to agree with its expected value in equation 3.15. This effectively connects the micro-dynamics of the active colloids to their global stationary profile.
Additionally, the equation 3.15 can be interpreted as a fluctuation dissipation measurement of the effective temperature of the system [136], here defined as $k_B T_{\text{eff}} = D_{\text{eff}}/\mu = \delta_{\text{eff}} \times mg$. Depending on the swimming activity and propulsion velocity, effective temperatures for this active system are found to range between the ambient temperature, for suspension close to equilibrium and "slow" swimmers, up to 10^3K. The effective temperature T_{eff} can be related to a Peclet number $Pe = V.R/D_0$ which characterizes the activity of the swimmer with respect to its equilibrium diffusion:

$$k_B T_{\text{eff}} = k_B T \times \left(1 + \frac{2}{9} Pe^2\right) \qquad (3.16)$$

using $D_{\text{eff}} = D_0 + V^2 \tau_r/6$ (Eq- 3.9) and a re-expression of the rotational diffusion time $\tau_r = 4R^2/3D_0$ in Eq- 3.15. The expression Eq- 3.16 for the effective temperature presents very good agreement with experimental results (see Fig. 3.12-inset). This underlines the role of the Peclet number as the physical relevant parameter of active systems in line with recent predictions [137].

Number fluctuations

Finally, we measured in the previous experiments the mean squared number of particles $\Delta N^2(z)$ in each slide δz for various altitudes z. We plot in figure 3.13 $\Delta N^2(z)$ versus the averaged number $N(z)$ for all fuel concentrations and swimming activity.

Data are found to collapse onto a master curve $\Delta N^2(z) = \kappa N$ with $\kappa = 1$. One can easily derive from equilibrium statistical physics the mean squared of the number fluctuations for a system at equilibrium at temperature T [13]:

$$\Delta N^2(z) = \frac{N^2 k_b T}{V^2(-\partial P/\partial V)_{T,N}} = k_B T \rho \chi_T N$$

where ρ is the concentration of the considered species and χ_T the isothermal compressibility of the fluid. For a perfect gas, $\chi_T = 1/P$ where P denotes the pressure, and the mean squared number reduce to $\Delta N^2(z) = N$. As a consequence our experimental measurements show that under the present semi-dilute conditions, the active suspension behaves like an ideal solution at equilibrium or in other terms a perfect gas of colloids and does not exhibit anomalously large fluctuations ($\Delta N^2(z) \sim N^\gamma$, with $\gamma > 1$) as previously predicted in [86] or experimentally reported in [138, 139], however for much denser active *granular* systems (see chapter 4 for deeper developments on anomalous fluctuations in active systems).

Sedimentation of active suspension

Finally, in the dilute regime under investigation, swimmers behave as a **perfect gas of "hot" colloids** with an effective temperature much larger than the bath temperature. Such behavior was recently predicted in "run and tumble" model of particles under external fields in a regime where the swimming speed V is larger than the sedimentation velocity v_T and is thus validated by our experimental results [91].

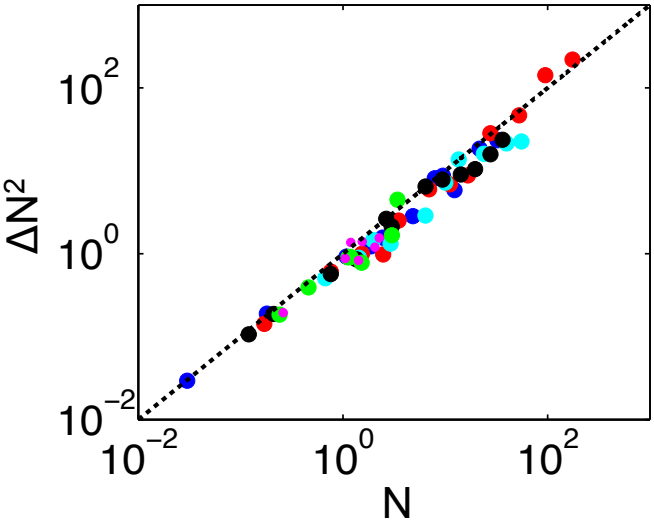

Figure 3.13: **Number fluctuations.** Mean squared number of colloids in each slice ΔN^2 versus the averaged number N for various swimming activity. The symbols colors refer to the the different swimming activity depicted on figure 3.11. The dashed line is the prediction for equilibrium system $\Delta N^2 = \kappa \cdot N$, with $\kappa = 1$ for dilute systems.

The big picture

In this chapter, I investigated the non-equilibrium steady state of an active colloidal suspensions under gravity field. This required the synthesis of large number of Janus colloids and the use of a dedicated microfluidic device, made of permeable gel microstructures. The active particles are chemically powered colloids showing self-propulsion in the presence of added fuel, here hydrogen peroxide. I studied the microdynamics of individual colloids and the global stationary state of the suspension under gravity with optical microscopy. I demonstrated that in the present *semi-dilute* regime, the active suspension followed a fluctuation-dissipation relationship with a temperature T_{eff} directly related to the Peclet number of the colloids activity $Pe \equiv V \cdot R/D_0$. Moreover, I measured *normal* number fluctuations $\Delta N^2 \propto N$. It is the first direct measurement of the effective temperature of an active suspension.

3.5 Appendices

Appendix A: synthesis of Janus microswimmers

The following Janus synthesis can be performed with any type of colloids. Nevertheless experimental parameters (dilution rate ....) can depend on the materials and coating that are used. I will extensively describe the case of 1 μm latex colloids that I mainly used during my thesis. A sketch of the synthesis process from deposition of commercial colloids to resuspension is presented in figure. 3.14a.

Colloid deposition
A commercial solution of latex-carboxylated coated fluorescent colloids (1 μm diameter, Molecular Probes F8823) is diluted 200 times in isopropanol[11](99.99%, Roth) and sonicated for typically 1 h to break aggregates of colloids. We check that despite the apolar nature of the solvent, the colloidal solution remains stable for a few hours.A 1 ml of this solution is deposited on the *rough* side of a 4" silicon wafer (Epitaxial wafer, thickness 525 μm, Si-Mat) under laminar flow. The wafer is straightened to drain the excess of solvent and the air flow is increased to 70% of the maximum speed to finish evaporating. Thanks to its high roughness (typically hundreds of μm) the silicon surface presents large hysteresis and traps the contact line during

[11]We dilute in isopropanol rather than in water for its much higher volatility.

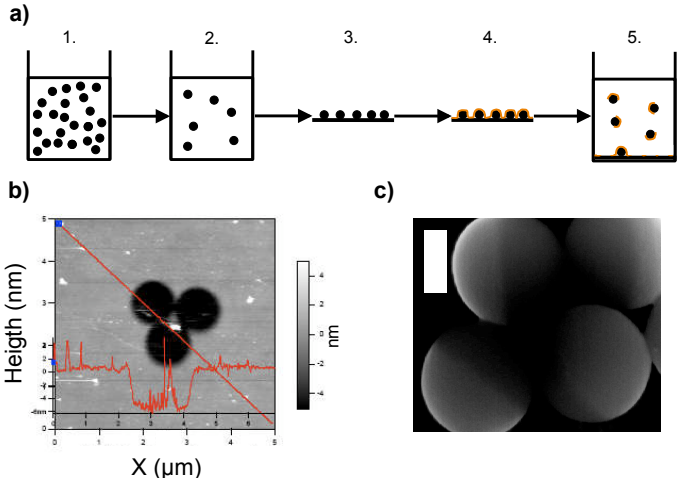

Figure 3.14: *(a)* **Sketch of the protocol to obtain platinum Janus particles.** See text.*(b)* **AFM Picture of the glass slide after resuspension of the Janus particles.** In this experiment, 1 μm colloid were deposited on a glass slide and coated by 5 nm of platinun, thickness determined by a quartz balance during the deposition. An AFM scan on the sonicated glass slide is performed in contact mode. It is coated by a layer of platinum except on the shadow of a *triplet* of colloids for which the AFM measures an altitude of 5 nm. This measures allows to validate the values given by the quartz balance during the deposition step as well as to show that the shadow effect presumed for the realization of Janus particles succeeds. The red graph represents the topography along the red line on the AFM scan. Grateful acknowledgments to A. Piednoir *(c)* **SEM picture of synthesized** Janus, platinum-latex, colloids (scale bar 500nm). The platinum side appears bright on the picture. Grateful acknowledgments to J.M. Benoit.

the drainage of the alcohol film. The evaporation of the solvent thin film is fast enough to ensure an homogeneous depositing of the colloids. The colloids are deposited as individuals on a monolayer. This monolayer is far from dense but it is crucial to have a surface without any packs or stuck colloids for the platinum deposition step of the process. Such a quality of deposition cannot be reached with aqueous solutions of colloids as the film destabilizes in droplets due to the Rayleigh-Plateau instability. These droplets evaporates and the flow causes ring stains [55] and colloidal clusters incompatible with the proper synthesis of Janus particles.

Platinum coating
The wafer is coated with a layer of platinum (purity 4N 99.99%) by sputtering (Evaporator EB3, Edwards, M. Gregoire, NanoLyon). Four 4" wafers can be sputtered at the same time with therefore the "exact" same coating of platinum. This thickness of the layer is determined by a quartz balance of frequency 6 Mhz, during the sputtering. The standard coating is 2 nm of platinum, but to 5 nm coating were also synthesized. The thickness e of the layer is also checked *a posteriori* with an AFM (Asylum) in contact mode (see Fig. 3.14-b) measuring the step between a bare side and a coated size on a flat surface of silicon[12]. The colloids are coated by platinum only on the top hemisphere by

[12]Note that $e < 2$ nm could not be measured with AFM while the separation is visible with the eye by difference of reflectivity between the two regions. The bare-platinum step convoluted with the AFM tip is finally smothered by the drift of the AFM during the scan which forbids any reliable measurement in this low-thickness regime

shadowing, and are namely Janus colloids (see Fig. 3.14-c)[13].

Resuspension of the colloids
The particles are resuspended by sonication in ultra-pure water (Milli-Q, resistivity 18.2 MOhm.cm^{-1}). Each wafer is sonicated $30'$ and rinsed to retrieve every colloids. With 4 wafers, the colloidal solution is typically 40 ml. This solution is centrifugated at 10^4 g during 15 mins (2-16K, Sigma) and the top of the solution is carefully removed to avoid resuspension of the colloids. The bottom of the centrifugating tube is vortexed at maximum speed during 5 mins and sonicated during only $2-3$ mins to avoid damaging the platinum cap of the Janus particles. Finally, a concentrated Janus bare-platinum colloids solution of volume $\sim 50\,\mu$l is obtained with a volume fraction of $\Phi \sim 0.01-0.1\,\%$. This stock solution is stored at 6°C until subsequent use in an airtight tube[14].

Comments on the synthesis technique
This synthesis process is inspired by the "recipe" reported in [108] but adapted to make much large numbers of identical swimmers. All the process is performed under laminar flow or clean-room conditions, to strongly decrease the pollution of the

[13]Taking into account the cross section of the particles, the thickness is non uniform and $e(\theta) = e\cos(\theta - \frac{\pi}{2})$.

[14]If the tube is not very well sealed, the water fully evaporates and packings of colloids form in detriment of the colloidal suspension quality. Distilled water can be added and strong sonication performed to disintegrate aggregates of colloids but this process can damage the platinum cap and is therefore avoided as much as replaced by vortexation.

final solution by micron-size dust.
In addition, as we want to explore the collective dynamics of large assembly of swimmers we need to synthesize these particles at "large scale". The use of "4" wafers rather than glass coverslips strongly increase the surface of deposition. The roughness and contact line trapping of the colloidal isopropanol solution allows to strongly increase the density of particles deposition which of course affects the efficiency of the synthesis.

Appendix B: Janus colloids in a gel microchamber

We deviced a gel microfluidic system in order to unlock the experimental difficulties related to the use of large populations of swimmers. The experimental details to design the microfluidics masks and to mold agarose stamps (5% w/w agarose gel) are described in the previous chapter, section 2.7.
As pinpointed in the *synthesis of Janus microswimmers*, a concentrated sample of Janus colloids is typically $50\,\mu$l. In order to minimize dispersion (like platinum thickness dispersion for colloids not obtained on the same platinum sputtering which strongly affects the weight and the sedimentation behavior of the colloids), we run series of experiments with Janus of the same "bath". This constraints imposes to limit to a very low amount the use of the Janus solution for each experiment. We now report the experimental protocol.

Preparation of the Janus experimental sample
The $50\,\mu$l stock solution of synthesized platinum-bare Janus colloids is vortexed at maximum speed during $2'$ to homogenize the solution. A sample of $0.5 - 1\,\mu$l is taken with a micropipette and deposited into a $500\,\mu$l centrifugation tube. Depending on the desired concentration of Janus colloids, this sample can be diluted in ultra-pure water (Milli-Q, resistivity 18.2 MOhm.cm^{-1}). This solution is sonicated $3'$ to resuspend colloids and get individual colloids in bulk without damaging the platinum cap. The solution of Janus colloids is then ready for

use.

Janus colloids enclosure in a gel microchamber
Agarose gel has been previously printed with 2 side channels and microfluidic chambers (see section 2.7 in the previous chapter) and stored at 6°C in distilled water. After punching the inlets and outlets for the side channels, the stamp is dried with clean air. This additional step avoids dilution of the Janus solution by the thin layer of water presented on the hydrophilic gel. A $0.5 - 1\,\mu$l drop of the solution is deposited on a clean glass cover slip. Then after ensuring that the drop is enclosed in the microfluidic chamber of volume $V \sim 30\,\text{nl} \ll 0.5\,\mu$l, the microfluidic device is tightly sealed as described in section 2.7. This protocol necessitates only the use of a very little volume of Janus particles and avoids dead volumes that would be inherent to standard microfluidic tubing and syringes.

Benchmark of the gel system

While unlocking main experimental difficulties to handle large population of swimmers, the hydrogel technology presents specificities. H_2O_2 diffuses from the side channels till the microfluidic chamber through the gel walls. After a few days soaked in hydrogen peroxide, a gel stamp initially elastic gets brittle. As H_2O_2 is a very strong oxydizing chemical species [15] it certainly reacts with the gel molecules of the system.

In order to quantify the consequences of this aging process,

[15] which originates its use in the laundering!

we ran benchmarks experiments *at equilibrium, i.e* bare colloids in hydrogen peroxide or Janus particles in water. We measure the MSD with the same but non-Janus 1 μm latex colloids in microfluidic gel chambers or glass capillaries for various conditions and concentrations of injected H_2O_2. In each case, the colloids present standard diffusion (ΔL^2 linear in time) as expected for equilibrium experiments. For measurements in 2 dimensions, the slope is 4D and one can therefore extract the diffusion coefficient D of the particle in the medium. Benchmarks experiments show a dependence of the diffusivity with the experimental conditions summarized in figure 3.10-b.

1. For colloids in water, just enclosed in a glass capillary or a gel chamber, we measure a diffusion coefficient $D_{SE} = k_B T/6\pi\eta R = 0.42 \pm 0.02\,\mu\text{m}^2/\text{s}$. This is in agreement with Stokes-Einstein expectations for $R = 0.55 \pm 0.02\mu$m colloids in water. The experiments are performed at 25°C, $\eta(25°\text{C}) = 0.890\,\text{mPa.s}$ and the radius of the colloids is extracted from the certificate of analysis of the lot (F8823, lot 21681W, Molecular Probes) and measured by the manufacturer through dynamic light scattering experiments.

2. Then, hydrogen peroxide is injected in side channels. The measurements of the mean squared displacement are performed for various concentration of H_2O_2 or water and times. In each case, the bare colloids present a diffusive dynamics with a diffusion coefficient $D_0 = 0.34 \pm 0.02\,\mu\text{m}^2/\text{s}$ stable through the various tests, independent of the hydrogen peroxide concentration. In addition, even

if water is injected after a flow of H_2O_2, the diffusion of the colloids remains constant at D_0. The independence with H_2O_2 concentration and the memory of previous hydrogen peroxide flow show that the difference measured between D_{se} is not related to an intrinsic difference of viscosity between H_2O_2 and water as expected for aqueous solutions of hydrogen peroxide of concentration below 10%. Moreover, the same value is also measured for experiments with Janus particles in water after various flows of H_2O_2 solutions are injected in side channels. We infer that the change of the diffusion coefficient of the colloids following the contact of the gel device with H_2O_2 is related to the dissolution of gel polymers in water. The dispersion of polymers in water leads to an increase of the viscosity $\eta \propto n^5$ in the semi-dilute regime where n stands for the volume number density of monomers [140]. A very small dissolution of gel monomers can lead to significant modifications of the viscosity and a subsequent decrease of the diffusivity of tracers. Nevertheless, we did not try to elude the mechanism by which this increase of viscosity is reached.

3. Beyond 2 days in contact with hydrogen peroxide (injected by the side channels or stored in H_2O_2) we measure $D_> \sim 0.4\,\mu\text{m}^2/\text{s}$ but the gel appears macroscopically damaged. Initially elastic, the agarose gel becomes brittle and breaks once manipulated. Degradation of hydrogels by hydrogen peroxide has been already reported in literature for different gels [141, 142]. Consequently we do not

perform exhaustive measurements in this regime as the matrix clearly appears irreversibly modified. All our experiments are performed for maximum 36 h on the same gel device. Then a new gel with new colloids swimmers (from the same synthesis lot of Janus particles) is used.

Finally, we rely on the fact that after a few hours in contact with hydrogen peroxide, the diffusivity of the colloids reaches a plateau $D_0 = 0.34 \pm 0.02\,\mu\mathrm{m}^2/\mathrm{s}$ and remains stable up to 36 hours. In the following experiments, we will inject H_2O_2 for a few hours before the measurements of the MSD to attain the "steady" viscosity D_0. This value is taken as the equilibrium value of the diffusion coefficient of $1\,\mu$m Janus colloids enclosed in gel microfluidic device.

Additionally, we want to underline a complex coupling between the gel walls of width e and the H_2O_2 concentration. The interaction between the two species consumes part of the H_2O_2 fuel. The residence time spent by the hydrogen peroxide in the gels walls before reaching the microfluidic chamber is a crucial parameter to determine the concentration C_0' in the chamber. Assuming a first order kinetics with a kinetic constant k for the reaction between peroxide and agarose gel one has : $d[H_2O_2]/dt = -k[H_2O_2]$. One can therefore relate the concentration C_0' in the microfluidic chamber with the concentration C_0 imposed by side channels by $C_0' = C_0 e^{-k\tau}$ with τ the residence time in the gel walls. This time is given by the diffusive transport of H_2O_2 through the gel wall of thichness e :

$\tau \sim e^2/D_{H_2O_2}$ where $D_{H_2O_2}$ is the diffusion coefficient of hydrogen peroxide. Initially we performed measurements with gel walls of thickness $e = 250\,\mu$m and varying C_0 from 0 to 18% we always measured low velocity and activity of the swimmers *e.g* the maximum velocity of the swimmers in this configuration was $\sim 0.5\,\mu$m/s pointing a concentration C_0' in the chamber of $1 - 2\%$ following [108]. We then used microfluidic designs with gel walls width $e = 125\,\mu$m to reduce by a factor of 4 the residence time. We could therefore access much higher Janus activity and velocity up to $2.9\,\mu$m/s (for $C_0 = 7.5\%$) meaning an increase of the hydrogen peroxide concentration C_0' experienced by the Janus colloids. These results support the basic explanation of degradation of H_2O_2 during the residence of the walls. In order to limit the influence of the gel walls, while keeping a good mechanical reliability of the microfluidic chamber we handle gel stamps with walls of width $e = 125\,\mu$m.

Appendix C: microswimmers dynamics, theoretical expectations

We now propose to calculate the mean squared displacement of a swimming particle.
The swimmer obeys the Newton's equation

$$\frac{d\mathbf{r}}{dt} = V\hat{\mathbf{u}}(t) + \frac{\tilde{\mathbf{f}}(t)}{m} \tag{3.17}$$

with V the swimming velocity along the (fluctuating) direction $\hat{\mathbf{u}}(t)$, m the mass of the particle, and $\tilde{\mathbf{f}}(t)$ the random force associated with the classical Brownian motion [13]. By linearity of the equation, one may separate the motion as $\mathbf{r} = \mathbf{r}_s + \mathbf{r}_B$, with $d\mathbf{r}_s/dt = V\hat{\mathbf{u}}(t)$ and $d\mathbf{r}_B/dt = \tilde{f}(t)$. This separates the component of the velocity of the particle induced by respectively the velocity V or the random force exerted by the medium. The consequence of the Brownian force on the mean squared displacement is well known and is related to the equilibrium thermodynamics diffusion coefficient D_0 by the fluctuation-dissipation theorem [13]. One has therefore $\langle(\mathbf{r}(t) - \mathbf{r}(0))^2\rangle = \langle(\mathbf{r}_s(t) - \mathbf{r}_s(0))^2\rangle + 3dD_0t$ where $\langle\cdot\rangle$ denotes an ensemble average and d is the dimension of the space.
We thus focus on $\mathbf{r}_s$. One may develop the mean squared displacement of the particle

$$\langle(\mathbf{r}_s(t) - \mathbf{r}_s(0)\rangle^2 = V^2 \int_0^t dt' \int_0^t dt'' \, \langle\hat{\mathbf{u}}(t') \cdot \hat{\mathbf{u}}(t'')\rangle$$

which can be rewritten

$$\langle(\mathbf{r}_s(t) - \mathbf{r}_s(0)\rangle^2 = V^2 \int_0^t ds\,(t-s)C(s) \qquad (3.18)$$

with $C(s) = \langle \hat{\mathbf{u}}(s) \cdot \hat{\mathbf{u}}(0)\rangle$.
The next step is to compute this correlation function. The particle undergoes a rotational Brownian motion, and the distribution $P(\hat{\mathbf{u}}, t)$ obeys the rotational diffusion equation:

$$\partial_t P(u,t) = D_r\, \Delta_{\theta,\phi} P(u,t)$$

where $\Delta_{\theta,\phi} = \hat{L}^2$ is the rotational Laplacian operator (also defined in terms of $\hat{L}$, the angular momentum operator).
The solution to this equation with initial condition $P(\hat{\mathbf{u}}, t = 0) = \delta(\hat{\mathbf{u}} - \hat{\mathbf{u}}_0)$ takes the form:

$$G(\hat{\mathbf{u}}, t|\hat{\mathbf{u}}_0) = \sum_{\ell,m} Y_{\ell,m}(\hat{\mathbf{u}})\, Y_{\ell,m}(\hat{\mathbf{u}}_0)\, \exp[-\ell(\ell+1)t/\tau_r]$$

($\tau_r = 1/D_r$), so that the complete solution is

$$P(\hat{\mathbf{u}}, t) = \int d\hat{\mathbf{u}}_0\, P_0(\hat{\mathbf{u}}_0) \times G(\hat{\mathbf{u}}, t|\hat{\mathbf{u}}_0)$$

with $P_0(\hat{\mathbf{u}}_0)$ the initial distribution.
Finally we can deduce the correlation function

$$C(t) = \int d\hat{\mathbf{u}}_0 \int d\hat{\mathbf{u}}\; P_0(\hat{\mathbf{u}}_0) \times G(\hat{\mathbf{u}}, t|\hat{\mathbf{u}}_0)\, \hat{\mathbf{u}} \cdot \hat{\mathbf{u}}_0$$

$$C(t) = \sum_{\ell,m} \int d\hat{\mathbf{u}}\ P_0(\hat{\mathbf{u}}_0) \times \hat{\mathbf{u}} \cdot \hat{\mathbf{u}}_0\, Y_{\ell,m}(\hat{\mathbf{u}})\, Y_{\ell,m}(\hat{\mathbf{u}}_0)\, e^{-\frac{\ell(\ell+1)}{\tau_r} t}$$

The three directions in space are independent and equivalent. We arbitrary focus on the component along z and will multiply the result by 3 to account for the two others equivalent directions. In this sum, only the terms $m = 0$ contribute; furthermore, $\int d\hat{\mathbf{u}}\, \hat{\mathbf{u}}\, Y_{\ell,m}(\hat{\mathbf{u}}) = 0$ for $\ell \neq 1$.
We derive the expression (multiplying by 3 to take into account the three directions of the space) :

$$\begin{aligned} C(t) = \quad & 3 \times e^{-2\frac{t}{\tau_r}} \times 2\pi \int d\theta_0 \sin\theta_0 \cos\theta_0\, P_0(\hat{\mathbf{u}}_0)\, Y_{1,0}(\theta_0) \\ & \times 2\pi \int d\theta \sin\theta \cos\theta\, Y_{1,0}(\theta) \end{aligned}$$

Using $P(\hat{\mathbf{u}}_0) = 1/4\pi$, and $\int d\theta \sin\theta \cos\theta\, Y_{1,0}(\theta) = 1/\sqrt{3\pi}$, we obtain the simple expression

$$C(t) = \exp[-2t/\tau_r]$$

Putting this result into Eq. (3.18), we obtain

$$\langle (\mathbf{r}_s(t) - \mathbf{r}_s(0))^2 \rangle = \frac{1}{2} V^2 \tau_r^2 \left[\frac{2t}{\tau_r} + \exp[-2t/\tau_r] - 1 \right]$$

For $2D$ measurements of the mean squared displacement as we perform by microscopy observations, we have to take into account only 2 directions. Assuming independence and equivalence of the 3 directions of space, the previous prediction must

be multiplied by $\frac{2}{3}$. Adding the Brownian component of the mean squared displacement, we obtain the final formula for a measured mean squared displacement:

$$\langle(\mathbf{r}_s(t) - \mathbf{r}_s(0)\rangle^2 = 4D_0t + \frac{1}{3}V^2\tau_r^2\left[\frac{2t}{\tau_r} + \exp[-2t/\tau_r] - 1\right] \tag{3.19}$$

Appendix D: sedimentation, experimental benchmarks

In order to probe the validity of a fluctuation-dissipation relationship with a suspension of active colloids, we measure the density profiles of the colloids in a microfluidic chamber. In this section, we perform experiments at equilibrium in order to calibrate and validate our experimental setup.
We want to measure the density profile $\rho(z)$ of a dilute solution of colloids ($\Phi \sim 0.01\%$) in water, at equilibrium at temperature T. We use the same commercial colloids (F8823, lot 21681W, Molecular Probes) as used to synthesize the Janus particles. The solution is enclosed in a gel microfluidic chamber as described in Appendix B. The system is left at rest during 4 hours to reach the steady diffusion coefficient.

Counting colloids
After this time we perform z stacks by scanning the chamber with a piezo (see section 3.4). We want to count the number of colloids "close to the focus" on each frame and sum the results for a given altitude z. This way we can measure the colloids distribution along the z direction. For now the expression "close to the focus" is willingly a blurry concept that we must define more quantitatively. The fluorescent intensity profile $\mathrm{I}(z)$ of the maximum intensity is measured to determine accurately the distance of a colloid to the focus plane. We measure experimentally the fluorescent intensity $\mathrm{I}(z)$ of an adsorbed colloid on a glass slide with a water immersion high numerical aperture objective (N.A.

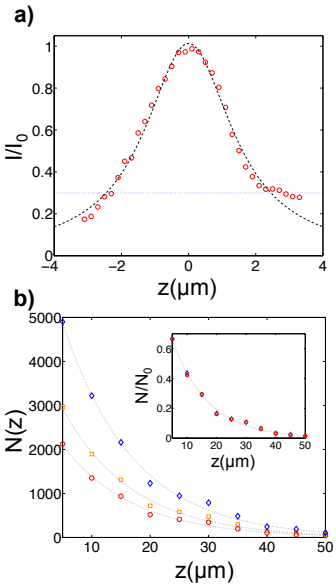

Figure 3.15: *(a)* z **profile of fluorescence intensity of a colloid** (red symbols). A fluorescent colloid is adsorbed on a glass slide. A piezo scans the fluorescent intensity of the brightest pixel along z by steps of 200 nm. The fluorescence intensity I(z) is well fitted by a gaussian function (black dashed line). *(b)* **Equilibrium sedimentation profiles.** Steady density profiles of colloids measured for sedimentation experiments of latex colloids at equilibrium in water. The different symbols represent the density profiles extracted from stacks of images for various thresholds: $0.3I_{foc}$ ($\diamond$), $0.5I_{foc}$ () and $0.6I_{foc}$ ($\circ$). For each case the profile is exponential (dashed line) and the exponential decay does not depend on the threshold criterion $b_0 = 12.1 \pm 1\mu$m. *Inset* **Normalized density profiles** all collapse to the same exponential curve in good agreement with the theoretical value. This benchmark experiment fully validates the experimental setup.

1.2). The normalized intensity is depicted in figure 3.15-a. The intensity is well fitted by a Gaussian. This curve calibrates the relationship between the threshold criterion (in percentage of the intensity in the focus plane I_{foc}) and δ. Applying a threshold criterion we can suppress on each frames the colloids that are at a distance beyond δ of the focus plane and count the colloids present in the slice $\pm\delta$. Practically, a high threshold eases the determination of "in focus" colloids but diminishes the statistics of particles detected on each frame. To get sufficient number of particles and good statistical convergence we define slices of thickness $\pm 2\,\mu$m. This implies a threshold criterion determined by $0.3 I_{foc}$. Moreover, the determination of δ also impacts the acquisition time T_{acq} between frames. To perform a proper ensemble average, T_{acq} must be large enough to enable a colloid to diffuse into or out of the slice. This gives $T_{acq} \geq \delta^2/2D \sim 3\,$s with D the diffusion coefficient of the colloids (typically $1\,\mu\text{m}^2/\text{s}$ for an active colloid) and supports the acquisition frame rate used of $0.2 - 0.3\,$Hz.

Tribute to Jean Perrin

Finally, we measure the density profile of latex colloids in water. The results are presented in figure 3.15-b. The distribution of colloid is *(i)* steady, *(ii)* exponential with *(iii)* an exponential decay over a characteristic length $b_0 = 12 \pm 1\,\mu$m. This value is in full agreement with Jean Perrin expectations for equilibrium. Indeed, for latex colloids (density d=1.055) with radius $R = 0.55 \pm 0.02\,\mu$m at ambient temperature, one expects a sedimentation length given by Eq-3.13: $\tilde{b}_0 = 10.9 \pm 1.2\,\mu$m. This result fully validates our experimental setup. Moreover we checked

that varying the threshold criterion only affects the number of detected colloids but not the exponential behavior and the decay length b_0. In the figure 3.15-b, density profiles of colloids are represented from the same experiments and extracted for various threshold criterions: $0.3; 0.5$ and $0.6\mathrm{I}_{foc}$. We verify that for each case the distribution is exponential with the same exponential decay b_0 (see Fig. 3.15-inset) and that only ρ_0 is affected which finishes to validate our experimental canvass.

Quand y en a un, ça va, c'est quand y en a beaucoup que ca pose probleme[1].

B. Hortefeux, Sep. 2009

4

Towards collective behaviors

The results depicted in the previous chapter on dilute assembly of Janus microswimmers are *equilibrium-like* and properly described in the framework of a Fluctuation-Dissipation relationship. In this context, they do not demonstrate important breakdown of equilibrium physics –certainly related to the dilute concentration of swimmer– but are a key first step to address more complex behaviors of active matter. Indeed collective motion can be observed at almost every scale in nature, from the familiar human crowds, bird flocks and fish schools to microorganisms such bacteria, or cells and until nanometric level with the dynamics of actin and tubulin filaments and the synchronization of molecular motors. Whereas biologists tend to build detailed representations of a particular case, the ubiquity of the phenomenon suggests underlying universal features and thus gives weight to the bottom-up modeling approach favored

[1] Unfortunately it did not refer to the complexity of large systems.

by physicist. It is thus natural for a condensed matter physicist to regard a coherently moving phase as an orientationally moving phase. This motivated a huge amount of work to understand this broad class of non-equilibrium dynamical systems.

Aim of this chapter

In this fourth and last chapter, I will present a brief review of the –huge– literature on collective effects, *designed for experimentalists*. The theoretical predictions in this field are abounding but scattered which makes the classification of *real* systems a bit awkward. This impression in magnified by the scarcity of experimental results to validate the numerous theoretical models. The aim is thus to point relevant, and *experimentally accessible*, observables and signatures related to the "out-of-equilibriumness" of active systems. In this scope, I will report theoretical predictions as well as experimental demonstrations of these effects.
The main purpose is to open perspectives and offer guidelines for further experimental studies of active systems. As I began exploring collective behavior of active colloids only at the end of my PhD, I will report here only very preliminary experimental results with dense suspensions of the Janus diffusio-phoretic microswimmers I have previously studied in the semi-dilute regime (see chapter 3). Encouraging experimental hints underline the relevance of this system in the study of collective behaviors.

Organization of the discussion

In a first part of this section I will describe the theoretical results on the collective and phase behaviors of flocks, *i.e.* assemblies of self-propelled particles (SPP) with velocity v_0 *without solvent*. The situation of SPP flocks without solvent may appear as unconnected to the situation of active Janus suspensions for which the solvent and hydrodynamic interactions play a crucial role. I will nevertheless review this class of SPP as they are some of the major "toy-models" in the study of active systems. In this respect, they are a pleasant avenue to begin in the complex world of collective behaviors and see some of the various signatures of "out-of-equilibriumness": giant number fluctuations, emergence of 2D long range order ...

In a second part, I will describe the physics of *swimming microorganisms*, *i.e.* self propelled particles in a *fluid medium*: the solvent which imposes momentum conservation. This additional conservation law leads to different characteristics than described in the first part and underline the role of hydrodynamic interactions. I will report theoretical predictions in these systems and experimental hints to probe active suspension.

In this context, further perspectives and preliminary experimental results on dense suspensions of the Janus diffusio-phoretic microswimmers I have previously studied in the semi-dilute regime (see chapter 3) will be discussed.

4.1 Preamble on active systems

As previously mentioned, active matter is condensed matter in a fundamentally new non-equilibrium regime. To support this idea we underline specificities of these systems:

1. The energy input takes place directly at the scale of each active particle and is thus "homogeneously" distributed in bulk, in clear contrast with out-of-equilibrium systems for which the energy is injected by a boundary forcing, *e.g.* sheared fluids.

2. The direction of the self-propelled motion is set by the particles themselves (and possible couplings with the surrounding world) but no symmetry-breaking is imposed by an external field.

Actually these characteristics can even be used to define active matter. The purpose of the physicist is thus to give a comprehensible framework for the description of such systems and give a proper scenario to describe how interactions typically at the particle range can lead to the emergence of long range order.
We turn to the description of out-of-equilibrium signatures and phase transitions of assembly of SPP. We will notably underline the differences arising from the different classes of system: SPP *without* or *with* surrounding fluid medium and categories of propellers (polar/apolar for flocks and pushers/pullers for active suspensions). As a first step we will consider a "minimal" model of flocking: the *Vicsek's model* [87]. Through this model of *individuals* coupled *via* microscopic interacting rules, it will

be easier to build an intuition on the collective behavior that may arise from a collection of interacting SPP. Such a "microscopic" approach allows to figure out many properties of SPP but does not allow to understand the large scale, long dynamics of a very large, moving flock. Solving the very-many body problem is analytically intractable and moreover *a priori* unnecessary to describe the large scales in the system. This problem is analogous to the field of hydrodynamics where the dynamics of the fluid is properly described by a continuum Navier-Stokes equation rather than the complete dynamics of all the molecular components in the fluid. The "coarse-graining" of observables describes the flock into continuum, smooth fields, *e.g* number density $\rho(\mathbf{r}, t)$ or velocity $\mathbf{v}(\mathbf{r}, t)$. Spatial and temporal symmetries of the considered problem and the definition of phenomenological parameters that "hide" microscopic details, as bulk viscosity η for hydrodynamics, allows to build a proper *continuum evolution equation* of the SPP system. The *hydrodynamic* approach is a very powerful tool to probe various aspects of the physics of active matter:

- Noise and phase transitions. For a general SPP suspension one expects noise sources of different kinds: thermal Brownian motion (negligible for particles larger than a few microns)and intrinsic fluctuations in the "motor" of self-propulsion of individuals SPP. The noise competes with the emergence of long range order and the formation of collective behaviors. We will thus discuss "phase transitions" and emergence of long ranged order in these systems and the sensitivity of the ordered phases to noise,

e.g. what is the order of the transition?

- *Fluctuations.* What are the scaling laws of the fluctuations in such out of equilibrium systems? Do they agree with the central limit theorem as for equilibrium ? We will notably discuss number fluctuations in suspensions of SPP.

4.2 SPP flocks

In this section we will begin by addressing models of ordering of active particles in a surrounding medium treated as an inert substrate or this equivalent without solvent. Each self-propelled particle possesses a velocity vector of fixed magnitude v_0.

Classification of systems

As a first step we will try to classify SPP in a minimal number of classes influencing the collective dynamics of the flock. *Propulsion* The mode of propulsion of the SPP belongs to one of the two following type:

- **polar:** the particles possess a "head" and a "tail" and the direction of the propulsion is thus given by an arrow. This is of course the case of birds, bacteria ...
- **apolar:** the particles are moving in a direction but with indifferent tail or head. Such systems can be experimentally obtained from symmetric rods in a vibrated container: the velocity is given by the long axis of the cylinder but the direction is random.

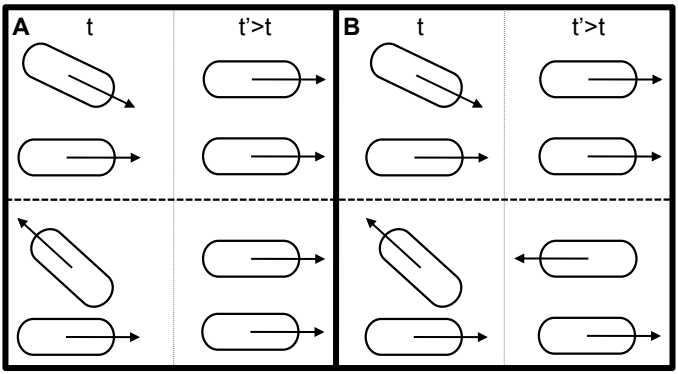

Figure 4.1: **Classifications of interactions between self-propelled particles.** We consider only polar SPP, blacks arrows represent velocity vectors. **A. Ferromagnetic interactions:** aligns the velocity vector of interacting SPP in direction and sense, for any given initial conditions before interaction.
B. Nematic interactions: aligns the velocity vector of interacting SPP. Nevertheless final velocities can be parallel or antiparallel depending on the initial angle between the polar SPP. A simple picture is that nematic interaction tends to align vectors with minimal geometric change in the system.

Interactions
The emergence of collective behaviors relies on the presence of interactions between the particles. Even short range interactions as excluding volume can be sufficient. We classify interactions in the same spirit as the propulsion mode of the SPP, on "geometrical" bases.

- **Ferromagnetic interactions.** Considering two polar SPP interacting, the interaction aligns the directions and senses of the velocity vectors (see Fig.4.1-A). Of course, ferromagnetic interactions do not make sense for apolar SPP!

- **Nematic interactions.** Considering two polar SPP interacting, the interaction aligns the directions and arrows of the velocity vectors if the initial angle between them is below $\pi/2$ and aligns in direction but with opposite sense otherwise (see Fig.4.1-B).

4.2.1 Polar SPP with ferromagnetic interactions: Vicsek's model and further

Ingredients of the model

We begin by the description of a microscopic, *discrete* model of flocking: the Vicsek model [87]. The purpose is to define the minimal ingredients to obtain through numerical simulations collective behaviors of SPP as birds.
The model incorporates the following generic features

1. A large number of **polar** points SPP.

2. Interactions are **ferromagnetic**. Particles move over time attempting to move in the same direction as their neighbors.

3. Interactions are purely short-ranged: each SPP will tend to follow its neighbors within some finite distance[1] R_0, independent of the size of the flock.

4. The model has complete rotational symmetry.

5. The SPP mechanism of "following" is noisy. The only considered noise is on the direction it actually moves adding to the averaged direction of motion a stochastic, short-ranged spatio-temporally correlated noise –while the velocity magnitude is kept constant.

6. The considered model is purely 2D.

Results and discussion

An equilibrium-like XY ferromagnet
First, as first noted by Vicsek himself, this model is exactly the

[1] This may appear as a reasonable assumption for bird flocks but is actually wrong. The constraint on the interactions is not geometric (interaction if the distance between birds is below R_0) but topological in nature (there are interactions between the n neighboring birds even if they are distant from more than R_0) as experimentally unveiled by the Starflag team [100] The topological interaction moreover grants significantly higher cohesion on the aggregation of the flock compared with the metric, geometric one.

dynamical model for a *2D equilibrium ferromagnet* **except for the motion**. If we thus interpret the velocity vectors of the SPP $\mathbf{v}_i$ as spins carried by each "bird" and update the spins according to the given rule for the interaction but do not actually move the birds, the model is a an equilibrium $2D$ ferromagnet which will relax to a Boltzmann distribution for an equilibrium Heisenberg model (with spins on a random set of points rather that on a lattice as usually stated). The Vicsek's model thus shares many analogies with the XY magnet models: it presents a "well defined" phase transition from a disordered phase to a coherent flock with decreased noise or increased particles density. The nature of the order-disorder transition with noise strength is under debate. Originally pointed as a second order transition by Vicsek [87], the transition was revealed to be discontinuous by Gregoire *et al.* by using much larger systems [143]. The critical behavior advocated by Vicsek was then attributed to strong finite size effects.

An out-of-equilibrium signature: emergence of a long range order

A striking difference with ferromagnetic analogy arises from Vicsek's simulations: at large density and low –but non zero– noise, the motion tends to become ordered from disordered on a macroscopic scale and all the particles tend to move in the same spontaneously selected direction (see Fig-4.2). The flocking model thus shows that a true **long range order**, *i.e.* a coherently, moving ferromagnetic flock with a nonzero average velocity $\langle \mathbf{v} \rangle = \frac{1}{N} \sum_i \mathbf{v}_i$, is possible at "nonzero temperature", *i.e.* nonzero noise. This result is in clear disagreement with

the "Mermin-Wagner" theorem of equilibrium statistical mechanics. This theorem states that *(i)* in dimensions $d \leq 2$, *(ii)* at non zero temperature with *(iii)* short-ranged interactions, it is impossible to spontaneously break a continuous symmetry. In the context of the XY spin model, it means that is impossible to develop spontaneously a true long-range ordered state with nonzero magnetization from a disordered state, with zero magnetization. But the ordered state with $\langle \mathbf{v} \rangle \neq 0$ breaks the continuous symmetry of the disordered state, namely rotation invariance! The reason the Mermin-Wagner theorem does not apply to flocks is of course that they are not systems in thermal equilibrium due to the intrinsically non-equilibrium self-propulsion of the particles! The kinetic disordered-ordered phase transition is related to the fact that the particles are driven with a constant absolute velocity and thus unlike standard equilibrium physical systems, with no conservation of the total momentum in the system. Finally, the spontaneous emergence of a moving, ordered phase thus appears as a strong signature of the "out-of-equilibriumness" of the SPP in Vicsek's model.

Further properties of ferromagnetic flocks

The "microscopic" Vicsek model is of great interest in order to figure out the physics at work in the emergence of long ranged order in assemblies of SPPs. As we briefly mentioned in the introduction, such a detailed description is not adapted to the description of the large-scales, long-time dynamics of a large assembly of particles which requires a hydrodynamics formulation.

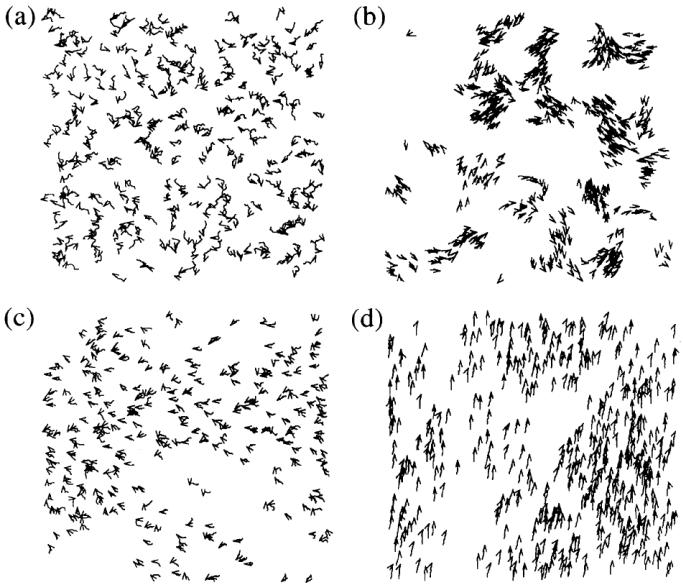

Figure 4.2: **Disordered-ordered phase transition in a system of SPP following Vicsek's model.** The actual velocity is depicted by a black arrow. *(a)* Initial conditions. *(b)* For small densities and noise, the particles form groups moving coherently in random directions–disordered phase. *(c)* At higher density and noise, the particles move randomly but with some correlation–disordered phase. *(d)* For higher density and smaller nonzero noise,long-ranged order emerges and the phase is ordered. Reprint from [87].

We will not describe the way continuum equations of the hydrodynamic model are written-down and derived. Basically, the general principle is that the non-equilibrium conditions oblige to consider all terms in the equations that are not explicitly forbidden by symmetry or conservation laws. The interested reader can report to [144–146] for these aspects. Now, we only report additional –but non exhaustive– insights on the physics of ferromagnetic flocks given by the hydrodynamics formulation that appear as signatures of the non-equilibrium nature of the system and that could be tested experimentally:

- **Long range order in 2D.** Taking into account the non linearities of the hydrodynamics equation, it is shown that 2D long-range order is possible in a ferromagnetic flock as obtained from the Vicsek model

- **Anomalous number fluctuations.** The density field presents anomalous strong fluctuations[2] in the ordered phase. For regions with N particles on average, the root mean square of the fluctuations $\Delta N = \langle (N(t) - N)^2 \rangle^{\frac{1}{2}}$ scales a N^{γ} with $\gamma = 0.8 > 0.5$ [147].

- **Anomalous transverse diffusion in the ferromagnetic phase.** Simulations unveiled an anomalous superdiffusion of individual particles in the direction perpendicular to the flock's moving direction. The dispersion of a 2D ensemble of "boids" is given by $w^2(t) = \langle [y_i(t) - y_i(0)] \rangle \propto t^{\frac{4}{3}}$

[2] As a quick reminder, the root mean square of the fluctuations of an observable $\Delta O \propto O^{\frac{1}{2}}$ in a equilibrium system, given the central limit theorem.

[145]. Note that the diffusion remains anomalous in 3D but the scaling law differs: $w^2(t)\rangle \propto t^{1.7}$ [147].

4.2.2 Polar SPP with nematic interactions

Theoretical predictions

We now turn to large collections of polar SPP with nematic interactions restricted to a two dimension space. This class of SPPs can be practically obtained from anisotropic vibrated rods, thus polar [148,149] interacting through volume exclusion, which is nematic (as figured out by Fig.4.1-B) . This problem was addressed in a mixed Vicsek model by Chate *et al.* [147]. Once again, we report only major and *experimentally accessible* signatures of the non-equilibrium properties that are much more extensively discussed in [131, 150].

- **Nematic ordered phase.** Unlike polar SPP with ferromagnetic interaction, no polar ordered phase is observed in this system. Only nematic order arises in spite of the polar nature of the particles, but it is long-ranged.

- **Phase transitions and anomalous fluctuations.** This system exhibits a much more complex phase transition behavior that in the ferromagnetic case: ordered and disordered regimes, each sub-divided in two phases leading to a total of four phases [150] (see Fig-4.3). Given the particle density, the nematic orientational order is destroyed with increasing noise.

- Phase I: at lowest noise η, presence of a long range nematic order. Two subpopulations of particles migrate in opposite directions constantly exchanging particles (see Fig-4.3-a). *Anomalous number fluctuations* appear in this phase: $\Delta N \propto \langle N \rangle^{0.8}$, as for the ferromagnetic polar order.
- Phase II: at steady state, presence of the low-density disordered region (see Fig-4.3-b,c). The emergence of the density inhomogeneities processes as nucleation and phase separation. The dense regions presents nematic order as for phase I and similar *anomalous fluctuations*.
- Phase III: segregated system with presence of dense bands (see Fig-4.3-d). The bands are unstable and chaotically bend, break and reform. Phase III is a disordered phase with *normal equilibrium-like fluctuations* but huge temporal and spatial correlations.
- Phase IV: highest noise, ordinary, spatially homogeneous disordered phase with very short time and space correlations.

- **Isotropic-nematic transition.** Hydrodynamic description of a system of polar SPP with nematic shows a lowering of the density parameter ρ_{SPP} of the nematic-isotropic transition: $\rho_{SPP} = \rho_E/(1 + \frac{v_0^2}{5k_BT})$, where v_0 is the SPP velocity and ρ_E the equilibrium Onsager transition density [131]

- **Boundary conditions sensibility.** We want to stress a very important role played by boundary conditions in the physics of SPPs. For equilibrium system, the boundary layer typically develops in a scale $\delta \sim \ell$ given by the size ℓ of the particle. With active systems, a finite polarization at the boundary decays as $\delta \sim v_0\tau$, with τ the persistence time in the system. Given L the size of the system, if $L \sim v_0\tau$, the correlations develop on the same scale as the size of the system. This underlines the possible prime role of boundary conditions in such systems as well as possible experimental arctefacts.

- **Clustering transition.** A clustering transition exists for particles with only excluded-volume interaction provided active motion and anisotropic particles (rods). This transition does not exist for isotropic particles (squares) or Brownian equilibrium diffusion [151].

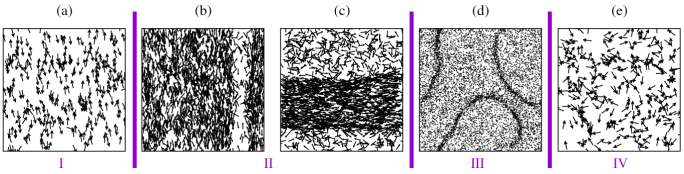

Figure 4.3: **Phases in a system of polar SPPs with nematic interactions for increasing noise** from *(a)* to *(e)*. Arrows indicate the polar orientation of the particles. See text for a description of the phase properties. Reprint from [150]

Experimental realizations

Experiments with large collection polar self-propelled particles were performed by Kudrolli *et al.*. Vibrated anisotropic rods behave as polar particles [149] and interact via volume-excluded *nematic* interactions. For sufficient driving accelerations, they observe dense clustering of self-propelled rods at the boundary. This phenomenon is absent for self-propelled rods which seems in agreement with the theoretical predictions by [151]. The clustering at the wall underlines the predominant role of boundary conditions in these systems. Anomalous number fluctuations are reported: $\Delta N \propto \langle N \rangle^{\frac{7}{12}}$, but with an exponent different from Ginelli *et al.* predictions [150]. Finally, no global polar order is observed in the system but coherent structures appear and the velocity field reveals numbers of streams and swirls with strong random fluctuations.
Recently, Deseigne *et al.* performed experiments with asymmetric, polar, vibrated disks. Interactions are given by hard core repulsion [139]. They observe anomalous number fluctuations $\Delta N \propto \langle N \rangle^{0.72}$ in good agreement with 0.8 exponent theoretically predicted[3]. Finally they report polar collective motion with long-range order –developed on the scale of the system– . The emergence of a polar order is not expected theoretically for polar SPP with nematic alignment (but predicted for polar SPP with ferromagnetic interactions). Actually they observe nematic collisions with systematic ferromagnetic bias. The con-

[3]Note that we define ΔN as the root mean square of the fluctuations in the whole chapter while Deseigne *et al.* used the same notation for the variance of the particles number in [139] thus the square of our notation.

sequences of this additional ingredient has not been considered up to now theoretically and make the classification of the system awkward. This result questions the nature of the of the interactions in this system that would *a priori* be pointed as nematic but nonetheless presents experimental ferromagnetic bias.

We end this section on SPP without solvent with the case of apolar SPP with nematic interactions.

4.2.3 Active nematics

By symmetry, the mean macroscopic velocity of an active nematic flock is zero. One could then imagine that the system presents no distinctive nonequilibrium properties since a phase that is not drifting does not have an order parameter that breaks time-reversal symmetry [146]. This expectation is actually wrong and dynamical processes allowed by the symmetry of the system introduce remarkable statistical behaviors of active nematics.

Giant number fluctuations

The main prediction on the non-equilibrium signature of active nematics is the presence of *giant number fluctuations*, *i.e.* $\Delta N \propto \langle N \rangle$ in strong contrast with equilibrium situations where central limit theorem applies and with an anomalous exponent bigger than with other class of SPP systems. Such fluctuations are named *giant* as they make the density an ill-defined quantity even in the limit of a large system. A physical understanding of the origin on the giant number fluctuations of the system can

be pictured as follows [152]. We consider a 2D system of apolar nematic SPP, with the angle θ as the only parameter to define flock distortions from perfectly aligned state. As presented on Fig.4.4-a, any asymmetry in the flock, splay or bend, confers local polarity and hence local flock motion. The current of particle $\mathbf{J}$ is thus proportional to the angular gradients: $\partial_x\theta, \partial_z\theta$. At steady state, this active flux is balanced by the diffusive current $\mathbf{J}_D \propto \nabla\rho$, ρ density of the flock which makes fluctuations of ρ and θ of same order.
By symmetry, angular θ fluctuations have variance of order $1/q^2$ at wavenumber q and thereafter, number density fluctuations are of $1/q^2$. Integrating over the wavenumber in a 2D space, one finally obtains the number fluctuations.

$$\Delta N \propto \langle N \rangle^{\frac{1}{2}+\frac{1}{d}} \sim \langle N \rangle \text{ with } d = 2, \text{ the space dimension}$$

The giant number fluctuations thus appear as a consequence of the coupled dynamics of density and orientation related to the nematic order in the system. So forth no giant fluctuations are expected in the isotropic phase.

Experiments

Narayan *et al.* realized experimental active nematics with a very dense collection (surface fraction $\Phi \sim 50 - 66\%$) of agitated monolayer of rods on a solid substrate. They measured giant number fluctuations $\Delta N \propto \langle N \rangle$ in a system presenting macroscopic swirls [153] (see Fig.4.4-b) . No giant fluctuations are reported in the isotropic phase. The fluctuations are also extremely long-lived as they report logarithmic relaxation of

the temporal autocorrelation function of the density fluctuations. Both these experimental results agree with theoretical predictions on active nematics [153,154]. *I end up with the brief*

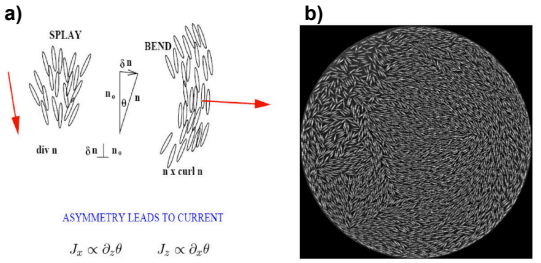

Figure 4.4: **Giant number fluctuations in active nematic.** *(a)* Bend or Splay in an apolar nematic confers local polarity and hence local motion. Reprint from [152]. *(b)* Nematic order with giant density fluctuations in a assembly of active nematic particles. Reprint from [153].

overview of the complex dynamics of self-propelled particles without solvent or, this is equivalent, a p*assive frictionnal medium which only role is to keep the particles at constant velocity. I now add a fluid solvent and consider the collective behaviors of suspended swimmers. The motion of the active particles in the medium is force free and for this class of SPP and additional conservation law is to be accounted: momentum conservation. This arises hydrodynamics interactions which present important modifications in the dynamics.*
We will restrict ourselves in our presentation to the case of the low Reynolds regime e.g. with microorganisms and in Newtonian fluids.

4.3 Low Reynolds number active suspensions

In this section we therefore survey such *suspensions*, ordered or disordered, of active particles in a fluid medium and show how the inclusion of momentum-conserving hydrodynamic flow into the analysis of active particle systems introduces important qualitative departures from the behavior presented in the preceding section. The long-range nature of the hydrodynamic interactions among the active particles leads to large-scale non equilibrium phenomena reported in colonies of bacteria of collections of living cells.

4.3.1 Pushers and Pullers

Low Reynolds microorganisms propel through a variety of periodic, non-reciprocal strokes (as described in section-3.1) that involve complex dynamics of beating parts *e.g.* flagella or cilia. Understanding the collective behaviors of dense suspensions of these systems, given the details of the swimming dynamics of individuals, would appear as a complete nightmare. Here we are interested in the collective behavior of many swimmers on *long time and large length scale* which make the details of the mechanism of self propulsion cumbersome.

Given Newton's third law, the active particles and the fluid exert equal and opposite forces on each other. It imposes that the

force density associated with each swimmer must integrate to zero, *i.e* no monopole moment is allowed. In a far field approximation, the minimal model of a stroke-averaged active particle in a fluid is therefore a static force dipole[4] of strength f, positive or negative, depending on the force exerted on the surrounding fluid:

- **Pullers.** Contractile swimmers with $f < 0$ pull fluid along their axis and push fluid out along an axis normal to their midpoint (see Fig.4.5-A for the fluid flow pattern). They are propelled by flagella at the head of the organism, hence "pullers". The algae *Chlamydomonas* belong to this class.

- **Pushers.** Tensile swimmers with $f > 0$ push fluid along their axis and pull fluid at their midpoint (see Fig.4.5-B for the fluid flow pattern). They are propelled from the rear, hence "pushers". Most bacteria, such as *E. Coli* belong to this class.

Let us precise that using the classification of SPP given in the previous section swimmers are *polar particles*.

The theoretical study of active suspensions is done by constructing the coupled dynamical equations for the swimmer concentrations and orientations and a *generalized* Navier-Stokes equation for the velocity field $\mathbf{u}$ of the suspension. Self-propulsion enters via the force density f in Navier-Stokes equation. The formulation of the hydrodynamic equations and their study goes far

[4]More complex models may encounter higher order multipoles.

beyond the aim of this chapter but are thoroughly developed in [86, 137, 146, 152]. Only most striking consequences on the dynamics or anomalous observables and experimental illustrations will be discussed.

4.3.2 Breaking the second principle

Thanks to the permanent energy input by the active swimmers, the system is *intrinsically* out-of-equilibrium and thus has no reason to be ruled by equilibrium principles as the second principle. Recently, Di Leonardo *et al.* gave numerical evidences of *monothermal* micromotor in a bacterial bath [101]. The chaotic motion of the active particles is rectified by asymmetric environment, *e.g.* ratchets to give net propulsion. This result is in clear contrast with equilibrium baths for which the detailed balance can not be broken. This scenario was validated experimentally by [102, 103]

4.3.3 Instability of orientation-ordered active suspensions

Instability of orientation-ordered active suspensions

Uniform ordered active suspensions are absolutely unstable at long wavelengths because of the growth of orientational fluctuations [86, 152]. An orientational order is under permanent and unstable uniaxial compression (pullers) or tension (pushers). We show the basic mechanism at work for suspensions of pullers (see Fig.4.5-A') or pushers (see Fig.4.5-B'). Let us consider a

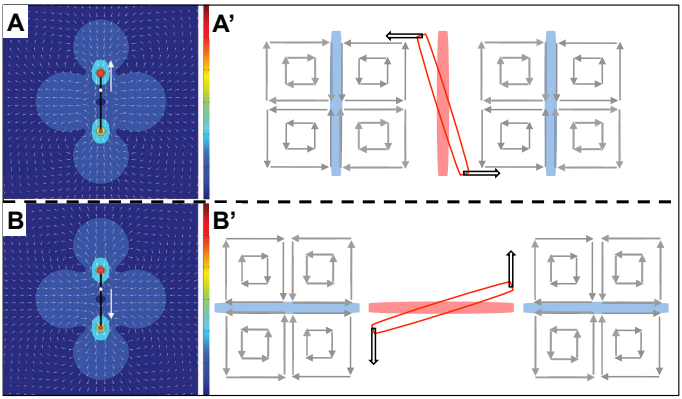

Figure 4.5: *(A-B)* **Dipolar flow pattern induced by the active force exerted on the surrounding fluid by a puller** *(A)* **or a pusher** *(B)*. The arrows represent the direction of the flow, fluid flow velocity denoted by the color. White arrow gives the direction of propulsion. Reprint from [137]. *(A'-B')* **Instability of a polar-ordered suspension of pullers** *(A')* **or pushers** *(B')***.** Let us assume a perfectly ordered, unbounded, parallel collection of pullers *(A')*, respectively pushers *(B')*, (swimmers represented as full colored symbols), *i.e.* a polar-ordered state. The double black arrow shows that any fluctuation of orientation of a swimmer (open red symbol) is amplified by the flow pattern (grey arrows) of the neighboring pullers *(A')* or pushers *(B')* (full blue symbols). Polar state of pullers, respectively, is an unstable state of uniaxial tension, respectively compression.

perfectly ordered, unbounded parallel collection of pullers (respectively pushers) swimmers. The self generated flows cancel in a delicate balance and the polar-state is at equilibrium. The nature of the equilibrium –stable or unstable– is given by the robustness to fluctuations. We suppose an orientation fluctuation of one puller (respectively pusher) in the polar state. The fluctuation is amplified by the flow pattern induced by the neighboring pullers (respectively pushers) and destabilizes the orientational order into an isotropic state (see Fig.4.6-I).
This scenario is in full agreement with the theoretical expression derived by [137] of the torque exerted by a puller (respectively pusher): a puller tends to misalign other swimmers located in the orthogonal direction of its axis, and a pusher tends to misalign swimmers along its axis. This pictorial argument can be detailed by a stability analysis of the hydrodynamics equations of the active suspensions [86]. In the Stokesian limit, Simha *et al* reports a growth of the orientational instability for wavenumbers q such as $Re \ll qa \ll \Phi^{\frac{1}{2}}$, where Re is the Reynolds number on the scale a of the particle, and Φ is the suspension volume fraction. This prediction differs from recent numerical simulations by Saintillan *et al.* who find that suspensions are *always* unstable at finite wavelength [155]. Finally, Baskaran *et al.* underlined the role of the long ranged ($\sim 1/r^2$) nature of the hydrodynamic interactions in this instability [137].

Isotropic suspensions: local nematic-order and mixing

In agreement with previous theoretical predictions, numerical simulations by Saintillan *et al.* exhibit ordered suspensions of

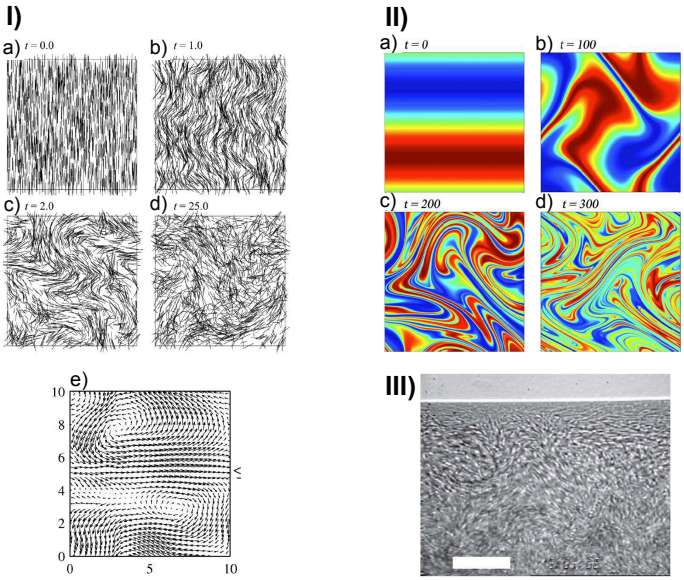

Figure 4.6: *I)* **Destabilization of an orientational order polar state of pushers into an isotropic state.** The isotropic state presents local order with swirls and vortices . (a)-(d) increasing time in numerical simulations: (a) initial polar suspension, (d) final isotropic suspension. Typical flow field of the isotropic suspension is presented on figure e). Reprint from [156]. *II)* **Fluid mixing by an active suspension of pushers.** The figure shows the configuration of a passive scalar field in the suspension (a)-(d) increasing time in numerical simulations: (a) initial polar suspension, (d) final isotropic suspension. Reprint from [155].
III) **Zero reynolds number turbulence** in a drop of *Bacillus subtilis* bacteria (pushers). Reprint from [157].

swimming rod-like particles unstable to long wavelength [156]. Nevertheless they unveil a local nematic ordering at short length scale as a result of hydrodynamic interactions. Very rapidly the orientational order destabilizes into a globally isotropic state characterized by large-scale vortices and swirls (see Fig.4.6-I.e) with large particles concentration fluctuations. Local orientational order, as well as formation of transient aggregates of particles has been also reported for spherical swimmers[5] in [88] with a slow decay of the radial distribution function $g_o(r)$ of the system. These patterns are dynamically unstable and constantly break up and merge in time. This suggests important modifications on the transport properties, *e.g.* mixing, in active suspensions. Saintillan *et al.* report that *efficient convective mixing* takes place in suspensions of pushers (see 4.6-II) but *not* in suspensions of pullers [155]. The mixing originates in the constant breakup and merging of concentrated regions of swimmers. The viscous fluid in which locomotive energy of individuals microswimmers is transferred also carries interactions that drive spatiotemporal coherence. Hydrodynamic couplings has significant impact on the dynamics of the swimming particles. The velocity distribution $P(v)$ presents large discrepancies with the equilibrium gaussian distribution. It is algebric $P(v) \sim 1/v$ at small velocities while the asymptotic decay is consistent with a gaussian [88]. Moreover, Saintillan *et al.* report that pullers swim more slowly than in the isolated case and pushers are

[5] Local orientational order is also reported for symmetric spherical swimmers by [88] but without formation of –even transient– aggregate. Nonetheless, we present this result only as a side remark as symmetric swimmers are rarely encountered in experimental realizations of swimmers.

faster. This effect exists in a wide range of concentrations – from moderate to high– of swimmers and leads to modifications of the swimming velocity of an individual up to $15-30\%$ [156]. Furthermore they report a strong dependence with particles volume fraction of the characteristic time scale τ_r for relaxation of the particle orientation. Because the particles interact and effectively travel through a chaotic flow –which depends on the swimmer volume fraction in the suspension– their orientations actually decorrelate in time.

Experimental observations

Many experimental evidences of "out-of-equilibriumness" of active suspensions were recently reported, but up to now, only with biological microswimmers *e.g.* bacteria or algae. Recent experiments have demonstrated the existence of collective effects for sufficiently concentrated suspensions [157]. The correlation length of the collective motion can exceed the size of the individual cells by more than an order of magnitude and the collective flow speeds (typically 50-100 μm/s) largely exceed the speed of individuals (typically 15-20 $\mu m/s$). Moreover these cooperative effects are demonstrated as strongly related to the concentration of swimmers. No collective effect is observed in dilute suspensions in which the correlation length is limited to the size of a bacterium, *i.e.* an equilibrium-like behavior and Sokolov *et al.* demonstrated a smooth and monotonically increase of the correlation length through the transition from individual to collective behavior [94].

Experiments by Wu *et al.* showed the presence of small

swirls and jets of cooperative swimming in thin films of concentrated suspensions of bacteria *E. Coli* –pushers–. This had important impact on the transport properties of the suspension with greatly enhanced diffusion[6] and even superdiffusion of passive tracers [97]. Exceptional transport of passive species in suspensions of pullers, the algae *Chlamydomonas*, was also recently reported with non-gaussian probability distribution functions of the tracers displacements by [93].

4.3.4 Rheology of active suspensions

As it propels itself, a swimming particle exerts a net force dipole on the surrounding fluid as a balance between the propulsive force exerted by the particle and the viscous drag on its body. The dipole induces a disturbance flow around the particle which results in hydrodynamics interactions, responsible for the complex dynamics we described above. In addition, we also expect that the injection of energy in the system by the active particles modifies the effective rheology of the suspension. Large theoretical efforts have been recently devoted to study these systems, and provided strong support to the idea that a medium suffused with active processes should be thought of as a distinct type of material. It was notably showed consequences on the viscosity, so called *effective viscosity*, of the swimming activity. A basic picture of the connection between bulk viscosity and swimmers activity can be given as follow. We consider an isotropic sus-

[6] The idea of a "bacterial bath" akin to the molecular bath responsible for brownian motion arises from the enhanced diffusion of tracers in suspensions of bacteria

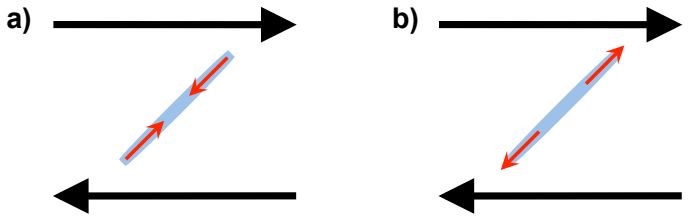

Figure 4.7: **Impact on the viscosity of the propulsion mode of rod-like swimmers** in a isotropic phase of an active suspension. Swimmers align under shear (black arrow) *a)* Contractile pullers particles. The force dipole (red arrow) opposes to the imposed flow, thus leading to an increase of the effective viscosity of the suspension. *b)* Tensile pushers particles. The force dipole (red arrow) enhances the imposed flow, thus leading to an decrease of the effective viscosity of the suspension.

pension of rod-like pullers (respectively pushers). A shear flow is imposed to the system and produces alignment of the swimmers. The permanent force dipole exerted by the contractile pullers (respectively tensile pushers) pulls back and resists to (respectively pushes out and enhances) the flow that oriented them, see Fig.4.7-a (respectively see Fig.4.7-b). This results in a change in the stress/rate ratio w.r.t. the same *equilibrium* suspension with passive particles, *i.e.* higher viscosity for pullers and lower viscosity for pushers. This sketch was first given, and supported by a coarse-grained hydrodynamic approach, by Hatwalne *et al* [158] to show the macroscopic impact on the viscosity of the swimming activity. These predictions are in agreement with a kinetic model of active rods by Saintillan [159]. Nevertheless the scenario of Fig.4.7 relies on the stress alignment of

the swimmers, *i.e.* form anisotropy. Haines *et al.* showed that swimming results in a decrease of viscosity only if the orientation distribution of swimmers is anisotropic, *e.g.* under gravitational field [160] and Ishikawa *et al.* demonstrated viscosity effects in suspensions of active "squirmers" in gravity field [161]. The reduction of effective viscosity intuitively results in the energy injection by the swimmers thus counteracting the energy loss due to viscous dissipation [160]. Saintillan formally identified the active power input generated by swimming particles as the origin for the decrease in viscosity predicted in pusher suspensions [159]. He notably demonstrated that predicted negative viscosity did not violate the positive rate of viscous dissipation, *i.e.* the second principle of thermodynamics, as it then included a contribution which is not of dissipative origin. Furthermore while positive viscosity results in preferential damping of high wavenumbers, low wave numbers are destabilized by negative viscosity, thus saturating at large-scale coherent structures in the absence of any external forcing. This leads to the formation of swirls, whorls or other complex, local structures in dense suspension of microswimmers and reported in the previous section. Note that theses models are *a priori* valid for dilute or semi-dilute suspensions in contrast to the emergence of local swirls that requires dense suspensions of active particles coupled by hydrodynamic interactions. For rheological properties, the cooperative alignment of swimmers arises from the shear (or external field) but not via hydrodynamic couplings and effects of activity on viscosity are thus predicted even at concentration for which hydrodynamic interaction may be neglected. Nonlinear visco-elasticy properties are also expected [158]. Finally

large fluctuations driven by activity and related to the effective temperature of the active system are also reported [158]

Viscosity measurements

Dense suspensions of active swimmers
Experimental viscosity measurements has recently been tested on active suspensions of microorganisms. Sokolov *et al.* determined the shear viscosity in concentrated suspensions (volume fraction $\Phi \sim 10\%$) of swimming bacteria *Bacillus subtilis* –pushers– in a thin liquid film [162]. They monitored the viscous torque on a rotating particle as well as the decay of a vortex in the film. They measured a decrease of the effective viscosity by up to a factor of 7 compared to the viscosity of the same liquid without bacteria or with nonmotile bacteria. Furthermore, the viscosity depends on the concentration and swimming speed of the bacteria, which underlines the crucial role of the microorganism activity in the mechanism.
Using swimming algae *Chlamydomonas Reinhardtii* in a conventional rheometer, Rafai *et al.* measured that effective viscosity of concentrated (volume fraction $\Phi \sim 20 - 30\%$) suspensions, *i.e.* with live –pullers– algae, was far greater than for the same liquid containing the same concentration of dead algae [99].
These experimental results are in qualitative agreement with above expectations and the basic scenario given on Fig.4.7-a,b): pullers increase the shear viscosity compared to the same passive suspension, while pushers reduce the viscosity. Quantitative comparisons between models and experiments is still to be performed.

Dilute/semi-dilute suspensions of active swimmers
Finally, Chen *et al.* probed non equilibrium properties of a *dilute* active bacterial bath of *E. Coli.* In dilute suspensions, with volume fraction $\Phi \sim 10^{-3}\%$, they measure no departure in the rheological response w.r.t. to the equilibrium situation, but significant enhancement of the fluctuations of the medium thus resulting in a strong violation of the Fluctuation-Dissipation theorem [163]. They also report anomalous $1/\sqrt{(}\omega)$ scaling in the active stress fluctuation spectrum measurements. This arises essentially from the concentration fluctuations in the active stress, but their results underline the importance of the microscopic swimming behavior details in the systems, departures from equilibrium thus proceeding *via* non-universal mechanisms.

4.4 Probing Janus microswimmers suspensions

We have described many signatures of "out-of-equilibriumness" in suspensions of active self-propelled particles in a fluid medium. Theoretical predictions are numerous in the regime of *dense* suspensions: local nematic ordering with the emergence of complex patterns of transient swirls and whorls, namely "zero Reynolds turbulence", distinctive transport properties, notably efficient mixing only for suspensions of pushers ... Moreover, activity impacts rheological properties notably increase/decrease of the shear viscosity even in dilute/semi dilute solutions. Many ex-

perimental validations of some signatures were recently provided with suspensions but only with active biological microorganisms and requires additional insights with large collections of artificial microswimmers. The Janus particles I developed during part of my phD thus proposes a relevant avenue in this context. Synthesizing the theoretical predictions on active suspensions with the specificities of the Janus microswimmers, **the aim of this section is to suggest leads to probe out-of-equilibrium signatures of a suspension of Janus**. Furthermore, a few very preliminary results will be given as hints of collective effects in this section

4.4.1 Bulk rheology measurements

One of the most natural way of probe collective effects in active colloidal suspensions is to perform bulk rheology measurements in the same spirit as experiments by Rafai *et al.* or Sokolov *et al.*. As underlined by [162], the shear viscosity depends on the total active energy injection in the medium, *i.e.* concentration and velocity of the swimmers. Given the typical velocity of biological microorganisms –typically $20-50\mu\mathrm{m}/s$– and the diffusiophoretic velocity of the Janus microswimmers, $V \sim 1-3\mu\mathrm{m}/s$, it will certainly be necessary to compensate the relatively slow velocity with higher concentrations, or certainly not lower. This underlines one of the mean experimental difficulty of bulk rheological measurements with artificial swimmers. It will require to achieve sufficiently highly concentrated suspensions with volume fraction of Janus of order $\Phi \sim 10-50\%$. The synthesis of such collections of artificial swimmers as well as the obten-

tion of so concentrated suspensions is an experimental challenge that we have not addressed up to now. This track is fully to be explored!

4.4.2 Passive tracers dynamics in an active bath of Janus microswimmers

Nonetheless Chen *et al.* demonstrated with passive tracers in a bacterial bath that strong departures from equilibrium can arise from the energy input even in semi-dilute suspensions of active particles $\Phi \sim 10^{-3}$. I developed in chapter 3 experimental techniques to work with Janus suspensions of volume fraction up to $\Phi \sim 10^{-1}$. In this regime I demonstrated that a suspension of active Janus microswimmers can be well described by a fluctuation-dissipation relationship and is *equilibrium-like*. Nevertheless the impact on passive tracers of the activity remains unexplored in our system. Along this line, it appears interesting to study the behavior of *passive tracers* in an active bath of Janus microswimmers (with volume fraction $\Phi \sim 0.01\%$). This can be done by measuring the force response of a passive tracer with optical tweezers which will be interesting to do in the future or studying its dynamics by optical microscopy.
I now present preliminary results for the study of the dynamics of passive tracers in an active bath of Janus microswimmers.

Experiment

We use, as for the the sedimentation experiments (see section 3.4) a hydrogel microfluidic chamber with Janus particles. In order

to locally increase the density and magnify the out-of-equilibrium effets, we use twice heavier Janus particles than in the sedimentation experiments. This is done by increasing the platinum coating to 5 nm –instead of 2 nm– on identical latex particles but non fluorescent. A solution containing these Janus particles ($\Phi_J \sim 10^{-2}\%$ and dilute passive tracers ($\phi_T \sim 10^{-4}\%$, fluorescent latex particles with diameter 1.1μm) is enclosed in the microfluidic chamber as previously described. Furthermore, a solution containing only dilute passive tracers ($\phi_T \sim 10^{-2}\%$, fluorescent latex particles with diameter 1.1μm) is enclosed in a neighboring microfluidic chamber as an equilibrium reference. Hydrogen peroxyde solution at concentration C_0 is continuously circulated in the lateral channels, ensuring a constant renewal of the fuel and removal of chemical waste (see Fig.4.8-a). The long-time dynamics of the Janus swimmers, the tracers in the Janus bath, and the reference tracers are investigated with a CCD camera (μeye) at $0.5Hz$ on time scales up to $60s$ and trajectories are extracted with Matlab analysis. We then calculate the mean square displacement $\Delta L^2(t)$ (see section 3.4.2 for more developments on this point) for each class of particles: swimmers, passive tracers with Janus, passive tracers at equilibrium. Preliminary results for $C_0 = 10\%$ are presented on Fig.4.8-b.

Results and discussions

The mean squared displacement of the passive tracers without Janus is linear with time (see Fig.4.8-b) as expected for equilibrium benchmark. The slope gives the reference diffusion coeffi-

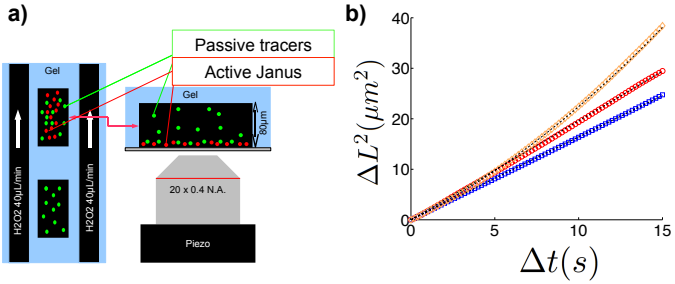

Figure 4.8: **Tracers dynamics in an active bath of Janus microswimmers**. *(a)* Experimental setup. A solution containing Janus particles plus passive tracers is enclosed in a gel microfluidic chamber. Passive tracers are enclosed in an independent chamber as a reference benchmark. Hydrogen peroxyde fuel is injected through lateral channels. The trajectories of *(i)* the passive tracers at equilibrium, *(ii)* the Janus particles and *(iii)* passive tracers in a Janus bath are recorded by a camera and mean squared displacements $\Delta L^2 t(t)$ calculated with Matlab routine. *(b)* $\Delta L^2 t(t)$ obtained for *(i)* passive equilibrium tracers (blue $\square$), *(ii)* Janus microswimmers (red $\circ$) and *(iii)* passive tracers in an active Janus bath (orange $\diamond$). Fitting curves (black dashed lines) for are linear for *(i)* and *(ii)* and parabolic for *(iii)*. Measurements of the equilibrium diffusion constant $D_0 = 0.40 \pm 0.02 \mu\text{m}^2/s$ of the tracers is measured as well as the effective diffusion constant of the Janus microswimmers $D_{eff} = 0.49 \pm 0.02 \mu\text{m}^2/s$. This is in clear contrast with passive tracers in the Janus baths which are advected by a velocity $V_t = 0.6 \pm 0.05 \mu\text{m}/s$. The origin of this flow is to still to be refined but could appear as a hint of cooperative flows generated by Janus activity.

cient of the tracers particles[7]: $D_0 = 0.40 \pm 0.02 \mu\text{m}^2/s$.
The mean squared displacement of the Janus particles appears as linear in time at long times scales with an enhanced diffusion coefficient $D_{eff} = 0.49 \pm 0.02 \mu\text{m}^2/s$.Given the rotational diffusion time $\tau_r \sim 0.9s$ of the janus particles, it is expected to recover a diffusive-like regime. The associated propulsion velocity of the particles is $V \sim 0.7 \mu\text{m}/s$.
The mean squared displacement of the passive tracers with Janus particles is not linear with time and is much better fitted by a parabolic function. This result is in clear discrepancy with the brownian dynamics expected for equilibrium tracers. Fitting the curve with $\Delta L^2(t) = 4D_0 t + \frac{2}{3} V_t^2 t^2$ gives tracers velocity $V_t = 0.6 \pm 0.05 \mu\text{m}/s$.
These experimental results show that passive tracers in an active bath present a completely different dynamics than equilibrium tracers. The convective dynamics observed with Janus particles could be reminiscent of a coherent flow pattern developed by the Janus particles. Further investigations with PIV-measurements of the flow field are of course necessary. As a clear signature of the out-of-equilibrium nature of the system, it will also be interesting to study the fluctuations in these systems and see if departures from equilibrium can be measured. Theses preliminary results need of course to be pushed forward notably with an extensive investigation of experimental parameters (Peclet number of the active particles, concentration of Janus particles in

[7] It accounts eventual modification of viscosity of the medium through the alteration of the gel by the hydrogen peroxide.

the chamber[8]...). Of course, they have to be confirmed but they could demonstrate, as previously reported by [163], that even at low concentration, the adding of active particles may have strong impact on the physical properties of a system. Furthermore they present encouraging hints of collective/cooperative effects in suspensions of active colloids.
Further investigations on collective effects and out-of-equilibrium dynamics of active colloidal suspensions are required and constitute the basis of the PhD work of I. Theurkauff.

[8]In these experiments the concentration is only 2 or 3 times higher than in sedimentation experiments. Work with denser suspensions needs to be done

Bibliography

[1] L. Bocquet and E. Charlaix, "Nanofluidics, from bulk to interfaces," *Chem. Soc. Rev.*, vol. 39, no. 3, pp. 1073–1095, 2010.

[2] G. Taylor, "Dispersion of soluble matter in solvent flowing slowly through a tube," *Proceedings Of The Royal Society Of London Series A-Mathematical And Physical Sciences*, vol. 219, pp. 186–203, 1953.

[3] T. M. Squires and S. Quake, "Microfluidics: Fluid physics at the nanoliter scale," *Reviews of Modern Physics*, vol. 77, pp. 977–1026, 2005.

[4] A. Ajdari, "Pumping liquids using asymmetric electrode arrays," *Physical Review E*, vol. 61, pp. R45–R48, 2000.

[5] A. Stroock, M. Weck, D. Chiu, W. Huck, P. Kenis, R. Ismagilov, and G. Whitesides, "Patterning electro-osmotic flow with patterned surface charge," *Physical Review Letters*, vol. 84, pp. 3314–3317, 2000.

[6] J. P. Urbanski, T. Thorsen, J. A. Levitan, and M. Z. Bazant, "Fast ac electro-osmotic micropumps with nonplanar electrodes," *Applied Physics Letters*, vol. 89, p. 143598, 2006.

[7] V. Studer, A. Pepin, Y. Chen, and A. Ajdari, "An integrated ac electrokinetic pump in a microfluidic loop for fast and tunable flow control," *Analyst*, vol. 129, pp. 944–949, 2004.

[8] M. Bazant and T. Squires, "Induced-charge electrokinetic phenomena: Theory and microfluidic applications," *Physical Review Letters*, vol. 92, p. 066101, 2004.

[9] T. M. Squires, "Induced-charge electrokinetics: fundamental challenges and opportunities," *Lab on a Chip*, vol. 9, p. 2477-2483, 2009.

[10] J. Levitan, S. Devasenathipathy, V. Studer, Y. Ben, T. Thorsen, T. Squires, and M. Bazant, "Experimental observation of induced-charge electro-osmosis around a metal wire in a microchannel," *Colloid Surface A*, vol. 267, p. 122-132, 2005.

[11] J. Van't-Hoff, "The function of osmotic pressure in the analogy between solutions and gases," *Proceedings of the Physical Society of London*, 1887.

[12] L. Rayleigh, "The theory of solution," *Nature*, vol. 55, pp. 253–254, 1897.

[13] J.-L. Barrat and J. P. Hansen, "Basic concepts for simple and complex liquids" *Cambridge University Press*, 2003.

[14] J. Anderson and D. Prieve, "Diffusiophoresis caused by gradients of strongly adsorbing solutes," *Langmuir*, vol. 7, pp. 403–406, 1991.

[15] A. Ajdari and L. Bocquet, "Giant amplification of interfacially driven transport by hydrodynamic slip: Diffusio-osmosis and beyond," *Physical Review Letters*, vol. 96, p. 186102, 2006.

[16] J. Ebel, J. Anderson, and D. Prieve, "Diffusiophoresis of latex-particles in electrolyte gradients," *Langmuir*, vol. 4, pp. 396–406, 1988.

[17] B. Abecassis, C. Cottin-Bizonne, C. Ybert, A. Ajdari, and L. Bocquet, "Boosting migration of large particles by solute contrasts," *Nature Materials*, vol. 7, pp. 785–789, 2008.

[18] J. Anderson and D. Prieve, "Diffusiophoresis - migration of colloidal particles in gradients of solute concentration," *Separation And Purification Methods*, vol. 13, pp. 67–103, 1984.

[19] A. Einstein, "On the theory of the brownian movement," *Annalen der physik*, 1906.

[20] A. Einstein, "On the movement of small particles suspended in stationary liquids required by the molecular-kinetic theory of heat," *Annalen der physik*, 1905.

[21] P. Langevin, "Sur la théorie du mouvement brownien," *Comptes Rendus de l'Académie des Sciences*, vol. 146, pp. 530–533, 1908.

[22] M. von Smoluchowski, "Zur kinetischen theorie der brownschen molekularbewegung und der suspensionen," *Annalen der physik*, 1906.

[23] J. Anderson, "Colloid transport by interfacial forces," *Annual Review of Fluid Mechanics*, vol. 21, 1989.

[24] C. Cottin-Bizonne, B. Cross, A. Steinberger, and E. Charlaix, "Boundary slip on smooth hydrophobic surfaces: Intrinsic effects and possible artifacts," *Physical Review Letters*, vol. 94, p. 056102, 2005.

[25] C. I. Bouzigues, P. Tabeling, and L. Bocquet, "Nanofluidics in the debye layer at hydrophilic and hydrophobic surfaces," *Physical Review Letters*, vol. 101, p. 114503, 2008.

[26] D. M. Huang, C. Sendner, D. Horinek, R. R. Netz, and L. Bocquet, "Water slippage versus contact angle: A quasiuniversal relationship," *Physical Review Letters*, vol. 101, p. 226101, 2008.

[27] D. M. Huang, C. Cottin-Bizonne, C. Ybert, and L. Bocquet, "Massive amplification of surface-induced transport at superhydrophobic surfaces," *Physical Review Letters*, vol. 101, p. 064503, 2008.

[28] C. Ybert, C. Barentin, C. Cottin-Bizonne, P. Joseph, and L. Bocquet, "Achieving large slip with superhydrophobic surfaces: Scaling laws for generic geometries," *Physics of Fluids*, vol. 19, p. 123601, 2007.

[29] T. M. Squires, "Electrokinetic flows over inhomogeneously slipping surfaces," *Physics of Fluids*, vol. 20, p. 092105, 2008.

[30] D. M. Huang, C. Cottin-Bizonne, C. Ybert, and L. Bocquet, "Ion-specific anomalous electrokinetic effects in

hydrophobic nanochannels," *Physical Review Letters*, vol. 98, p. 177801, 2007.

[31] R. Piazza, "Thermophoresis: moving particles with thermal gradients," *Soft Matter*, vol. 4, pp. 1740–1744, 2008.

[32] S. Duhr and D. Braun, "Why molecules move along a temperature gradient," *Proceedings of the National Academy of Sciences of the U.S.A*, vol. 103, pp. 19678–19682, 2006.

[33] A. Wurger, "Thermophoresis in colloidal suspensions driven by marangoni forces," *Physical Review Letters*, vol. 98, p. 138301, 2007.

[34] M. Braibanti, D. Vigolo, and R. Piazza, "Does thermophoretic mobility depend on particle size?," *Physical Review Letters*, vol. 100, p. 108303, 2008.

[35] F. M. Weinert and D. Braun, "An optical conveyor for molecules," *Nano Letters*, vol. 9, pp. 4264–4267, 2009.

[36] H.-R. Jiang, H. Wada, N. Yoshinaga, and M. Sano, "Manipulation of colloids by a nonequilibrium depletion force in a temperature gradient," *Physical Review Letters*, vol. 102, no. 20, p. 208301, 2009.

[37] F. M. Weinert, J. A. Kraus, T. Franosch, and D. Braun, "Microscale fluid flow induced by thermoviscous expansion along a traveling wave," *Physical Review Letters*, vol. 100, p. 164501, 2008.

[38] F. M. Weinert, M. Wuehr, and D. Braun, "Light driven microflow in ice," *Applied Physics Letters*, vol. 94, p. 113901, 2009.

[39] P. Baaske, F. M. Weinert, S. Duhr, K. H. Lemke, M. J. Russell, and D. Braun, "Extreme accumulation of nucleotides in simulated hydrothermal pore systems," *Proceedings of the National Academy of Sciences of the U.S.A*, vol. 104, pp. 9346–9351, 2007.

[40] P. Staffeld and J. Quinn, "Diffusion-induced banding of colloid particles via diffusiophoresis .2. non-electrolytes," *Journal of Colloid And Interface Science*, vol. 130, pp. 88–100, 1989.

[41] P. Staffeld and J. Quinn, "Diffusion-induced banding of colloid particles via diffusiophoresis .1. electrolytes," *Journal of Colloid And Interface Science*, vol. 130, pp. 69–87, 1989.

[42] B. Abecassis, C. Cottin-Bizonne, C. Ybert, A. Ajdari, and L. Bocquet, "Osmotic manipulation of particles for microfluidic applications," *New Journal of Physics*, vol. 11, p. 075022, 2009.

[43] J. Diao, L. Young, S. Kim, E. Fogarty, S. Heilman, P. Zhou, M. Shuler, M. Wu, and M. DeLisa, "A three-channel microfluidic device for generating static linear gradients and its application to the quantitative analysis of bacterial chemotaxis," *Lab on a Chip*, vol. 6, no. 3, pp. 381–388, 2006.

[44] S. Cheng, S. Heilman, M. Wasserman, S. Archer, M. Shuler, and M. Wu, "A hydrogel-based microfluidic device for the studies of directed cell migration," *Lab on a Chip*, vol. 7, no. 6, pp. 763–769, 2007.

[45] M. Chui, R. Phillips, and M. McCarthy, "Measurement of the porous microstructure of hydrogels by nuclear magnetic resonance," *Journal of Colloid And Interface Science*, vol. 174, no. 2, pp. 336–344, 1995.

[46] L. Petit, C. Barentin, J. Colombani, C. Ybert, and L. Bocquet, "Size dependence of tracer diffusion in a laponite colloidal gel," *Langmuir*, vol. 25, pp. 12048–12055, 2009.

[47] CRC, *Handbook of Chemistry and Physics, 89th edition*, 2008

[48] K. Mattern, C. Nakornchai, and W. Deen, "Darcy permeability of agarose-glycosaminoglycan gels analyzed using fiber-mixture and donnan models," *Biophysical Journal*, vol. 95, no. 2, pp. 648–656, 2008.

[49] M. Abramowitz and I. A. Stegun, "Handbook of mathematical functions. with formulas, graphs, and mathematical" , 1968.

[50] H. Risken, "The fokker-planck equation: methods of solution and applications" *Springer, Verlag*, 1996.

[51] R. D. Leonardo, F. Ianni, and G. Ruocco, "Colloidal attraction induced by a temperature gradient," *Langmuir*, vol. 25, 2009.

[52] F. M. Weinert and D. Braun, "Observation of slip flow in thermophoresis," *Physical Review Letters*, vol. 101, p. 168301, 2008.

[53] C. Ybert, F. Nadal, R. Salome, F. Argoul, and L. Bourdieu, "Electrically induced microflows probed by fluorescence correlation spectroscopy," *European Physical Journal E*, vol. 16, pp. 259–266, 2005.

[54] J. Leng, B. Lonetti, P. Tabeling, M. Joanicot, and A. Ajdari, "Microevaporators for kinetic exploration of phase diagrams," *Physical Review Letters*, vol. 96, p. 084503, 2006.

[55] R. Deegan, O. Bakajin, T. Dupont, G. Huber, S. Nagel, and T. Witten, "Capillary flow as the cause of ring stains from dried liquid drops," *Nature*, vol. 389, pp. 827–829, 1997.

[56] H. Berg, "Random walks in biology," *Princeton University Press*, 1993.

[57] H. C. Berg, "Motile behavior of bacteria," *Physics Today*, vol. 53, no. 1, pp. 24–29, 2000.

[58] J. Adler, "Chemotaxis in bacteria," *Science*, vol. 153, pp. 708–16, Aug 1966.

[59] M. Eisenbach and J. W. Lengeler, "Chemotaxis," *Imperial College Press*, 2004.

[60] E. F. Keller and L. A. Segel, "Model for chemotaxis," *Journal of Theoretical Biology*, vol. 30, pp. 225–34, 1971.

[61] E. O. Budrene and H. C. Berg, "Dynamics of formation of symmetrical patterns by chemotactic bacteria," *Nature*, vol. 376, pp. 49–53, 1995.

[62] E. O. Budrene and H. C. Berg, "Complex patterns formed by motile cells of escherichia coli," *Nature*, vol. 349, pp. 630–3, 1991.

[63] S. Park, P. Wolanin, E. Yuzbashyan, H. Lin, N. Darnton, J. Stock, P. Silberzan, and R. Austin, "Influence of topology on bacterial social interaction," *Proceedings of the National Academy of Sciences of the U.S.A*, vol. 100, no. 24, pp. 13910–13915.

[64] Y. Tsori and P. de Gennes, "Self-trapping of a single bacterium in its own chemoattractant," *Europhysics Letters*, vol. 66, pp. 599–602, 2004.

[65] Y. V. Kalinin, L. L. Jiang, Y. H. Tu, and M. M. Wu, "Logarithmic sensing in escherichia coli bacterial chemotaxis," *Biophysical Journal*, vol. 96, pp. 2439–2448, 2009.

[66] Y. L. Qi and J. Adler, "Salt taxis in escherichia-coli bacteria and its lack in mutants," *Proceedings of the National Academy of Sciences of the U.S.A*, vol. 86, pp. 8358–8362, 1989.

[67] H. Y. Chang, "Anatomic demarcation of cells: Genes to patterns," *Science*, vol. 326, pp. 1206–1207, 2009.

[68] T. D. Pollard and J. A. Cooper, "Actin, a central player in cell shape and movement," *Science*, vol. 326, pp. 1208–1212, 2009.

[69] C. E. Holt and S. L. Bullock, "Subcellular mrna localization in animal cells and why it matters," *Science*, vol. 326, pp. 1212–1216, 2009.

[70] L. Shapiro, H. H. McAdams, and R. Losick, "Why and how bacteria localize proteins," *Science*, vol. 326, no. 5957, pp. 1225–1228, 2009.

[71] L. Wolpert, "Positional information revisited," *Development*, vol. 107, pp. 3–12, 1989.

[72] T. Gregor, D. W. Tank, E. F. Wieschaus, and W. Bialek, "Probing the limits to positional information," *Cell*, vol. 130, pp. 153–64, 2007.

[73] A. Eldar, R. Dorfman, D. Weiss, H. Ashe, B.-Z. Shilo, and N. Barkai, "Robustness of the bmp morphogen gradient in drosophila embryonic patterning," *Nature*, vol. 419, pp. 304–8, 2002.

[74] M. Loose, E. Fischer-Friedrich, J. Ries, K. Kruse, and P. Schwille, "Spatial regulators for bacterial cell division self-organize into surface waves in vitro," *Science*, vol. 320, pp. 789–92, 2008.

[75] J. B. Moseley, A. Mayeux, A. Paoletti, and P. Nurse, "A spatial gradient coordinates cell size and mitotic entry in fission yeast," *Nature*, vol. 459, pp. 857–U8, 2009.

[76] L. Rothfield, A. Taghbalout, and Y.-L. Shih, "Spatial control of bacterial division-site placement," *Nature Reviews Microbiology*, vol. 3, no. 12, pp. 959–968, 2005. 10.1038/nrmicro1290.

[77] P. Niethammer, P. Bastiaens, and E. Karsenti, "Stathmin-tubulin interaction gradients in motile and mitotic cells," *Science*, vol. 303, pp. 1862–6, 2004.

[78] A. Turing, "The chemical basis of morphogenesis," *Philosphophical Transactions of the Royal Society of London B*, 1952.

[79] B. N. Kholodenko and W. Kolch, "Giving space to cell signaling," *Cell*, vol. 133, no. 4, pp. 566 – 567, 2008.

[80] R. E. Baker, E. A. Gaffney, and P. K. Maini, "Partial differential equations for self-organization in cellular and developmental biology," *Nonlinearity*, vol. 21, no. 11, pp. R251–R290, 2008.

[81] A. F. Schier and D. Needleman, "Developmental biology: Rise of the source-sink model," *Nature*, vol. 461, pp. 480–1, 2009.

[82] E. Michard, P. Dias, and J. Feijo, "Tobacco pollen tubes as cellular models for ions dynamics: Improved spatial and temporal resolution of extracellular flux and free cytosolic concentration of calcium and protons using phluorin and yc3.1 cameleon," *Sex Plant Reproduction*, vol. 21, 2008.

[83] M. J. Madou, "Fundamentals of microfabrication," *CRC Press*, p. 2640, 2009.

[84] P. Rai-Choudhury, "Handbook of microlithography, micromachining and microfabrication," *Institution of Engineering and Technology*, 1997.

[85] Microchem, "Processing guidelines for su-8 2100 and su-8 2150,"

[86] R. Simha and S. Ramaswamy, "Hydrodynamic fluctuations and instabilities in ordered suspensions of self-propelled particles," *Physical Review Letters*, vol. 89, p. 058101, 2002.

[87] T. Vicsek, A. Czirók, E. Ben-Jacob, I. Cohen, and O. Shochet, "Novel type of phase transition in a system of self-driven particles," *Physical Review Letters*, vol. 75, no. 6, 1995.

[88] I. Llopis and I. Pagonabarraga, "Dynamic regimes of hydrodynamically coupled self-propelling particles," *Europhysics Letters*, 2006.

[89] N. Uchida and R. Golestanian, "Synchronization and collective dynamics in a carpet of microfluidic rotors," *Physical Review Letters*, vol. 104, p. 178103, 2010.

[90] J. Tailleur and M. E. Cates, "Sedimentation, trapping, and rectification of dilute bacteria," *Europhysics Letters*, vol. 86, no. 6, p. 60002 (6pp), 2009.

[91] R. Nash, R. Adhikari, J. Tailleur, and M. Cates, "Run-and-tumble particles with hydrodynamics: Sedimentation, trapping, and upstream swimming," *Physical Review Letters*, vol. 104, p. 258101, 2010.

[92] L. Cisneros, R. Cortez, C. Dombrowski, R. Goldstein, and J. Kessler, "Fluid dynamics of self-propelled microorganisms, from individuals to concentrated populations," *Experiments in Fluids*, vol. 43, no. 5, pp. 737–753, 2007.

[93] K. Leptos, J. Guasto, J. Gollub, A. Pesci, and R. Goldstein, "Dynamics of enhanced tracer diffusion in suspensions of swimming eukaryotic microorganisms," *Physical Review Letters*, vol. 103, p. 198103, Nov 2009.

[94] A. Sokolov, I. S. Aranson, J. O. Kessler, and R. E. Goldstein, "Concentration dependence of the collective dynamics of swimming bacteria," *Physical Review Letters*, vol. 98, p. 158102, 2007.

[95] J. P. Hernandez-Ortiz, C. G. Stoltz, and M. D. Graham, "Transport and collective dynamics in suspensions of confined swimming particles," *Physical Review Letters*, vol. 95, p. 204501, 2005.

[96] I. Tuval, L. Cisneros, C. Dombrowski, C. Wolgemuth, J. Kessler, and R. Goldstein, "Bacterial swimming and oxygen transport near contact lines," *Proceedings of the National Academy of Sciences of the U.S.A*, vol. 102, no. 7, p. 2277, 2005.

[97] X.-L. Wu and A. Libchaber, "Particle diffusion in a quasi-two-dimensional bacterial bath," *Physical Review Letters*, vol. 84, pp. 3017–3020, 2000.

[98] K. Drescher, K. Leptos, I. Tuval, T. Ishikawa, T. Pedley, and R. Goldstein, "Dancing volvox: Hydrodynamic bound states of swimming algae," *Physical Review Letters*, vol. 102, p. 168101, 2009.

[99] S. Rafaï, L. Jibuti, and P. Peyla, "Effective viscosity of microswimmer suspensions," *Physical Review Letters*, vol. 104, p. 098102, 2010.

[100] M. Ballerini, N. Cabibbo, and R. Candelier, "Interaction ruling animal collective behavior depends on topological rather than metric distance: Evidence from a field study," *Proceedings of the National Academy of Sciences of the U.S.A*, 2008.

[101] L. Angelani, R. D. Leonardo, and G. Ruocco, "Self-starting micromotors in a bacterial bath," *Physical Review Letters*, vol. 102, p. 048104, 2009.

[102] R. D. Leonardo, L. Angelani, D. Dell'Arciprete, G. Ruocco, V. Iebba, S. Schippa, M. P. Conte, F. Mecarini, F. D. Angelis, and E. D. Fabrizio, "Bacterial ratchet motors," *Proceedings of the National Academy of Sciences of the U.S.A*, vol. 107, pp. 9541–9545, 2010.

[103] A. Sokolov, M. M. Apodaca, B. A. Grzybowski, and I. S. Aranson, "Swimming bacteria power microscopic gears,"

Proceedings of the National Academy of Sciences of the U.S.A, vol. 107, pp. 969–974, 2010.

[104] A. Cavagna, A. Cimarelli, I. Giardina, G. Parisi, R. Santagati, F. Stefanini, and M. Viale, "Scale-free correlations in starling flocks," *Proceedings of the National Academy of Sciences of the U.S.A*, vol. 107, pp. 11865–11870, 2010.

[105] R. Dreyfus, J. Baudry, M. Roper, M. Fermigier, H. Stone, and J. Bibette, "Microscopic artificial swimmers," *Nature*, vol. 437, pp. 862–865, 2005.

[106] W. Paxton, K. Kistler, C. Olmeda, A. Sen, S. S. Angelo, Y. Cao, T. Mallouk, P. Lammert, and V. Crespi, "Catalytic nanomotors: Autonomous movement of striped nanorods," *Journal of the American Chemical Society*, vol. 126, pp. 13424–13431, 2004.

[107] N. Mano and A. Heller, "Bioelectrochemical propulsion," *Journal of the American Chemical Society*, vol. 127, pp. 11574–11575, 2005.

[108] J. R. Howse, R. A. L. Jones, A. J. Ryan, T. Gough, R. Vafabakhsh, and R. Golestanian, "Self-motile colloidal particles: From directed propulsion to random walk," *Physical Review Letters*, vol. 99, p. 048102, 2007.

[109] P. Tierno, R. Golestanian, I. Pagonabarraga, and F. Sagues, "Controlled swimming in confined fluids of magnetically actuated colloidal rotors," *Physical Review Letters*, vol. 101, p. 218304, 2008.

[110] R. Golestanian, T. B. Liverpool, and A. Ajdari, "Designing phoretic micro- and nano-swimmers," *New Journal of Physics*, vol. 9, p. 126, 2007.

[111] E. Purcell, "Life at low reynolds number," *American Journal of Physics*, 1977.

[112] E. Lauga and T. Powers, "The hydrodynamics of swimming microorganisms," pp. 1–37, 2009.

[113] M. Leoni, J. Kotar, B. Bassetti, P. Cicuta, and M. C. Lagomarsino, "A basic swimmer at low reynolds number," *Soft Matter*, vol. 5, pp. 472–476, 2009.

[114] O. Pak, T. Normand, and E. Lauga, "Pumping by flapping in a viscoelastic fluid," *Physical Review E*, 2010.

[115] E. Lauga, "Life at high deborah number," *Europhysics Letters*, vol. 86, 2009.

[116] E. Lauga, "Propulsion in a viscoelastic fluid," *Physics of Fluids*, vol. 19, 2007.

[117] A. Najafi and R. Golestanian, "Simple swimmer at low reynolds number: Three linked spheres," *Physical Review E*, vol. 69, p. 062901, 2004.

[118] H. Wada and R. R. Netz, "Model for self-propulsive helical filaments: Kink-pair propagation," *Physical Review Letters*, vol. 99, p. 108102, 2007.

[119] H. Wada and R. R. Netz, "Hydrodynamics of helical-shaped bacterial motility," *Physical Review E*, vol. 80, p. 021921, 2009.

[120] M. Polin, I. Tuval, K. Drescher, J. P. Gollub, and R. E. Goldstein, "Chlamydomonas swims with two "gears" in a eukaryotic version of run-and-tumble locomotion," *Science*, vol. 325, pp. 487–490, 2009.

[121] A. Vilfan and F. Julicher, "Hydrodynamic flow patterns and synchronization of beating cilia," *Physical Review Letters*, vol. 96, p. 058102, 2006.

[122] Y. Wang, R. M. Hernandez, D. J. Bartlett, J. M. Bingham, T. R. Kline, A. Sen, and T. E. Mallouk, "Bipolar electrochemical mechanism for the propulsion of catalytic nanomotors in hydrogen peroxide solutions," *Langmuir*, vol. 22, pp. 10451–10456, 2006.

[123] A. Perro, S. Reculusa, S. Ravaine, E. B. Bourgeat-Lami, and E. Duguet, "Design and synthesis of janus micro- and nanoparticles," *Journal of Materials Chemistry*, vol. 15, no. 35-36, pp. 3745–3760, 2005.

[124] S. Jiang, Q. Chen, M. Tripathy, E. Luijten, K. S. Schweizer, and S. Granick, "us particle synthesis and assembly," *Advanced Materials*, vol. 22, pp. 1060–1071, 2010.

[125] S. Gangwal, O. J. Cayre, M. Z. Bazant, and O. D. Velev, "Induced-charge electrophoresis of metallodielectric particles," *Physical Review Letters*, vol. 100, p. 058302, 2008.

[126] L. Hong, A. Cacciuto, E. Luijten, and S. Granick, "Clusters of charged janus spheres," *Nano Letters*, vol. 6, pp. 2510–2514, 2006.

[127] S. Sacanna, W. T. M. Irvine, P. M. Chaikin, and D. J. Pine, "Lock and key colloids," *Nature*, vol. 464, pp. 575–578, 2010.

[128] R. Golestanian, T. B. Liverpool, and A. Ajdari, "Propulsion of a molecular machine by asymmetric distribution of reaction products," *Physical Review Letters*, 2005.

[129] W. F. Paxton, S. Sundararajan, T. E. Mallouk, A. Sen, "Chemical locomotion," *Angewandte Chemie-International Edition*, vol. 45, 2006.

[130] D. Sage, F. Neumann, F. Hediger, S. Gasser, and M. Unser, "Automatic tracking of individual fluorescence particles: Application to the study of chromosome dynamics," *Ieee Transactions On Image Processing*, vol. 14, pp. 1372–1383, 2005.

[131] A. Baskaran and M. Marchetti, "Enhanced diffusion and ordering of self-propelled rods," *Physical Review Letters*, vol. 101, p. 268101, 2008.

[132] R. Golestanian, "Anomalous diffusion of symmetric and asymmetric active colloids," *Physical Review Letters*, vol. 102, no. 18, p. 188305, 2009.

[133] J. Perrin, "Mouvement brownien et réalité moléculaire," *Annales de Chimie et de Physique*, 1909.

[134] H. Callen, "Thermodynamics and an introduction to thermostatistics (2nd edition)," *Wiley*, 1985.

[135] M. Born, E. Wolf, and A. Bhatia, "Principles of optics: Electromagnetic theory of propagation, interference and diffraction of light," *Cambridge University Press*, 1999.

[136] D. Loi, S. Mossa, and L. Cugliandolo, "Effective temperature of active matter," *Physical Review E*, vol. 77, p. 051111, 2008.

[137] A. Baskaran and M. C. Marchetti, "Statistical mechanics and hydrodynamics of bacterial suspensions," *Proceedings of the National Academy of Sciences of the U.S.A*, vol. 106, pp. 15567–15572, 2009.

[138] V. Narayan, S. Ramaswamy, and N. Menon, "Long-lived giant number fluctuations in a swarming granular nematic," *Science*, vol. 317, no. 5834, pp. 105–108, 2007.

[139] J. Deseigne, O. Dauchot, and H. Chate, "Collective motion of vibrated polar disks," *Physical Review Letters*, vol. 105, p. 098001, 2010.

[140] P. D. Gennes, "Scaling concepts in polymer physics" *Cornell University Press*, 1979.

[141] T. Uchiyama, Y. Kiritoshi, J. Watanabe, and K. Ishihara, "Degradation of phospholipid polymer hydrogel by hydrogen peroxide aiming at insulin release device," *Biomaterials*, vol. 24, pp. 5183–5190, 2003.

[142] T. Dahl, G. He, and G. Samuels, "Effect of hydrogen peroxide on the viscosity of a hydroxyethylcellulose-based gel," *Pharmaceutical Research*, vol. 15, pp. 1137–1140, 1998.

[143] G. Gregoire and H. Chate, "Onset of collective and cohesive motion," *Physical Review Letters*, vol. 92, p. 025702, 2004.

[144] J. Toner and Y. Tu, "Long-range order in a 2-dimensional dynamical xy model - how birds fly together," *Physical Review Letters*, vol. 75, pp. 4326–4329, 1995.

[145] Y. Tu, J. Toner, and M. Ulm, "Sound waves and the absence of galilean invariance in flocks," *Physical Review Letters*, vol. 80, pp. 4819–4822, 1998.

[146] J. Toner, Y. Tu, and S. Ramaswamy, "Hydrodynamics and phases of flocks," *Annals of Physics*, vol. 318, 2005.

[147] H. Chate, F. Ginelli, G. Gregoire, F. Peruani, and F. Raynaud, "Modeling collective motion: variations on the vicsek model," *European Physical Journal B*, vol. 64, pp. 451–456, 2008.

[148] D. Volfson, A. Kudrolli, and L. Tsimring, "Anisotropy-driven dynamics in vibrated granular rods," *Physical Review E*, vol. 70, p. 051312, 2004.

[149] A. Kudrolli, G. Lumay, D. Volfson, and L. S. Tsimring, "Swarming and swirling in self-propelled polar granular rods," *Physical Review Letters*, vol. 100, p. 058001, 2008.

[150] F. Ginelli, F. Peruani, M. Baer, and H. Chate, "Large-scale collective properties of self-propelled rods," *Physical Review Letters*, vol. 104, p. 184502, 2010.

[151] F. Peruani, A. Deutsch, and M. Bar, "Nonequilibrium clustering of self-propelled rods," *Physical Review E*, vol. 74, p. 030904, 2006.

[152] S. Ramaswamy, "The mechanics and statistics of active matter," *arxiv*, vol. cond-mat.soft, 2010.

[153] V. Narayan, S. Ramaswamy, and N. Menon, "Long-lived giant number fluctuations in a swarming granular nematic," *Science*, vol. 317, pp. 105–108, 2007.

[154] H. Chate, F. Ginelli, and R. Montagne, "Simple model for active nematics: Quasi-long-range order and giant fluctuations," *Physical Review Letters*, vol. 96, p. 180602, 2006.

[155] D. Saintillan and M. J. Shelley, "Instabilities, pattern formation, and mixing in active suspensions," *Physics of Fluids*, vol. 20, p. 123304, 2008.

[156] D. Saintillan and M. J. Shelley, "Orientational order and instabilities in suspensions of self-locomoting rods," *Physical Review Letters*, vol. 99, p. 058102, 2007.

[157] C. Dombrowski, L. Cisneros, S. Chatkaew, R. Goldstein, and J. Kessler, "Self-concentration and large-scale coherence in bacterial dynamics," *Physical Review Letters*, vol. 93, p. 098103, 2004.

[158] Y. Hatwalne, S. Ramaswamy, M. Rao, and R. Simha, "Rheology of active-particle suspensions," *Physical Review Letters*, vol. 92, p. 118101, 2004.

[159] D. Saintillan, "Extensional rheology of active suspensions," *Physical Review E*, vol. 81, p. 056307, 2010.

[160] B. M. Haines, I. S. Aranson, L. Berlyand, and D. A. Karpeev, "Effective viscosity of dilute bacterial suspensions: a two-dimensional model," *Physical Biology*, vol. 5, p. 046003, 2008.

[161] T. Ishikawa and T. J. Pedley, "The rheology of a semi-dilute suspension of swimming model micro-organisms," *Journal of Fluid Mechanics*, vol. 588, pp. 399–435, 2007.

[162] A. Sokolov and I. S. Aranson, "Reduction of viscosity in suspension of swimming bacteria," *Physical Review Letters*, vol. 103, p. 148101, 2009.

[163] D. T. N. Chen, A. W. C. Lau, L. A. Hough, M. F. Islam, M. Goulian, T. C. Lubensky, and A. G. Yodh, "Fluctuations and rheology in active bacterial suspensions," *Physical Review Letters*, vol. 99, p. 148302, 2007.